TÉCNICO LISBOA

The study of the impact of angular momentum transport in low mass red giant stars using asteroseismology

Beatriz José Campos Bordadágua

Thesis to obtain the Master of Science Degree in

Engineering Physics

Supervisor: Prof. Dr. Ilídio Pereira Lopes

Examination Committee

Chairperson: Prof. Dr. José Pizarro de Sande e Lemos
Supervisor: Prof. Dr. Ilídio Pereira Lopes
Member of the Committee: Prof. Dr. Ana Olímpia Gonçalves Madeira de Brito

September 2022

To my mother.

Acknowledgments

Throughout all these years I came across several people that have had a meaningful impact on my path and have contributed significantly to my professional and personal growth. To each and every one of you – Thank you.

Distinctively, I would like to acknowledge and express my gratitude to my supervisor, Prof. Ilídio Lopes, for his insight, guidance, constant availability and his sharing of knowledge that has made this thesis possible. I also want to thank the members of CENTRA who helped me along the way. In particular, I want to thank Ana Brito, for the insightful criticism that certainly improved this work. I also want to acknowledge the creators of MESA and GYRE for making the codes and extensive support material publicly available, which was the foundation of my work.

I appreciate all the opportunities that I had in these years. In particular, I want to highlight my colleagues who deposited their trust on me and granted me the opportunity to participate and manage NFIST for two years. It was truly an incredible experience that I will always treasure.

I would like to thank my family for their understanding and support throughout all these years. To my closest friends that followed along this long journey, through the best and the not-so-good moments – I thank you for your friendship and companionship that persevered.

Last but certainly not least, I want to, wholeheartedly, express my gratitude to my Mother, for all the unconditional love and support, for believing in me despite all the adversities, and for the extraordinary selfless efforts to get me where I am today. Finally, to Eduardo, I am forevermore grateful for the patience, words of encouragement, crucial support and for just being a true font of inspiration.

Resumo

Modelos computacionais e analíticos prevêem vários mecanismos de transporte de momento angular(AM) e de mistura de elementos-químicos capazes de descrever a física dos interiores estelares. No entanto, medições recentes da rotação do núcleo de gigantes vermelhas(RGB) disponibilizas pela missão Kepler, apontam um possível mecanismo de transferência AM em falta na actual teoria.

Na primeira parte, utilizamos o código de evolução estelar MESA para calcular modelos de uma estrela de baixa-massa com rotação(KIC8579095) desde idade-zero-da-sequência-principal(ZAMS) até ao RGB. Incluimos o transporte de AM e a mistura-química devido a campos magnéticos em zonas radiativas, usando o Tayler-Spruit dínamo e a recente revisão,Fuller-Formalism, que mostrou resultados promissores. Fazemos também uso do código de pulsações,GYRE, para continuar a estudar estes mecanismos usando asteroseismologia. Verificamos que apenas os modelos que incluem o Fuller-formalism para o transporte AM foram capazes de prever as taxas de rotação do núcleo observadas na RGB.A eficiência do transporte de AM aumenta com a inclusão da mistura-química, apesar da mistura induzida pelo Fuller-formalism ser extremamente pequena, como esperado.

Na segunda parte, testámos a eficiência do transporte AM com o Fuller-formalism para diferentes parâmetros iniciais.Encontrámos modelos particularmente sensíveis a variações no parâmetro-α e na massa inicial, mas menos à metalicidade e ao overshooting. Por último, utilizando uma amostra de 1093 estrelas sequência-principal(MS) até ao aglomerado-vermelho(RC) entre 1-2$M_{\odot}$, modelámos uma estrela com 1.5$M_{\odot}$ usando Fuller-formalism e comparámos os resultados obtidos com observações asterosísmicas. Verificámos que é necessária uma gama mais ampla para o parâmetro-α[0,5;5] reproduzir as medições na RGB e RC.

Palavras-chave: Asterosismologia; estrelas; gigante vermelha; rotação; momento angular

Abstract

Computational and analytical models predict several mechanisms of transport of angular momentum(AM) and of chemical-mixing capable of describing the physics in star's interiors. Nonetheless, recent measurements of core rotation rates of red-giants(RGB) stars enabled by the Kepler mission, indicate a possible missing AM transfer mechanism in the current theory of stellar interiors.

In the first part, we use the Modules for Experiments in Stellar Astrophysics(MESA) code to compute models of a low-mass rotating star(KIC8579095) from the zero-age-main-sequence(ZAMS) to the RGB. We include transport of AM and chemical-mixing due to magnetic fields in radiative zones, using the Tayler-Spruit dynamo and the recent revision,Fuller-formalism, which has showed very promising results for RGB models. We use the pulsation code,GYRE, to further study this mechanisms using asteroseismic observables.We find that only the models including the Fuller-formalism were able to predict the RGB observed core rotation rates. The efficiency of transport of AM increases with inclusion of mixing, despite the Fuller-formalism mixing being extremely small as expected.

In the second part, we tested the efficiency of AM transport of Fuller-formalism models with different input physics. We found models particularly sensible to variations in the free α-parameter and initial-mass, but less to metallicity and overshooting.Lastly, using a sample of 1093 stars from main-sequence(MS) to red-clump(RC) with 1-2$M_{\odot}$, we modeled a typical star with a mass of 1.5$M_{\odot}$ using the Fuller-formalism and compared the results with asteroseismic observations. We found that a wider range for α-parameter[0.5;5] is needed to reproduce the measurements of RGB and RC stars.

Keywords: Asteroseismology; stars; red giant; rotation; angular momentum

Contents

List of Figures

List of Tables

Nomenclature

Constants

G	Gravitational constant
c	Speed of light in vacuum
c_s	Speed of sound

Physical Quantities

R	Stellar radius
M	Stellar mass
L	Stellar luminosity
T	Temperature
Ω	Angular velocity
r	Radius
m	Mass
Ψ	Total potential
Φ	Newtonian potential
ρ	Density
p	Pressure
g	Gravitational acceleration
t	Time
κ	Opacity
V	Volume
v	Velocity
Z	Metallicity
Y	Helium abundance
X	Hydrogen abundance
$[Fe/H]$	Metallicity (Iron-to-Hydrogen ratio)
f_{P}, f_{T}	Form factors
q	Heat
ξ	Displacement
θ	Colatitude
ϕ	Longitude
ν_{nl}	Frequency
ω	Angular frequency
S_l	Lamb frequency
N	Brunt-Väisälä frequency
$\Delta\nu$	Large frequency separation
$\Delta\Pi$	Period separation
i	Specific moment of inertia
ν	Viscosity coefficient
X	Mass fraction
D	Mixing diffusion coefficient
B	Magnetic field
q	Dimensionless shear
l	Length scale
η	Magnetic difusivity

Subscripts

$\odot$	Solar quantity		
dyn	Dynamical quantity	m	Azimuthal order
KH	Kelvin-Helmholtz quantity	$\mathrm{r, h}$	Radial and horizontal components
nuc	Nuclear quantity	max	Maximum quantity
crit	Critical velocity quantity	min	Minimum quantity
eff	Effective quantity	norm	Normalized quantity
rad	Effective quantity	TS	Tayler-Spruit quantity
ν	Neutrino quantity	F	Fuller quantity
grav	Gravitational quantity	A	Alfvèn quantity
ad	Adiabatic quantity	rad	Radiation quantity
0	Equilibrium quantity	ov	Overshooting quantity
Lag	Lagrangian quantity	star	Stellar quantity
Eul	Eulerian quantity	seis	Seismic quantity
n	Radial order	mod	Model quantity
l	Spherical degree	core	Core quantity
surf	Surface quantity	env	Envelope quantity

Acronyms

AM	Angular momentum
HR	Hertzsprung-Russel
ISM	Interstellar medium
pre-MS	Pre main-sequence
ZAMS	Zero age main-sequence
MS	Main-sequence
SGB	Subgiant branch
RGB	Red giant branch
AGB	Asymptotic giant branch
post-AGB	post asymptotic giant branch
WD	White dwarf
CNO	Carbon-Nitrogen-Oxygen
KIC	*Kepler* input catalog
MOST	Microvariablity and Oscillations of STars
CoRoT	Convection, Rotation and exoplanetary Transits
TESS	Transiting Exoplanet Survey Satellite
PLATO	PLAnetary Transits and Oscillations
MESA	Modules for Experiments in Stellar Astrophysics
MLT	Mixing-length theory
p-mode	Pressure mode
g-mode	Gravity mode
PDS	Power density spectrum
IGWs	Internal gravity waves
APOGEE	Apache Point Observatory Galactic Evolution Experiment
DR	Data release

Chapter 1

Introduction

Stars are the building blocks of the Universe. Our current knowledge of stars, planetary systems, galaxies and the Universe is only possible due to light received from them. The production of nearly all chemical elements in the Universe occurs in stellar interiors, hence stars are responsible for the dynamical and chemical evolution of galaxies, planetary systems and of any potential form of life.

For most subjects in astrophysics, computational models of stellar structure and evolution are needed, and are required to have remarkable precision to test theoretical predictions against the ever more precise observations. In 1926, Arthur Eddington wrote in his paper *The Internal Constitution of the Stars:* "At first sight it would seem that the deep interior of the Sun and stars is less accessible to scientific investigation than any other region of the Universe. [...] Our telescopes may probe farther and farther into the depths of space; but how can we ever obtain certain knowledge of that which is hidden beneath substantial barriers? [...] What appliance can pierce through the outer layers of a star and test the conditions within?" – Eddington (1926). The answer to this question would later be unveiled through the field of Asteroseismology.

1.1 Motivation

More than 400 years ago, in 1596, David Fabricius discovered the first known periodic variable star, named Mira, that disappeared and reappeared from the sky every $\sim$ 11 months. Nowadays, we know pulsating stars populate a large portion of the Hertzsprung-Russel (HR) diagram. Several types of pulsators have been identified in terms of the type of excited pulsation mode, mass and evolutionary state (temperature and luminosity) as can be seen in figure 1.1.

Due to its proximity to the Earth, the interior structure of the Sun is the most studied so far. The field of helioseismology has brought unprecedented resolution to the solar surface, with the observations of millions of pulsation modes (e.g., Christensen-Dalsgaard 2002).The frequencies of oscillation modes observed in the surface of individual stars are dependent on physical properties of the stellar interiors. Stellar nucleosynthesis and other physical processes (e.g., mixing and diffusion) that have crucial impact in the structure and course of evolution of stars predominately take place in deep stellar interiors. Hence, observations of

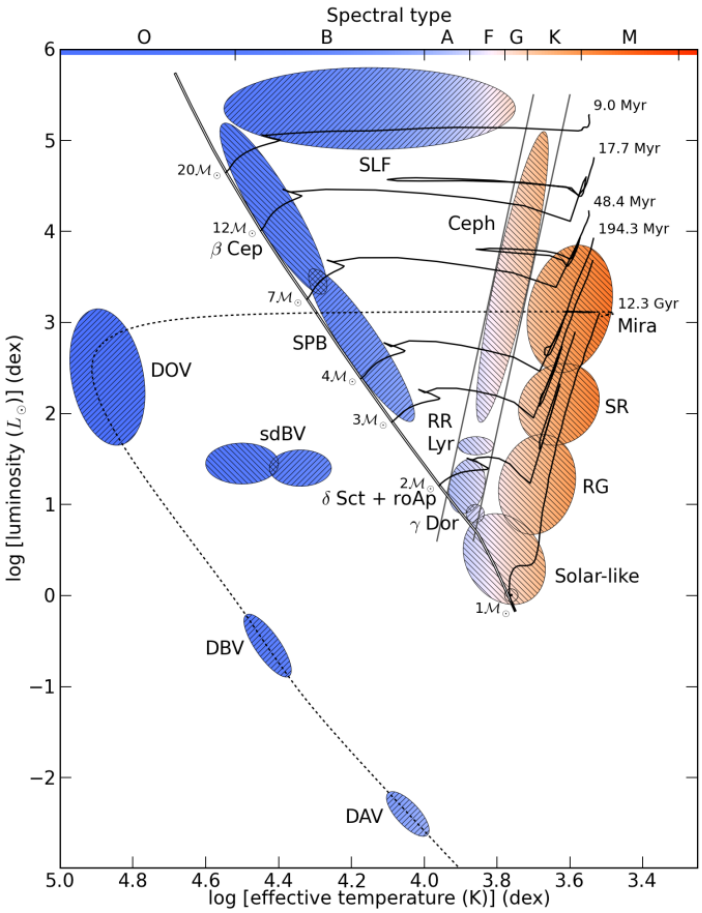

Figure 1.1: HR diagram of different classes of pulsating stars following the nomenclature used by Aerts et al. (2010). The solid black lines and the black dotted line correspond to standard evolutionary tracks, with initial masses and timescales as indicated. The gray lines represent the classical instability strip borders. The hatching linestyle used marks the dominant type of oscillation mode in each class: // for gravity modes and \\ for pressure modes. Figure produced by Péter Pápics, adapted from Aerts (2021).

the time-dependent light output from variable stars on timescales shorter than evolutionary changes show that they can be used to learn about these important physical processes, something unachievable to other methods. Asteroseismology thus uses theoretical models to predict eigenfrequencies based on the current knowledge of stellar structure, and matches the obtained values to the observations.

The pulsation modes identified in stellar surfaces are originated by waves propagating in stellar interiors, analogously to sound waves resonating in musical instruments. The simplest normal modes that stars can pulsate in are radial modes, where the star expands and contracts in a periodic motion. In nonradial modes some parts of the star move up while others are going down periodically, changing the stars' shape and breaking spherical symmetry. The two major restoring forces for stellar oscillations are the pressure and buoyancy. For radial motion (known as p-modes) the pressure acts as the main restoring force, whereas for predominately horizontal motion (known as g-modes), gravity acts through buoyancy, similar to how horizontally propagating waves are generated when throwing a stone into a pond (Handler 2013).

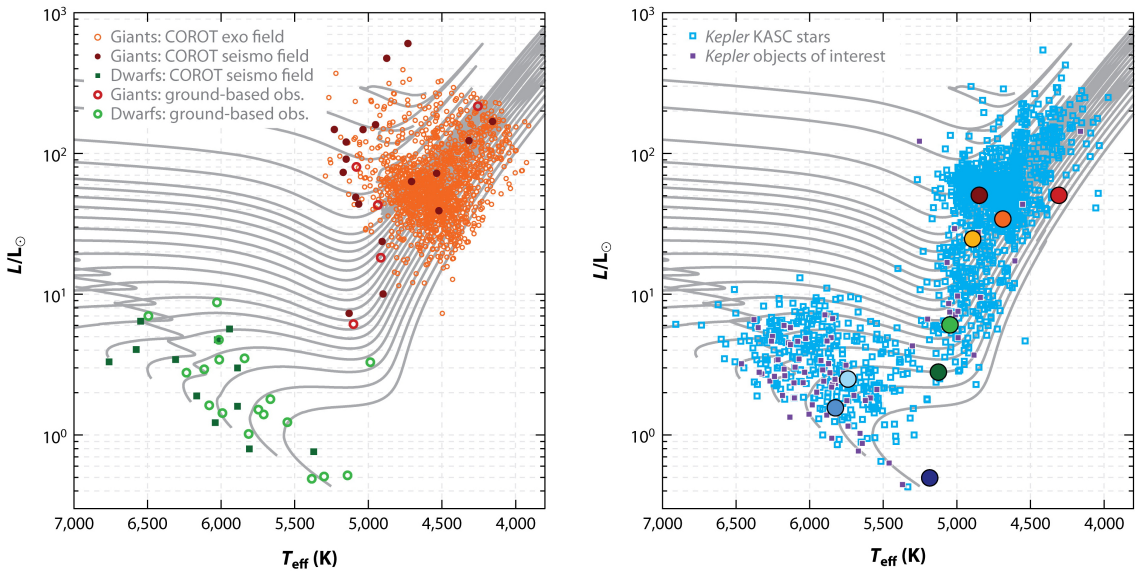

Figure 1.2: HR diagrams showing populations of stars with detected solar-like oscillations by CoRoT and ground-based telescopes (left) and by *Kepler* (right). The large dark blue circles correspond to MS stars. The light blue and dark green circles are stars located in the SGB. The light green, yellow, orange and red circles are stars in the RGB. Adapted from Chaplin and Miglio 2013.

After Ledoux (1951) analysis, ground-based observatories intensively searched for nonradial oscillations in pulsating stars during half century. The search for solar-like oscillations further intensified after the predictions published by Kjeldsen and Bedding (1995), that led to the first definite discovery of solar-like oscillations in a star other than the Sun (Kjeldsen et al. 1995).

In the past decade, space missions dedicated to asteroseismology revolutionized the understanding of pulsating stars. With the assembly of long-duration photometric data came an unprecedented quality regarding the total length of the timeseries, the signal to noise ratio, and the number and range of observed stars. Oscillation frequencies can now be measured directly from data with a precision of 0.001% for p-modes of low-mass stars and 0.1% for g-modes of intermediate mass stars (Aerts et al. 2019).

The first space mission dedicated to asteroseismology and launched in 2003 was Canada's MOST mission (Microvariablity and Oscillations of STars; Walker et al. 2003). In 2006, the French-led CoRoT mission (Convection, Rotation, and exoplanetary Transits; Baglin et al. 2007) was launched into a low-Earth orbit to monitor numerous nonradial pulsators and search for exoplanets. A major success of this mission was the first discovery of nonradial oscillations in hundreds of red giant stars (Hekker et al. 2009) which opened up the field of red giant seismology. Nonradial oscillations are capable of probing the deepest interiors of stars, and after this mission, have now been identified in almost all stellar mass ranges (see figure 1.2), finally bringing observational constraints to the study of stellar interiors (see e.g., Aerts 2021).

The NASA *Kepler* mission was launched in 2009 (Koch et al. 2010, Borucki et al. 2010) with almost 100 times better precision for the oscillation frequencies than CoRoT, and with a low noise level enabling the detection of $l = 3$ modes. Thanks to the *Kepler* mission there is an overwhelming amount of precision data

(around 14 000 red giants; see figure 1.2) which will bring more validation to the theory of stellar oscillations and to stellar structure models.The *Kepler* space telescope has also made huge contributions to the field of exoplanets, providing over 5 100 exoplanet candidates.

Currently, the ongoing NASA TESS space mission (Transiting Exoplanet Survey Satellite; Ricker et al. 2014) is scanning almost the entire sky and delivering high-precision space photometry for millions of stars, a larger sample than *Kepler*, but at the cost of less precision in asteroseismic oscillation frequencies. The ESA PLATO mission (PLAnetary Transits and Oscillations of stars; Rauer et al. 2014), expected to be launched in 2026, will survey an even larger amount of stars (bringing up to a million the number of main-sequence, subgiant and red giant stars data) with higher precision than previously provided by CoRoT and *Kepler*.

The observation of solar-like oscillations in red giant stars from CoRoT and *Kepler* has led to numerous breakthroughs, since important internal physics; such as convective overshooting, angular momentum transport and rotational mixing – are more pronounced in evolved stars as they accumulate with time. The red giant phase happens after the core hydrogen depletion, and hydrogen-burning starts in the shell surrounding the core. These stars are brighter and have longer oscillation timescales from a few hours to months (Huber et al. 2011; Mosser et al. 2012). *Kepler*'s detection of g-mode period spacings in a red giant (Beck et al. 2011), and the discovery of gravity-dominated mixed modes in red giants (Bedding et al. 2011) revealed the ability to probe both the inner and outer regions of stellar interiors in this stars, depending on their predominant g- or p-mode nature. Those observations also provided a clear separation between hydrogen shell burning and helium core burning stars. Kepler's measurements of rotational splittings of dipole mixed modes led to the determination of internal rotation profiles in evolved stars. Slower core rotation in red giant stars was found contrary to model predictions (Beck et al. 2012), highlighting some inaccuracies in the current description of internal angular momentum transport (Mosser et al. 2012).

Rotation should be viewed as a phenomenon that dominates the course of stellar evolution at particular stages, and not always as a side effect of stellar evolution, as there is a vast amount of evidence of rotational effects from spectroscopy, interferometric observations, chemical abundance determinations, and recently asteroseismology (e.g., Maeder 2009). In fact, space asteroseismology has the possibility to uncover the hidden physics behind the internal transport of angular momentum and chemical mixing processes in radiative zones of stars. At the moment, there are two major promising theories. Either angular momentum transport by internal gravity waves (IGWs; e.g., Rogers et al. 2013) or by instabilities due to magnetic fields as proposed by Spruit (2002) and reformulated by Fuller et al. (2019). Both theories are still incomplete and there is currently no scientific consensus.

1.2 Objectives

It is known from literature that internal diffusive transfer processes, angular momentum transport and mixing of chemical elements, influence the course of stellar evolution and structure (e.g., Maeder 2009). The search for the missing mechanism that could explain the differences between theory and asteroseismic

measurements is still a topic of debate, hence the focus of many studies is usually around finding the most efficient mechanisms. Our first goal consists on understanding the impact of different prescriptions of angular momentum transport, such as hydrodynamic instabilities (Heger et al. 2000) and magnetic torques by Spruit 2002 (Tayler-Spruit dynamo) and by Fuller et al. 2019 (recently referred as Fuller-formalism), in the stellar evolution and structure of low mass red giant stars.

The rotation-induced chemical mixing in stellar interiors is also an open topic since observations have revealed discrepancies in computational models. We incorporate, for the first time, chemical mixing due to the Fuller-formalism, using the coefficient derived by Fuller et al. (2019) with the goal to compare its efficiency with the Tayler-Spruit dynamo and with hydrodynamic instabilities, and to understand its impact in the chemical abundance profile of the models. Asteroseismic variables are a great tool to infer the properties of stellar interiors, hence we aim to compute the mode oscillations frequencies of our previous calculated models to better comprehend the effects of this transfer processes and attest if those effects are visible enough to be detected in asteroseismic observations.

The Fuller-formalism is one of the current best candidates to explain the transport of angular momentum in radiative interiors. However, the free parameter in this theory has received some attention (Eggenberger et al. 2019; den Hartogh et al. 2020) since it shows some incompatibilities at some evolutionary stages. Using up-to-date asteroseismic inferred rotational splittings, we want to extend the knowledge on this formalism by testing its sensibility to different input parameters. It is also our objective to constraint the free parameter of this formalism, by establishing an upper and lower limit to reproduce the large range of core rotation rates of the stars, from the main-sequence to the red clump, in our sample.

1.3 Thesis Outline

In this chapter (Chapter 1) we introduce our topic of study and the context of this subject in the current astrophysics research. We also summarize the objectives for this thesis and list its structure, as follows.

Chapter 2 introduces the theoretical background for the work presented in this thesis. In Section 2.1, we start by describing the stellar evolution, from the process of star formation until the cooling white-dwarf phase. Next, we lay out the basic equations used to model the structure evolution of rotating stars. In Sections 2.2 and 2.3, we take a close look at the theory for stellar oscillations and at the used approximations to arrive at the asymptotic expressions that describe with a good level of accuracy the mode behavior found in observed stellar oscillation spectra.

Chapter 3 summarizes the state-of-the-art on rotation in stellar interiors. Section 3.1 briefly describes the impact of rotation on the stellar surface and interior. In Section 3.2 we describe the most important mechanisms of transport of angular momentum and rotationally-induced chemical mixing, along with their capacity to probe current observations, and their implementation in current stellar evolution codes. Section 3.3 is dedicated to explain the Tayler-Spruit dynamo and Fuller-formalism.

In Chapter 4 we display the observational spectroscopic and asteroseismic data used to constraint our

numerical models and we describe the methodology used in this work. In Chapter 5 we first discuss the impact of different implementations of angular momentum transport on a red giant model (Section 5.1). We also include models with different mechanisms of rotation-induced chemical mixing in Section 5.2. In Section 5.3 we tested the effects of the Tayler-Spruit dynamo and Fuller-formalism in the asteroseismic parameters, dipole mode period spacing and rotational splitting, and on the eigenfunctions.

In Chapter 6 we started by gathering a significant amount of measured rotational splittings for stars in the range 1-2 $M_{\odot}$ from the main-sequence to the red clump stage (Section 6.1). In Section 6.2 we test the variability of the models for several input parameters using the Fuller-formalism prescription for transport of angular momentum. At last, we find new constraints for the initial rotation period and free parameter of this mechanism (Section 6.3).

In the last chapter (Chapter 7), we outline our results, present our conclusions and make suggestions for future work in this subject.

Chapter 2

Theoretical background

This chapter presents the theoretical background for the work performed in this thesis. The chapter starts with a brief description of the stellar evolution process, from the beginning of star formation until the white dwarf phase of stars with masses around 1.5 $M_{\odot}$, including rotation effects in the stellar structure equations. Next, we focus on the theoretical foundation for the study of stellar oscillations, discuss the asymptotic theory and finish with a summary of the observational and theoretically derived impact of rotation on oscillation frequencies.

2.1 Stellar evolution

The generally accepted theory of star formation states stars are formed inside large dense interstellar molecular clouds, that have between 10^5-10^6 solar masses and diameters of about 50 pc with temperatures typically around 15 K (e.g., Carroll and Ostlie 2007). As a part of the interstellar medium (ISM), these clouds are rich in hydrogen (H), helium (He) and contain more or less heavier elements depending on the population type of its surroundings. The interstellar medium components constitute the remains from which new stars are born and severely determine the course of stellar evolution. During a star's lifetime, part of its constituent matter is returned to the interstellar medium (e.g., through stellar winds, supernovae) from which future star generations will form, restarting a new star formation cycle.

Star formation is triggered when these massive clouds of gas become gravitationally unstable and induce collapse, fragmenting into smaller parts. Rotation enhances this fragmentation process. The angular momentum embedded in the original cloud is conserved as time evolves, thus the fragments rotate faster as they further contract, until a break-up velocity is reached. To form future rotating stars, preventing further contraction or fragmentation, angular momentum has to reduce by a factor of 10^5-10^6 (Maeder 2009). This is sustained by an evacuation of angular momentum, progressively forming an accretion disc, that will constitute future planetary systems.

The contraction takes place on a dynamical timescale, as the gas is free falling towards the center of the cloud. The gravitational potential energy is successively transformed into thermal energy and radiation, increasing the density and pressure in the center, consequently increasing the opacity of the cloud. With

increasing thermal energy generation, the temperature begins to rise, entering the stage where the cloud is considered a protostar (e.g., Kippenhahn et al. 2013), mainly composed of molecular hydrogen (pre main-sequence phase, pre-MS, in figure 2.1).

With further contraction, eventually, the temperature in the core reaches a point where ignition of hydrogen fusion is possible (if the mass exceeds 0.08 $M_\odot$; Carroll and Ostlie 2007), and a star is 'born'. The process of stellar evolution begins in the so-called zero age main-sequence (ZAMS) phase. At this stage, the contraction stops and the star enters the main-sequence (MS) evolution (figure 2.1), where there is a balance between the nuclear energy generation and the energy radiated through the surface. The star settles into hydrostatic equilibrium, and its structure changes with time mainly due to alterations in the chemical composition from the nuclear reactions.

Throughout the different evolutionary phases, changes in the star take place on different timescales. In the main-sequence, evolution is mainly governed by three basic timescales (e.g., Christensen-Dalsgaard 2021). The previously mentioned dynamical timescale corresponds to the star's reaction in response to loss of hydrostatic equilibrium, the time it would take a star to collapse if the pressure counterbalancing gravity were removed, and may be estimated as

$$\tau_{\rm dyn} = \left(\frac{R^3}{GM}\right)^{1/2} \simeq 30 \text{ min} \left(\frac{R}{R_\odot}\right)^{3/2} \left(\frac{M}{M_\odot}\right)^{-1/2}, \tag{2.1}$$

where G is the universal gravitational constant, M and R are the stellar mass and radius, respectively. The thermal or Kelvin-Helmholtz timescale is associated with the time in which a star would radiate away all its thermal energy if the nuclear reactions in its core ceased, so thus,

$$\tau_{\rm KH} = \frac{GM^2}{RL} \simeq 3 \times 10^7 \text{ year} \left(\frac{M}{M_\odot}\right)^2 \left(\frac{R}{R_\odot}\right)^{-1} \left(\frac{L}{L_\odot}\right)^{-1}, \tag{2.2}$$

where L is the luminosity of a given star. Lastly, the nuclear timescale refers to the time in which a star would radiate away all the energy released from the nuclear reactions. It can be estimated by the time in which all the hydrogen in the core turns into helium, in other words, the time a star spends in the main-sequence phase,

$$\tau_{\rm nuc} = 7 \times 10^{-4} \frac{Mc^2}{L} \simeq 10^{10} \text{ year} \left(\frac{M}{M_\odot}\right) \left(\frac{L}{L_\odot}\right)^{-1}, \tag{2.3}$$

where the denominator is the energy released by nuclear fusion, with c the speed of light in vacuum.

The Sun has an estimated nuclear timescale of the order of 10 billion years, much longer than its thermal and dynamical timescale, of 10 million years and half an hour, respectively ($\tau_{nuc} \gg \tau_{KH} \gg \tau_{dyn}$; Kippenhahn et al. 2013). Hence there is a higher probability of observing stars in the main-sequence, as they spend most of their lives in this stage. As a star switches from nuclear sources, and there is a departure from hydrostatic equilibrium, τ_{KH} and τ_{dyn} become relevant again, and as a consequence, later stages of evolution proceed more rapidly.

The energy production process occurring during the main-sequence phase highly depends on the chemical composition as well as on the initial mass of stars. Following the convention in Karttunen et al. 2007,

for lower mass stars, roughly lower than 1.5 $M_\odot$ (e.g., the Sun), the central temperature is lower than for massive stars, so hydrogen is fused into helium via proton-proton (pp) chains:

$$4\ {}^1\mathrm{H} \ \rightarrow\ {}^4\mathrm{He} + 2\mathrm{e}^+ + 2\nu_e\ , \tag{2.4}$$

releasing 26.73 MeV per nuclear reaction (Carroll and Ostlie 2007), where e^+ denotes a positron and ν_e denotes the electron neutrino. Stars with masses above 1.5 $M_\odot$ reach higher temperatures in their cores, thus the dominant energy production mechanism is the Carbon-Nitrogen-Oxygen (CNO) cycle. This mechanism consists of successive reactions using isotopes of C, N and O as catalysts to convert H into ^{4}He. The CNO cycle is strongly dependent on the temperature ($\epsilon_{CNO} \sim T^{17}$, Carroll and Ostlie 2007) hence its energy production is highly concentrated in the core. In massive stars interiors the temperature gradient is too steep that it reaches the physical limit, known as Schwarzschild criterion, where energy transport can no longer be sustained by radiation consequently becoming convectively unstable. Therefore, convection assures an efficient transport of energy and mixing of the internal composition in the core of those stars, in contrast with their envelope where there is no fusion so energy is carried trough radiation. In lower mass stars the opposite configuration is established – where radiative core is surrounded by a small convective envelope (e.g., Karttunen et al. 2007).

The end of the main-sequence phase is marked by the complete depletion of hydrogen in the core and is proceeded by the H-burning shell phase, as the requirements for helium burning in the core are not met yet. This transition takes place gradually in lower mass stars. Since the conditions in the core significantly impact the structure and evolution forward, our focus will be solely on the evolutionary path of stars with masses around 1.5 $M_\odot$ with radiative cores (as in Karttunen et al. 2007). Without central nuclear reactions the stellar core contracts and consequently releases gravitational potential energy. The temperature increases in the shell surrounding the core, which incites more nuclear reactions in that region and the total stellar luminosity rises. The build up pressure due to radiation will cause the envelope expansion and cool down, resulting in a decrease of the star's effective temperature. As follows, the star enters the subgiant branch (SGB) and it continues to move almost horizontally (to the right) in the HR diagram illustrated in figure 2.1.

As the convective envelope expands due to the increase of photospheric opacity at lower surface temperatures, the star reaches a limit where, in order to maintain hydrostatic equilibrium, has to evolve towards larger luminosities (e.g., Hekker and Christensen-Dalsgaard 2017). In this stage, the star begins to move upwards in the HR diagram, entering the so-called red giant branch (RGB). The mass of the inert degenerate helium core gradually increases with the deposit of helium from the H-burning happening in the shell, increasing its density. The central temperature and pressure also increase, boosting the energy generation in the shell.

Eventually the temperatures in the core reaches approximately 10^8 K and densities of 10^7 kg m^{-3}, sufficient to trigger the triple-alpha (3-α) process – which generates ^{12}C from the fusion of three alpha particles and additionally generates ^{16}O through a secondary reaction. Fusion initially takes place in the degenerate helium core that is essentially independent of temperature as it rises. The unstable burning conditions

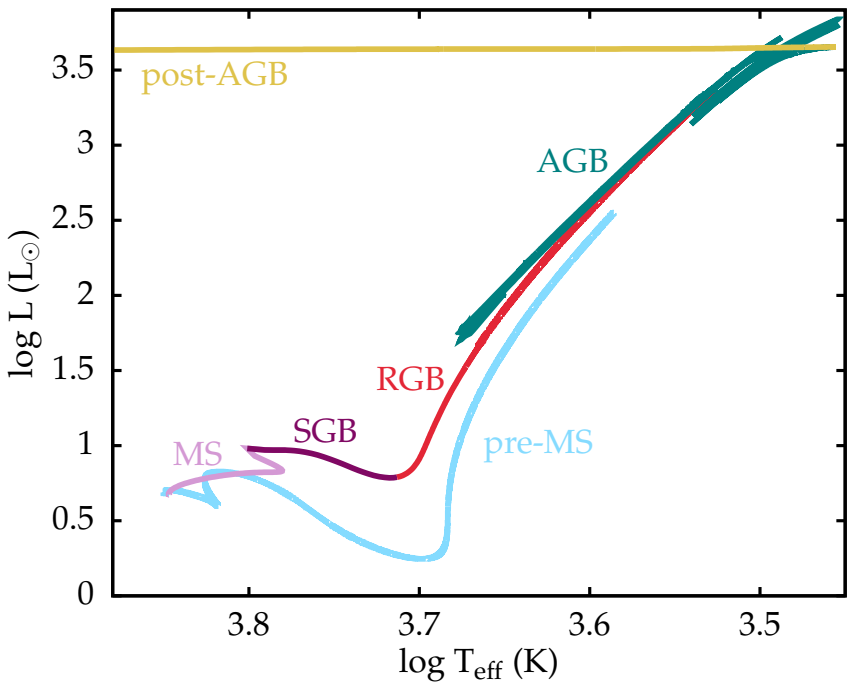

Figure 2.1: HR diagram showing the evolution of a MESA model with 1.5 $M_\odot$ at solar metallicity. The illustrated evolutionary track starts in the pre-main sequence (pre-MS, blue) phase, passing through the zero age main-sequence (ZAMS) entering in the main-sequence (MS, pink) phase. The model then evolves along the subgiant branch (SGB, purple) and up the red giant branch (RGB, red) until it enters the asymptotic giant branch (AGB, green). The post asymptotic giant branch (post-AGB, yellow) is followed by the white dwarf (WD) cooling sequence which is not represented.

result in a tremendous amount of energy being released in a matter of seconds. This run-away process is called *helium flash*, and the luminosity generated by the He-burning core reaches values in the order of 10^{11} $L_\odot$ (Carroll and Ostlie 2007). Stellar models predict subsequent smaller sub-flashes towards the center ultimately lifting the degeneracy in the core, and the star recovers equilibrium with He-burning in the center.

Once helium has exhausted in the core, the star enters the thermally pulsating phase in the asymptotic giant branch (AGB), where helium quasi-periodically ignites in the shell around the degenerate carbon-oxygen core, an aftereffect of the deposit of ashes from H-burning in upper shells. These intermittent helium shell flashes lead to the loss of large amounts of mass from the stellar envelope and cause abrupt changes in the surface luminosity along the asymptotic giant branch. The mass lost will latter constitute the so-called planetary nebula that will be, ultimately, dispersed into the interstellar medium (e.g., Karttunen et al. 2007).In the center, for this particular mass range, the conditions for carbon fusion are never met, thus the carbon-oxygen core contracts to a radius comparable to the Earth radius, remaining in a compact and extremely hot degenerate core, called a white dwarf (WD) (e.g., Kippenhahn et al. 2013).

2.1.1 Equations of stellar evolution of rotating stars

Stellar evolution codes usually assume spherical symmetry when computing structures of non-rotating non-binary stars without the presence of strong magnetic fields. This approximation allows to produce with high accuracy one dimensional (1D) stellar evolution and structure models characterized by one spatial coordinate (e.g., mass in the Lagrangian formalism) and time. However, since it is highly likely that all stars rotate (the molecular clouds from which they originate have acquired angular momentum), it is often important to consider rotation in stellar models. Rotation not only warps the equilibrium configuration (as we will see in this chapter), but it also triggers various phenomena such us internal circulation motions, hydrodynamic instabilities and mass loss, that ultimately lead to enrichment of a number of different elements on the stellar surface due to chemical mixing and transfer of angular momentum in stellar interiors, latter discussed in chapter 3.

The inclusion of rotation in stellar modeling (e.g., see Tassoul 1978; Maeder 2009) inherently implies a departure from spherical symmetry, requiring a 3D numerical approach to solve the full stellar structure equations. Currently, there are still many challenges implementing rotation using 2D (e.g., Rieutord et al. 2016) and 3D (e.g., Turcotte et al. 2004) methods, hence many widely used stellar evolution codes resort to 1D modeling by considering the so-called *shellular approximation* introduced by Zahn (1992). One writes the angular velocity Ω as

$$\Omega(r,\theta) = \overline{\Omega}(r) + \widehat{\Omega}(r,\theta) \ , \tag{2.5}$$

with θ the colatitude, which is the complementary angle of a given latitude, $\overline{\Omega}$ is the angular velocity of a rigidly-rotating shell, and $\widehat{\Omega}$ is the second order term to account for higher rotation velocities, defined in terms of the Legendre polynomials (e.g., see Maeder 2009).

Current models assume radial differential rotation, so that the core is rotating faster than the outer convective envelope. Consequently strong anisotropic turbulence develops in radiative regions with motion more vigorous in the horizontal direction erasing the existent compositional inhomogeneities along isobaric surfaces. The motion is much weaker in the vertical direction considering that the stable thermal gradient suppresses the fluid motions. Hence, the angular velocity profile depends very weakly on latitude and is almost constant on isobars $\overline{\Omega} \gg \widehat{\Omega}$ (shellular approximation; Zahn 1992). The last term in equation (2.5) is to account for cases of extreme rotation velocities, which will not be considered in the following derivation $\big(\Omega(r) = \overline{\Omega}(r)\big)$.

In this approach, the total potential Ψ is constant over isobaric surfaces, which differ from spherical shells. The total potential writes as a sum of the gravitational potential and the potential from which the centrifugal acceleration derives,

$$\Psi = \Phi - \frac{1}{2}\Omega^2 r^2 \sin^2\theta \ = \ \text{const.} \tag{2.6}$$

(e.g., Endal and Sofia 1976; Meynet and Maeder 1997; Maeder 2009) where in the *Roche approximation*, the gravitational potential of the mass M_r inside radius r is assumed not distorted by rotation, such that Φ is

given by the Newtonian potential $\Phi = -GM_{\rm r}/r$. In the Roche model the inner layers are assumed spherical, giving the same external potential as if the total mass of the star was concentrated at the center, which is a good approximation to real stars as most of their mass is highly condensed in the core. The centrifugal force term in equation (2.6) is what causes the deviation from the spherical symmetry in rotating stars. For rapid rotators one should expect a strong distortion, since it varies with Ω^2. For slow to moderate rotators the deformations in the stellar structure remain fairly negligible, nonetheless there is still a small distortion to be taken into account.

In literature, a criteria often used to establish whether the effects of rotation are significant is comparing the actual star's rotation velocity with its *critical velocity*. This last one, also called break-up velocity, is reached when the modulus of the centrifugal force becomes equal to the modulus of the gravitational force in the equatorial plane. The classical expression for the critical velocity at the equator ($\theta = \pi/2$) is then

$$\Omega_{\rm e,crit} = \sqrt{\frac{GM}{R^3_{\rm e,crit}}} \ , \tag{2.7}$$

(e.g., Heger et al. 2000) where $R_{\rm e,crit}$ is the equatorial radius at break-up. The critical velocities grow with stellar masses (as the associated increase in stellar radius is small),and with lower metallicities (since their radii are smaller). Ultimately, the effect of rotation in the stellar surface (e.g., equatorial radius) is only visible in cases where the rotational velocity is notably close to the critical velocity. Maeder (2009) saw that up to $\Omega/\Omega_{\rm crit} = 0.7$ the increase of the equatorial radius is inferior to 10%.

The stellar structure equations for rotating stars implemented in several widely used stellar evolution codes, such as the Modules for Experiments in Stellar Astrophysics (MESA; Paxton et al. 2013, 2019), make use of the shellular approximation (following the approach of Meynet and Maeder 1997) and take into account effects of centrifugal acceleration (Kippenhahn and Thomas 1970; Endal and Sofia 1976).

The equation of continuity preserves the same form as for a non-rotating star, by re-defining the radius coordinate as the volume-equivalent $V_p = 4\pi r_p^3/3$ radius r_p of an isobar S_p:

$$\frac{\partial\, r_p}{\partial m_p} = \frac{1}{4\pi r_p^2 \rho} \ , \tag{2.8}$$

where ρ is the density and m_p the mass enclosed by the surface area S_p.

The equation of motion or momentum balance can be derived from the hydrostatic equilibrium equation $\nabla \mathbf{p} = \rho\ \mathbf{g}_{\rm eff}$, where the effective gravity $\mathbf{g}_{\rm eff}$ cannot be defined as in the conservative potential case, and is otherwise defined as

$$\mathbf{g}_{\rm eff} = \left(-\frac{GM_{\rm r}}{r^2} + \Omega^2 r^2 \sin^2\theta \ ,\ \Omega^2 r \sin\theta\cos\theta \ ,\ 0 \right) \ . \tag{2.9}$$

$$\frac{\partial p}{\partial m_p} = -\frac{Gm_p}{4\pi r_p^4} f_P - \frac{1}{4\pi r_p^2} \left(\frac{\partial^2 r_p}{\partial t^2} \right)_{m_p} \ , \tag{2.10}$$

is the equation of motion where $\partial^2 r_p/\partial t^2$ is the inertia term, which must vanish to regain 1D hydrostatic equilibrium. This modified equation of motion describes the pressure p evolution in each isobaric layer of

the star and the influence of rotation is described by the *form factors*

$$f_p = \frac{4\pi r_p^4}{GM_pS_p}\frac{1}{\langle g_{\rm eff}^{-1}\rangle} \qquad \text{and} \qquad f_T = \left(\frac{4\pi r_P^2}{S_P}\right)^2 \frac{1}{\langle g_{\rm eff}\rangle\langle g_{\rm eff}^{-1}\rangle}\ , \tag{2.11}$$

where $g_{\rm eff} \equiv |\mathbf{g}_{\rm eff}|$ with $g_{\rm eff}$ the effective gravitational acceleration normal to S_p and the averages are performed over each isobar (Meynet and Maeder 1997). The quantities f_p and f_T reduce to 1 in non-rotating models, differing from 1 the most in the outer stellar layers of fast rotators.

The energy transport equation that describes how energy is transported at each layer of the star, can be written as

$$\frac{\partial T}{\partial m_p} = \frac{Gm_pT}{4\pi r_P^4 p}\nabla\ , \tag{2.12}$$

where T is the temperature and $\nabla \equiv \partial \ln T/\partial \ln p$ is the temperature gradient, a quantity that is used to test whether a zone is stable or unstable against convection. From a computational perspective, the calculation of the energy transport in stellar interiors needs to be divided into radiative and convective zones.

In the case of radiative transfer located in stellar atmospheres, the problem is non-trivial and it must be solved in combination with the hydrodynamic equations. In stellar interiors a diffusion approximation to the radiative transfer is adequate, owing to the very short photon mean free path in comparison to the length scales of stellar structure variations (Maeder 2009). Hence, for stellar interiors this is given by

$$\nabla = \nabla_{\rm rad} = \frac{3\kappa}{16\pi acG}\frac{p}{T^4}\frac{L_p}{m_p}\frac{f_T}{f_p}\ , \tag{2.13}$$

with a the radiation density constant, κ is the opacity and L_p is the energy flux through S_p.

In convection zones, on the other hand, the turbulent gas motions provide a very efficient and complex transport of energy, resulting in equations far to complex to be handled analytically or numerically under most circumstances. Therefore the so-called *mixing-length theory* (MLT; Houdek and Dupret 2015) is usually implemented, despite being a rough approximation since it dismisses the turbulent pressure. It is characterized by the free parameter α_{MLT}, that accounts for the mean free path over which the convective eddies travel before dissipating.

The energy conservation equation also retains its usual, non-rotating form

$$\frac{\partial L_p}{\partial m_p} = \epsilon_{\rm nuc} - \epsilon_\nu + \epsilon_{\rm grav}\ , \tag{2.14}$$

where $\epsilon_{\rm nuc}$ is the specific energy rate generation for the total nuclear reaction, ϵ_ν is the specific thermal neutrino loss rate and $\epsilon_{\rm grav}$ is the specific rate of change of gravitational energy due to contraction or expansion.

The equations (2.8), (2.10), (2.12),(2.14) are the basic equations for the hydrostatic equilibrium of stars with shellular rotation, that can be solved numerically if complemented with an appropriate equation of state, tabulated opacities, network of nuclear reaction rates, element diffusion data and atmosphere boundary conditions.

2.2 Stellar Pulsations

2.2.1 Hydrodynamic equations

This section presents the theoretical background for the computation of stellar oscillations, based on Aerts et al. (2010). Formally the equations of stellar oscillations are derived by performing small perturbations to a spherical equilibrium state, determined by the four general equations of hydrodynamics without rotation effects.

The first equation is the continuity or mass conservation equation (2.15), which relates the mass change with time in a given volume V with its flux entering that given volume (with the fluid velocity $\mathbf{v}$). Secondly is the equation of motion or momentum conservation (2.16) that describes the motion caused by various contributing forces. In stellar interiors one can ignore the internal friction in the gas (assuming zero viscosity) and other external forces (i.e., magnetic fields), only remaining the pressure and gravity forces. The third equation is the Poisson equation (2.17), where the gravitational acceleration can be written as the gradient of the gravitational potential Φ. Lastly, there is the energy equation (2.18) obtained through a combination between the continuity equation and the first law of thermodynamics, expressing that the heat gain dq/dt comes both from the variation in the internal energy E and work of expanding or compressing the gas.

$$\frac{\partial \rho}{\partial t} + \nabla \cdot (\rho \mathbf{v}) = 0 \,, \tag{2.15}$$

$$\rho \frac{\partial \mathbf{v}}{\partial t} + \rho(\mathbf{v} \cdot \nabla \mathbf{v}) = -\nabla p - \rho \nabla \Phi \,, \tag{2.16}$$

$$\nabla^2 \Phi = 4\pi G \rho \,, \tag{2.17}$$

$$\frac{dq}{dt} = \frac{dE}{dt} - \frac{p}{\rho^2}\frac{d\rho}{dt} \,. \tag{2.18}$$

In the adiabatic regime, where processes causing excitation or damping of oscillations are ignored, the heating term in the energy equation can be neglected to a high degree of precision, thus simplifying the calculation of oscillation frequencies. In this conditions equation (2.18) becomes

$$\frac{dp}{dt} - \Gamma_1 \frac{p}{\rho}\frac{d\rho}{dt} = 0 \,, \qquad \text{where } \Gamma_1 = \left(\frac{\partial \ln p}{\partial \ln \rho}\right)_{\mathrm{ad}} \,, \tag{2.19}$$

the subscript 'ad' refers to derivatives taken at constant entropy. Near the surface, however, the timescale of oscillations becomes comparable to the thermal timescale (equation 2.2) so the full energy equation must be taken into account (Christensen-Dalsgaard 1997).

This equation, together with the equations (2.15), (2.16) and (2.17), form the complete set of equations for adiabatic motion, which are still far to complex to solve analytically or even numerically. The already mentioned perturbation analysis obtains useful and valid simplifications to this equations, since the amplitudes of solar oscillations are very small compared with the dimension of the Sun (e.g., Aerts et al. 2010).

The thermodynamic quantities p, ρ, ϕ and $\mathbf{v}$ are continuous functions of time t and position r, and can be written as their value in the equilibrium configuration (with a subscript '0'; i.e., X_0) plus a small perturbative contribution. The equilibrium structure is assumed to be static and velocities are ignored. It is convenient

to use a description of the evolution of a field where the observer is stationary. The former is called the *Eulerian* description, where a scalar quantity X can be written as

$$X(\mathbf{r}, t) = X_0(\mathbf{r}) + X'(\mathbf{r}, t) \ , \tag{2.20}$$

with X' denoting a small perturbation in this description. In turn, it is also useful to use the already mentioned *Lagrangian* description, with an observer following the motion of the field. If the fluid suffers a displacement $\boldsymbol{\delta}\mathbf{r}$ from the equilibrium configuration, X can be written as

$$X(\mathbf{r}_0 + \boldsymbol{\delta}\mathbf{r}) = X_0(\mathbf{r}_0) + \delta X(\mathbf{r}) \ , \tag{2.21}$$

where δX is the perturbation in this description. The Eulerian and Lagrangian perturbations are related to each other by the expression below (left) which is completely equivalent to the expression below (right), that shows the relation between the local and the material time derivative:

$$\delta X = X' + \boldsymbol{\delta}\mathbf{r} \cdot \nabla X_0 \ , \qquad \left(\frac{dX}{dt}\right)_{Lag.} = \left(\frac{\partial X}{\partial t}\right)_{Eul.} + \mathbf{v} \cdot \nabla X \ , \tag{2.22}$$

with $\mathbf{v} = d\mathbf{r}/dt$ and $\mathbf{r} = \mathbf{r}_0 + \boldsymbol{\delta}\mathbf{r}$. Comparing both expressions in (2.22), one can obtain that the velocity is given by the time derivative of the displacement $\mathbf{v} = \frac{\partial \boldsymbol{\delta}\mathbf{r}}{\partial t}$, by neglecting higher order terms.

The energy equation (2.19) involves calculating total time derivatives, so to first order in the perturbations one can obtain the total time derivative of a quantity X as follows

$$\frac{dX}{dt} = \left(\frac{\partial}{\partial t} + \mathbf{v} \cdot \nabla\right)(X_0 + X') = \frac{\partial X'}{\partial t} + \mathbf{v} \cdot \nabla X_0 = \frac{\partial}{\partial t}\left(X' + \boldsymbol{\delta}\mathbf{r} \cdot \nabla X_0\right) = \frac{\partial \delta X}{\partial t}. \tag{2.23}$$

The full linearized fluid equations listed below are obtained by inserting the expressions (2.20) or (2.21) in the full set of equations for adiabatic motion, and subtracting the equilibrium equations, neglecting quantities of order higher than one.

$$\rho' + \nabla(\rho_0 \boldsymbol{\delta}\mathbf{r}) = 0 \ , \tag{2.24}$$

$$\rho_0 \frac{\partial^2 \boldsymbol{\delta}\mathbf{r}}{\partial t^2} = -\nabla p' - \rho_0 \nabla \Phi' - \rho' \nabla \Phi_0 \ , \tag{2.25}$$

$$\nabla^2 \Phi' = 4\pi G \rho' \ , \tag{2.26}$$

$$p' + \boldsymbol{\delta}\mathbf{r} \cdot \nabla p_0 = \Gamma_{1,0} \frac{p_0}{\rho_0}(\rho' + \boldsymbol{\delta}\mathbf{r} \cdot \nabla \rho_0) \ . \tag{2.27}$$

2.2.2 Equations of Linear Stellar Oscillations

Solutions to the perturbed stellar structure equations above can be simplified by excluding the Lorentz and Coriolis force, leaving the pressure and gravity as the only forces at play. Therefore, a spherically symmetric equilibrium configuration is adopted and generally described using a spherical coordinate system (r, θ, ϕ), where r is the distance to the center of the star, θ is the colatitude (coincides with the rotation axis), and ϕ is the longitude (e.g., Aerts 2021). In this coordinates the displacement δr can be decomposed into radial and horizontal components, such that

$$\boldsymbol{\delta}\mathbf{r} = \xi_r \mathbf{e}_r + \boldsymbol{\xi}_h = \xi_r \mathbf{e}_r + \xi_\theta \mathbf{e}_\theta + \xi_\phi \mathbf{e}_\varphi \ , \tag{2.28}$$

where $\mathbf{e}_i$ is the unit vector in the respective direction.

Additionally, the simplifications in the linearized stellar structure equations lead to separable solutions in terms of r, θ, ϕ and t. The time dependence is given by $e^{-i\omega t}$, where ω is the angular frequency. The angular dependence is given by the spherical harmonics $Y_l^m(\theta,\varphi) = (-1)^m\, c_{lm}\, P_l^m(\cos\theta)\, e^{im\varphi}$, where c_{lm} is a normalization constant and P_l^m are the Legendre polynomials characterized by the spherical degree l and azimuthal order m, that obey $|m| \leq l$.

The (physical) displacement vector (analogously to the other dependent variables ρ', p' and Φ') can now be written, as function of position $\mathbf{r}$ and time t,

$$\boldsymbol{\delta}\mathbf{r}(\mathbf{r},t) = \sqrt{4\pi}\ \mathrm{Re}\left\{\left(\xi_r(r)\ Y_l^m,\ \xi_h(r)\ \frac{\partial Y_l^m}{\partial\theta},\ i\xi_h(r)\ \frac{m}{\sin\theta}Y_l^m\right)e^{-i\omega t}\right\}\ , \tag{2.29}$$

(Aerts et al. 2010) where ξ_r and ξ_h are the radial and horizontal displacement amplitude functions, respectively.

After some algebraic manipulation of equations (2.24)-(2.27) and applying the expression above, the equations of linear adiabatic stellar oscillations can be written as

$$\frac{d\xi_r}{dr} = -\left(\frac{2}{r} + \frac{1}{\Gamma_{1,0}p_0}\frac{dp_0}{dr}\right)\xi_r + \frac{1}{\rho_0 c_s^2}\left(\frac{S_l^2}{\omega^2} - 1\right)p' + \frac{l(l+1)}{\omega^2 r^2}\Phi'\ , \tag{2.30}$$

$$\frac{dp'}{dr} = \rho_0\left(\omega^2 - N^2\right)\xi_r + \frac{1}{\Gamma_{1,0}p_0}\frac{dp_0}{dr}p' - \rho_0\frac{d\Phi'}{dr}\ , \tag{2.31}$$

$$\frac{1}{r^2}\frac{d}{dr}\left(r^2\frac{d\Phi'}{dr}\right) = 4\pi G\left(\rho_0\frac{\xi_r}{g_0}N^2 + \frac{p'}{c_s^2}\right) + \frac{l(l+1)}{r^2}\Phi'\ , \tag{2.32}$$

where $c_s^2 = \Gamma_{1,0}p_0/\rho_0$ is the adiabatic sound speed squared, S_l is the *Lamb frequency*

$$S_l^2 = \frac{l(l+1)c_s^2}{r^2}\ , \tag{2.33}$$

and N is the *Brunt-Väisälä* or *buoyancy frequency*

$$N^2 = g_0\left(\frac{1}{\Gamma_{1,0}p_0}\frac{dp_0}{dr} - \frac{1}{\rho_0}\frac{d\rho_0}{dr}\right)\ . \tag{2.34}$$

The fourth-order set of equations (2.30)-(2.32) with four dependent variables ξ_r, p', Φ', $d\Phi'/dr$ can only be solved by providing four adequate boundary conditions (e.g., in the center and surface of the star), discussed in great detail by Cox (1980) and Unno et al. (1989). The mode frequencies ω are the respective eigenvalues of this system of equations described by the quantum numbers, n, l and m. For a radii $r \in [0;R]$, n consists of the number of nodes between r and the surface of the star R (by convention labeled with $n > 0$ for radial modes, where the mode with $n = 0$ is the fundamental frequency; Unno et al. 1989); for nonradial modes n is the number of nodes below r (labeled with $n < 0$). l represents the number of nodal lines on the surface and m the number of nodal lines crossing the stellar equator. The assumption of spherical symmetry leads to a solution independent of m.

2.3 Asymptotic theory of stellar oscillations

It is often useful to reduce the previous system of equations to second order by neglecting the perturbation to the gravitational potential $|\Phi'|$ (and analogously its derivative $d\Phi'/dr$) since it is small compared to the perturbation to the density ρ'. This approximation known as the *Cowling approximation* (Cowling 1941) is adequate when the spherical degree l and the radial order $|n|$ are large. Despite being a rough first approximation to the equations of nonradial oscillations, it gives a good approximation to the mode frequencies and is generally valid when applying to observed modes of solar oscillations and solar-like oscillations in other stars.

For oscillations of high radial order, the derivatives of the equilibrium quantities ($\frac{dp_0}{dr}$) in the equations (2.30) and (2.31) can be neglected, due to the faster variation of eigenfunctions in comparison with equilibrium quantities. The first term of equation (2.30) ($-\frac{2}{r}\xi_r$) can also be neglected in this regime. At last, the set of equations (2.30)-(2.32) is reduced to

$$\frac{d\xi_r}{dr} = \frac{1}{\rho c_s^2}\left(\frac{S_l^2}{\omega^2} - 1\right) p' \,, \tag{2.35}$$

$$\frac{dp'}{dr} = \rho\left(\omega^2 - N^2\right)\xi_r \,, \tag{2.36}$$

where the subscript '0' for equilibrium quantities was omitted. Combining these two equations one obtains

$$\frac{d^2\xi_r}{dr^2} \simeq \frac{\omega^2}{c_s^2}\left(1 - \frac{N^2}{\omega^2}\right)\left(\frac{S_l^2}{\omega^2} - 1\right)\xi_r \qquad \Rightarrow \qquad \frac{d^2\xi_r}{dr^2} + K^2\xi_r = 0 \,. \tag{2.37}$$

A positive sign of the radial wave-number K^2 determines an oscillatory solution for the equation 2.37. Since stellar oscillations are standing waves driven by restoring forces, pressure and gravity, they are *trapped* in a zone limited by points where $K = 0$, known as *turning points* of the waves (radii where $\omega = S_l$ or $\omega = N$). Stellar oscillations are sensitive to the structure of the trapping region (also known as *mode cavity*). High frequency oscillations ($|\omega| > |N|, S_l$) are excited by pressure, hence are labeled *p-modes*, whereas lower frequency oscillations ($|\omega| < |N|, S_l$) are excited by buoyancy and are labeled *g-modes*. Outside the mode cavities, the negative sign of K^2 leads to an exponentially decaying motion, meaning that the modes are evanescent in those regions ($|N| < |\omega| < S_l$ or $S_l < |\omega| < |N|$).

Several oscillation modes have been detected in the Sun, with periods in the range of 3-15 minutes (Claverie et al. 1980; equivalent to high frequencies). These modes are stochastically excited by convective noise - p-modes - with high amplitudes when reaching the stellar surface thus probing the envelope structure. Since g-modes are anticipated to be confined in the inner radiative regions and decay exponentially within convective regions, they have only a residual amplitude at the surface. Until now, attempts to observe g-modes in the solar surface have proven to be unsuccessful, despite the controversial detection and interpretation of individual modes at low amplitude (García et al. 2007). Figure 2.2 (left) illustrates a propagation diagram for a 1 $M_\odot$ main sequence star with the mode cavities for pure p- and g-modes.

In the subgiant stage of low to intermediate mass stars, the core contraction and subsequent envelope expansion leads to an increase of Brunt-Väisälä frequency in radiative interiors, therefore g-mode frequen-

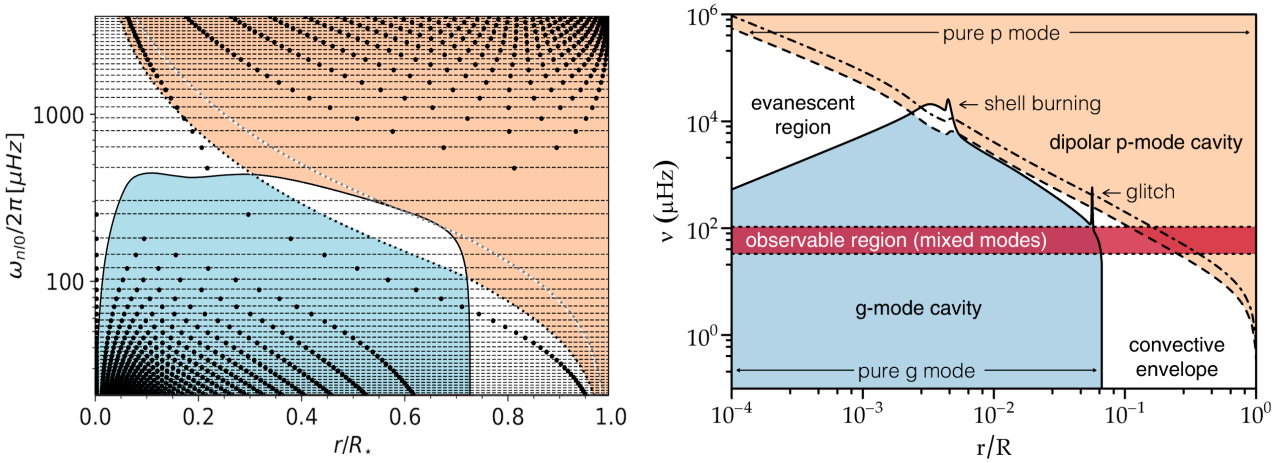

Figure 2.2: Propagation diagrams illustrating the mode cavities of p- and g-modes for two 1 $M_\odot$ models, in core H-burning (left) and shell H-burning (right) stage of evolution. The blue region is the g-mode cavity delimited by the Brunt-Väisälä frequency (full line), the orange region is the p-mode cavity delimited by the Lamb frequency (dashed lines for $l = 1$ and $l = 2$). The white region show evanescent regions. Left: The values of the dipole mode frequencies are indicated as black horizontal dashed lines. The position of the nodes of ξ_r are indicated as black dots for $l = 1$. Adapted from Aerts (2021). Right: The red band shows the observable region for mixed modes. Adapted from Christensen-Dalsgaard et al. (2020).

cies increase. In addiction, the mean density of stars decreases, hence the p-mode frequencies decrease. As a result, there is an overlap in the frequency domain of p and g-modes, therefore p-modes couple to the g-modes between the two oscillation cavities through the evanescent zone. Nonradial modes develop a mixed nature (predicted theoretically by Dziembowski (1971) and Shibahashi (1979)) exhibiting g-mode behavior in the convectively stable core of the star and p-mode behavior in the outer convective regions. Unlike pure g-modes which cannot be observed in solar-like oscillators, these so-called *mixed modes* have the potential to probe the entire star, and have been detected in *Kepler* data of evolved low mass stars (Beck et al. 2011; Bedding et al. 2011). The number of mixed modes increases as the stars evolves toward the red giant branch and the mode amplitude also increase in comparison to the main-sequence phase. The total number of nodal lines on the stellar surface also increases with higher angular degrees l, hence current observations are limited to modes with lower angular degree $l \leq 3$, due to the so-called *partial cancellation* (e.g., Aerts et al. 2010). Moreover, due to the lower density in the red giant branch, the mode oscillations periods increase to hours or even days.

Figure 2.2 (right) illustrates a schematic propagation diagram for a 1 $M_\odot$ red giant star that exhibits mixed mode character.

2.3.1 Asteroseismic diagnosis

Over the past decade, major improvements in high-resolution spectroscopy and the success of space missions such as MOST, CoRoT, Kepler, and most recently TESS have significantly increased the number of

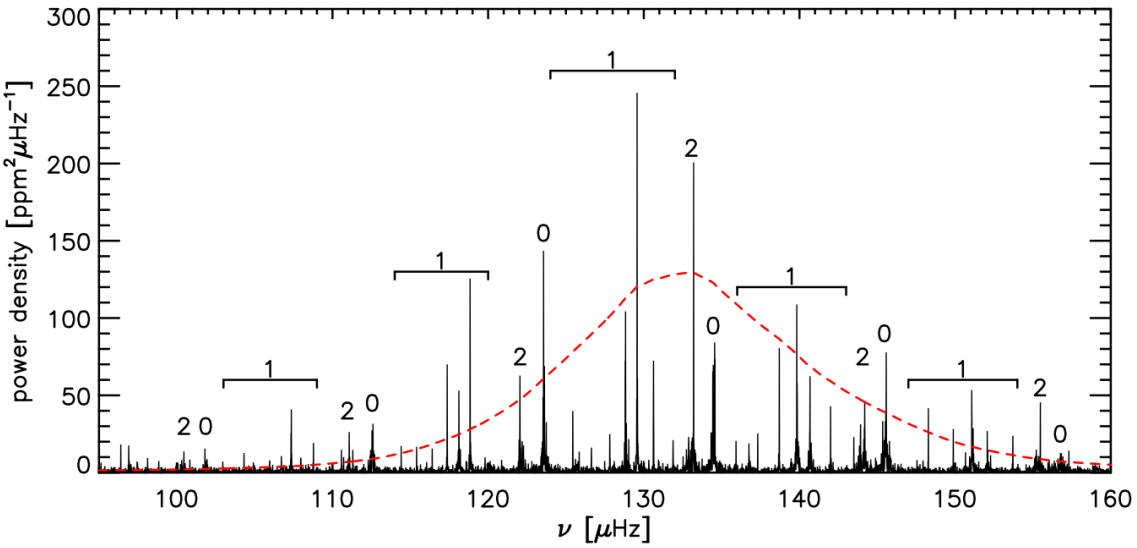

Figure 2.3: Power density spectrum of KIC 9145955. The numbers indicate the spherical degree (l) of the modes. The red dashed curve shows a smoothed bell-shaped curve centered around the frequency of maximum oscillation power. An estimated range for the observed mixed modes ($l = 1$) is indicated. Adapted from Hekker and Christensen-Dalsgaard (2017).

stars, particularly red giants, with detected nonradial oscillations and the resolution of oscillation patterns. Nonradial oscillations, specially of mixed modes, allow us to probe the stellar interiors at different depths of the stars acting as very important diagnostic tools in the study of stellar evolution theory.

Stellar oscillations of stochastic nature (triggered by turbulent motions in stellar convective envelopes), are detected in timeseries data of intensity variations (photometric fluxes) or radial-velocity variations. The timeseries data is transformed to the frequency space by performing a Fourier transform where the oscillation frequencies appear as sharp peaks in a Fourier power spectrum. Figure 2.3 shows the power density spectrum (PDS) of the red giant KIC 9145955. The individual modes are characterized by their frequencies, width, amplitudes, their overall shape and patterns in the PDS. Solar-like oscillations display a bell-shaped curve centered around a specific frequency in the PDS known as the *frequency of maximum oscillation power* $\nu_{\rm max}$. Measuring this quantity provides a direct measure to the surface gravity when the effective temperature is known $\nu_{\rm max} \propto g/\sqrt{T_{\rm eff}}$. To determine the solar mass and radius a simple approach using the following scaling relation is used:

$$\nu_{\rm max} = \left(\frac{M}{M_\odot}\right)\left(\frac{R}{R_\odot}\right)^{-2}\left(\frac{T_{\rm eff}}{T_{\rm eff,\odot}}\right)^{-1/2} \nu_{\rm max,\odot} \ , \tag{2.38}$$

(Kjeldsen and Bedding 1995) where $T_{\rm eff,\odot}$ = 5770 K, and $\nu_{\rm max,\odot}$ = 3090 $\pm$ 30 μHz as derived by Huber et al. (2011). An analogous scaling relation to equation 2.38 is often used for the frequency separation between consecutive radial-mode frequencies $\Delta\nu \equiv \nu_{nl} - \nu_{n-1\,l}$, known as the *large frequency separation*,

$$\Delta\nu = \left(\frac{M}{M_\odot}\right)^{1/2}\left(\frac{R}{R_\odot}\right)^{-3/2} \Delta\nu_\odot \ , \tag{2.39}$$

(Kjeldsen and Bedding 1995) where $\Delta\nu_\odot$ =135.1 $\pm$ 0.1 μHz (Huber et al. 2011).

For high radial order (meaning $n \gg l$), there is an asymptotic relation for pure acoustic modes that predicts approximately equally spacing $\Delta\nu$ in frequency. Following a first approximation by Tassoul (1980), the frequencies of acoustic modes follow the distinct pattern

$$\nu_{nl} \equiv \frac{\omega_{nl}}{2\pi} \simeq \left(n + \frac{l}{2} + \epsilon\right) \Delta\nu - d_{nl} \ , \tag{2.40}$$

with $\epsilon_{n,l}$ being a frequency dependent phase shift of the acoustic modes and $d_{n,l}$ a small corrective parameter (e.g., zero for $l = 0$). The regular structure of p-mode spectra predicted by asymptotic theory can be observed through the sequence of modes with $l = 0$ and $l = 2$ in figure 2.3 (effectively with less definition than in the case of pure p-modes). The large frequency separation is very sensitive to the sound speed c_s on the outer regions, hence it can be used to estimate the propagation time of sound waves across the star,

$$\Delta\nu = \left(2 \int_0^R \frac{dr}{c_s(r)}\right)^{-1} \ . \tag{2.41}$$

The frequency pattern for high-order g-modes in the inner radiative region can be obtain from the asymptotic approximation for a non-rotating star resulting in a spectrum nearly uniformly spaced in period satisfying the following relation by Tassoul (1980):

$$\Delta\Pi_l = \frac{2\pi^2}{\sqrt{l(l+1)}} \left(\int_{r_1}^{r_2} \frac{N}{r} dr\right)^{-1} = \frac{\Pi_0}{\sqrt{l(l+1)}} \ , \tag{2.42}$$

where r_1 and r_2 correspond to the inner and outer positions of the g-mode cavity, respectively, and the quantity Π_0 stands for the buoyancy travel time. The value of $\Delta\Pi$ has a strong diagnostic power in the inner regions of stars. In fact, it allows to clearly distinguish two different stages in the red giant branch, stars with an inert core from stars with core He-burning (Bedding et al. 2011; Mosser et al. 2011). Additionally, deviations from asymptotic values can bring insight to inner structure changes triggered by chemical discontinuities due to the first dredge-up (Cunha et al. 2015).

Due to the mixed nature in evolved stars, the period spacing of oscillation modes (equation 2.42) suffers a departure from asymptotic predictions. The $\Delta\Pi$ is smaller for p-dominated mixed modes (e.g., contain multiple mixed modes per p-mode order) and increases for g-dominated mixed modes ($\Delta\Pi$ evolves towards the asymptotic value for modes with more g-dominated character). This feature is illustrated in the PDS of figure 2.3, where dipole modes are presented as several peaks with different frequencies for p- and g-dominated mixed modes instead of only one has presented for $l = 0$ and $l = 2$ modes where there are mainly p-modes.

The relative contributions of different regions of the star to a mixed mode are usually characterized by the *normalized inertia* $E_{\rm norm}$. This is defined in Hekker and Christensen-Dalsgaard (2017) and can be written as

$$E_{\rm norm} = \frac{4\pi \int_0^R \left[\xi_r(r)^2 + l(l+1)\xi_h(r)^2\right] \rho r^2 dr}{M \left[\xi_r(R_{\rm phot})^2 + l(l+1)\xi_h(R_{\rm phot})^2\right]} \ , \tag{2.43}$$

where $R_{\rm phot}$ is the photospheric radius and the rest of the quantities are their usual definitions. The value of $E_{\rm norm}$ is much higher for g-dominated mixed modes than for p-dominated ones.

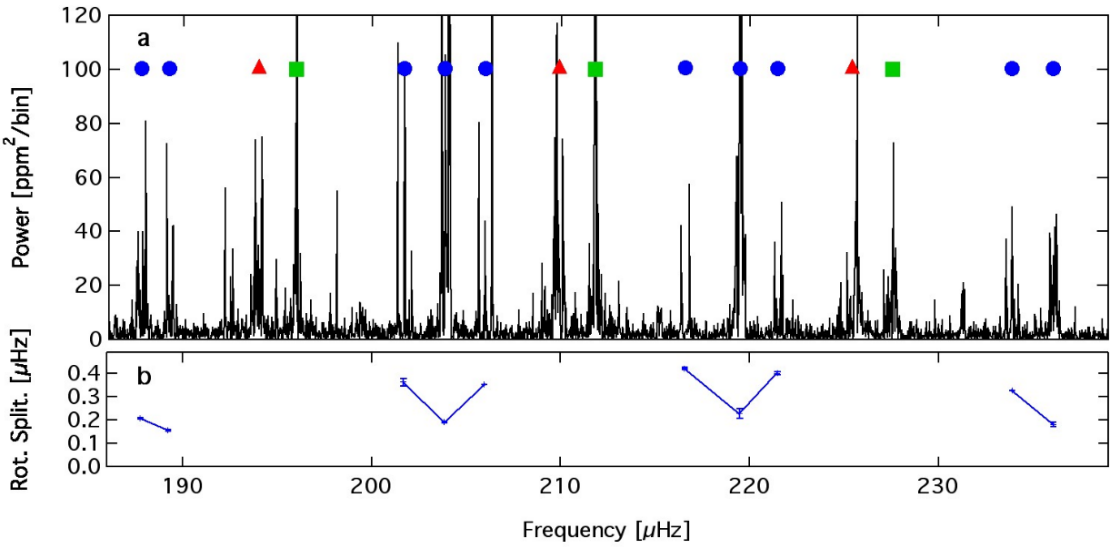

Figure 2.4: Panel a: Illustrates the oscillation spectrum of KIC 5356201, indicating radial modes (green squares), l=2 modes (red triangles) and l=1 rotational multiplets (blue circles). Panel b: Shows the observed rotational splitting for individual l=1 modes. Adapted from Beck et al. (2012).

Hundreds of stars in *Kepler* data showed decreasing $\Delta\Pi$ with increasing mode period, revealing a "tilted" pattern (e.g., see Aerts 2021). These slope is a consequence of the star rotation and we will discuss its implications in the adiabatic stellar oscillations equations in the next section.

2.3.2 Impact of rotation on oscillation frequencies

In the absence of rotation, frequency modes of different m values are degenerate due to spherically symmetry. In rotating stars, the Coriolis force lifts this degeneracy, and modes with different m split into $2l+1$ frequency components. Measurements of this rotational splitting were performed in early analysis of red giants in *Kepler* data (Beck et al. 2012) revealing that red giant cores rotate approximately ten times faster than the surface. Rotational splittings constitute a crucial diagnostic tool of stellar interiors along with $v \sin i$ spectroscopic measurements, bringing knowledge of the internal rotation of stars as inferred in recent results (e.g., Mosser et al. 2012; Vrard, M. et al. 2016) and possible constraints on rotationally induced internal chemical mixing. Figure 2.4 illustrates the rotational frequency splitting in dipole mixed modes.

In slowly rotating stars, where the rotation frequency is well below the oscillation frequencies $2\Omega/\omega \ll 1$, the Coriolis force can be treated as a small perturbation in the equations of adiabatic stellar oscillations (equations (2.30)-(2.32)). This generally applies for slow rotators such as p- and mixed modes in red giants of low-mass stars (e.g., see Aerts 2021). Low frequency g-modes observed in the majority of intermediate- and high-mass stars have rotation periods similar to their pulsation period, so their modes occur in the gravito-inertial regime and require a nonperturbative approach when including the Coriolis force (Aerts et al. 2017). Currently this is performed by adopting the "Traditional Approximation of Rotation" (TAR; Lee and Saio 1987a, 1987b) and solving the Laplace tidal equations, subject that is out of the scope of this thesis.

In the frame corotating with the star, the Coriolis force leads to a purely geometric shift of oscillation frequencies of the multiplet components,

$$\omega_{nlm} = \omega_{nl} + m\Omega \ , \tag{2.44}$$

where ω_{nl} is the frequency in the nonrotating case. Shellular rotation is assumed so that the angular frequency $\Omega = \Omega(r)$ only depends on the radius, and, to account for differential rotation, Ω in equation (2.44) is replaced by the average

$$\langle \Omega \rangle \simeq \frac{\int \Omega |\boldsymbol{\delta r}|^2 dV}{\int |\boldsymbol{\delta r}|^2 dV}. \tag{2.45}$$

where $\boldsymbol{\delta r}$ is the radial displacement vector defined in equation (2.29). Hence the rotational splitting measures an average of the rotation rate over the stellar interior, determined by the mode properties. The first-order rotational splitting is given by

$$\delta\omega_{nlm} = m \ \beta_{nl} \int_0^R K_{nl}(r)\Omega(r)dr \ , \tag{2.46}$$

(see derivations in Unno et al. 1989; Aerts et al. 2010) where the *rotational kernel* K_{nl} is given by

$$K_{nl} = \frac{\left(\xi_r^2 + L^2\xi_h^2 - 2\xi_r\xi_h - \xi_h^2\right) r^2\rho}{\int_0^R \left(\xi_r^2 + L^2\xi_h^2 - 2\xi_r\xi_h - \xi_h^2\right) r^2\rho dr} \ , \tag{2.47}$$

with $L^2 \equiv l(l+1)$ and

$$\beta_{nl} = \frac{\int_0^R \left(\xi_r^2 + L^2\xi_h^2 - 2\xi_r\xi_h - \xi_h^2\right) r^2\rho dr}{\int_0^R \left(\xi_r^2 + L^2\xi_h^2\right) r^2\rho dr} \ . \tag{2.48}$$

For high-order p-modes the terms ξ_r^2 and $L^2\xi_h^2$ dominate, thus $\beta_{nl} \approx 1$. Since the neglected terms account for the Coriolis force, advection is the most responsible for the rotational splitting in p-modes. For high-order g-modes, the terms containing ξ_r can neglect, hence $\beta_{nl} \approx 1 - 1/L^2$.

Chapter 3

Rotation and Angular momentum

In the beginning of chapter 2 we discussed the departure from spherical symmetry in the stellar surface due to rotation and the alterations made to hydrodynamic equations to accommodate those effects. In this chapter we review other phenomena also directly correlated with rotation: gravity darkening, stellar winds, mixing of chemical elements and transport of angular momentum; that drastically influence the course of stellar evolution. Up to today, the physical knowledge in some of these phenomena is still limited and highly uncertain, nonetheless they are extremely important to be considered when building stellar models.

Lastly, we focus on processes of transport of angular momentum by magnetic fields subjected to instabilities in radiative stellar interiors and their potential to explain the discrepancies between computational models and current observations.

3.1 Impact of rotation in the stellar structure

As pointed out in chapter 2, the centrifugal force deforms the shape of the stellar surface from spherical symmetry (the equatorial radius becomes larger than the polar radius). The degree of this deformation depends on several parameters, such as the ratio between the actual velocity and the critical velocity, the degree of differential rotation, the stellar radius, etc. The centrifugal force also lowers the effective gravity in the equatorial regions relative to polar ones (see equation 2.9) – the so-called *gravity darkening* (von Zeipel 1924). This makes the stellar evolution tracks analogous to a non-rotating slightly less massive star, shifting the evolutionary tracks towards lower luminosity and effective temperature. The hydrostatic structure of faster rotators (e.g., intermediate to high mass stars) can be dramatically affected, on the other hand, in slowly rotating stars (e.g., low mass main-sequence and more evolved stars) these effects can generally be neglected.

The main effects of rotation on the evolution, however, result from the enhancement of mass loss (e.g. Maeder 2009) in massive stars and the development of anisotropies in the stellar winds (see e.g. Maeder and Meynet 2000; Georgy et al. 2011), leading to an enhanced polar mass flux. On the other hand, in the 1-2 $M_{\odot}$ range, rotation greatly impacts the mixing of the chemical elements and the transport of angular momentum from the inner to outer regions, in the convective or radiative zones (e.g., Endal and Sofia 1978).

3.2 Transport processes in stellar interiors

3.2.1 Evolution of angular momentum transport

There are several mechanisms that try to explain the physics of angular momentum redistribution in stellar interiors. Some of the most accepted mechanisms include hydrodynamic instabilities, meriodional circulations, torques due to magnetic fields and transport by internal gravity waves (see an extensive discussion in Aerts et al. (2019).

Large scale circulations in the meridian plane (e.g., Eddington-Sweet circulation by Sweet 1950) transport angular momentum through advection in radiative and convective regions. This circulation motions arise from the thermal imbalance created due to the deformation of isobars (that become much closer to each other in the polar regions than in the equatorial ones) by the centrifugal acceleration. Nowadays, there are still some uncertainties regarding the interactions with horizontal turbulence, magnetic fields and the amount of horizontal differential rotation generated by those interactions (Zahn 1992; Maeder 2009).

Hydrodynamic instabilities in radiative zones arise from the turbulent motions created by differential rotation mainly in phases with successive expansion and contraction of the star. These instabilities whether draw their energy from the increase in potential energy (due to entropy stratification and centrifugal force) or from the kinetic energy of the medium (e.g., Aerts et al. 2019). The last ones, the shear instabilities, have a significantly higher weight.

The implementation, in 1D stellar evolution codes, of hydrodynamic processes such as circulation and hydrodynamic instabilities described above showed that they can explain some transport in massive stars (e.g., Maeder and Meynet 2000). Nonetheless, torques generated by the majority of these processes scale as $(\Omega/N)^2$ and are rather ineffective, thus fail to explain the asteroseismic inferred core rotation rates of evolved stars, predicting spins two orders of magnitude higher (e.g., Heger et al. 2000; Cantiello et al. 2014), see figure 3.1.

Internal gravity waves (IGWs) are stronger candidates to explain the transport of angular momentum. With buoyancy as their dominant restoring force, they can transport angular momentum efficiently into radiative zones, in the presence of a certain amount of radial differential rotation, where they eventually dissipate. The work of Charbonnel and Talon (2005) with solar-like stars demonstrated the possibility for this phenomenon to explain the near rigid rotation profile of the Sun. At the interface between convective and radiative zones, it is predicted that the damped IGWs can travel forced by turbulent convective flux, hence have an impact in rotation in inner and outer regions of the stars (Rogers et al. 2013). Transport of angular momentum by IGWs in mixed modes was also studied by Belkacem et al. (2015a,b), and in g-modes in Townsend et al. (2017) (see an overview in Aerts 2021).

Magnetic fields are present in low mass stars and in convective envelopes of solar-like stars. Whether a dynamo can operate in a radiative zone with differential rotation remains a topic of discussion (e.g., Zahn et al. 2007; Maeder 2009). The torque imposed by a magnetic field would have important consequences in the

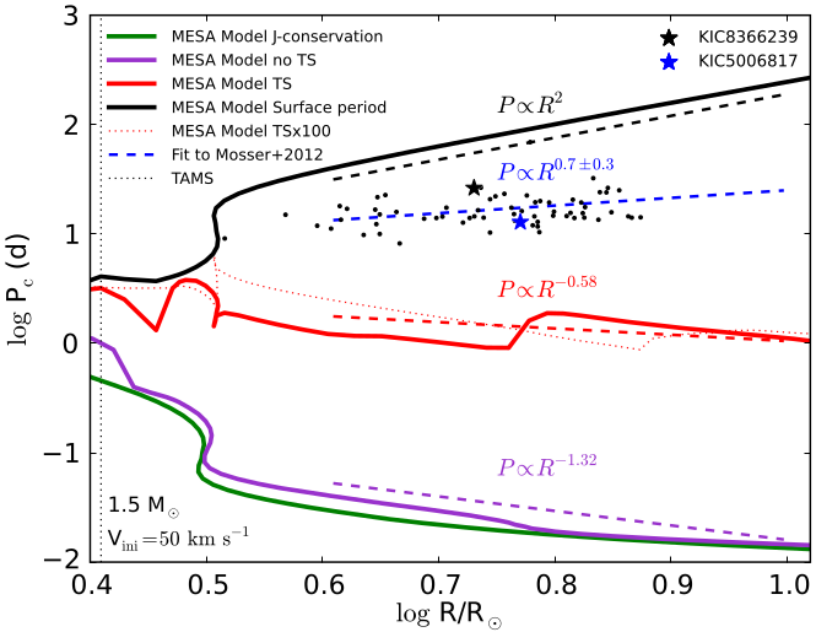

Figure 3.1: Evolution of the average core rotational period as a function of stellar radius of a 1.5 $M_\odot$ model with initial rotation of 50 km s $^{-1}$, for different angular momentum transport mechanisms. Illustrated are models without angular momentum transport (green), including transport of angular momentum due to rotational instabilities (purple) and due to magnetic torques in radiative regions (red; Tayler-Spruit dynamo). Red giants in the sample of Mosser et al. (2012) are shown as black dots. Adapted from Cantiello et al. (2014).

internal rotation profile, as this magnetic fields are subject to the instabilities: magnetorotational instability (MRI) and magnetohydrodynamical instability (e.g., the Tayler instability; Tayler 1973; Pitts and Tayler 1985). For example the Tayler-Spruit dynamo (Spruit 2002) mechanism based on this last instability, achieves rotation rates one order of magnitude higher than observations, regardless, it still predicts more efficient angular momentum transport than most candidates (see figure 3.1) A recent revision of this mechanism was performed by Fuller et al. (2019), most recently referred as the Fuller-formalism, that predicts stronger torques and higher efficiencies, overcoming previous limitations. There are also some other alternative candidates that predict opposite configurations, with differential rotation in the envelope and rigid rotation in radiative zones enforced by magnetic torques (Kissin and Thompson 2015).

The discrepancy between theory and asteroseismic observations of core rotation rates (e.g., den Hartogh et al. 2020) suggest that there must exist an additional process of transport of angular momentum from the inner to outer regions of stars. There is no consensus on which of the two processes above – IGWs or magnetic torques – is dominant since both still require calibrations of free parameters to reach the inferred rotation rates.

The inclusion of microscopic processes and convection along stellar evolution poses a real challenge to computational models due to the wide variety of spatial and temporal scales (e.g., Palacios 2013). Angular momentum transport is usually included using an advection-diffusion approach (as developed by Zahn 1992

and others) or only a diffusive approach (Endal and Sofia 1978; Pinsonneault et al. 1989; Heger et al. 2000). In this thesis we make use of the diffusion approximation as implemented in MESA (Paxton et al. 2013), where the transport of angular momentum as a diffusive process can be written as

$$\left(\frac{\partial \Omega}{\partial t}\right)_m = \frac{1}{i}\left(\frac{\partial}{\partial m}\right)_t \left[(4\pi r^2 \rho)^2 i \nu \left(\frac{\partial \Omega}{\partial m}\right)_t\right] - \frac{2\Omega}{r}\left(\frac{\partial r}{\partial t}\right)_m \left(\frac{1}{2}\frac{d\ln i}{d\ln r}\right) , \tag{3.1}$$

(Endal and Sofia 1978), where i is a shell specific moment of inertia, and ν is the turbulent viscosity calculated as the sum of the diffusion coefficients for convection, semiconvection, and rotationally induced instabilities (neglecting interactions such as amplification and damping between some instabilities). The first term on the right-hand side accounts for the diffusion transport and the second term is an advection term, accounts for contraction and expansion of the shells at constant mass.

3.2.2 Evolution of processes of chemical mixing

The transport of angular momentum mechanisms described above constitute the source of rotationally driven mixing, that transports chemical elements between layers in stellar interiors. Thus, the detection of surface chemical abundances can indirectly probe the angular momentum missing processes.

The evolution of chemical elements is computed separately from the transport of angular momentum. The enforced shellular rotation sweeps out compositional differences, leading to an approximately chemical homogeneous composition on isobars. This allows to solve the evolution of compositional mixing in a 1D diffusive approach, by solving the following equation

$$\left(\frac{\partial X_n}{\partial t}\right)_m = \left(\frac{\partial}{\partial m}\right)_t \left[(4\pi r^2 \rho)^2 D \left(\frac{\partial X_n}{\partial m}\right)_t\right] + \left(\frac{dX_n}{dt}\right)_{\rm nuc} , \tag{3.2}$$

(Heger et al. 2000), where X_n is the mass fraction for n'th nucleus, D is the diffusion coefficient determined as the sum of individual mixing processes (e.g., convection, semiconvection, thermohaline mixing and rotationally induced instabilities). The first term on the right-hand side accounts for diffusive transport and the second term is for nuclear reactions.

Mixing of nuclides modifies the elements stratification in the inner regions, and in particular, rotation-induced mixing is known to affect the evolutionary tracks in the HR diagram (Maeder and Meynet 2000). During the main-sequence phase, new hydrogen is brought into the core and the produced helium transported outwards. As a consequence, stars evolve with more luminosity and effective temperatures, larger helium cores, and extended lifetimes during core burning phases. In low to intermediate mass red giants, the convective envelope expands and penetrates deeper into the regions where nuclear reactions have altered the chemical composition, and some of these material is transported to the surface (e.g., see Aerts 2021).

In low mass stars on the red giant and asymptotic giant branch, the most representative observational tracer is the surface abundance of lithium (Somers and Pinsonneault 2016), due the lithium sensitivity to temperature and thus to the physics of internal transfer processes. Spectroscopic measurements of surface

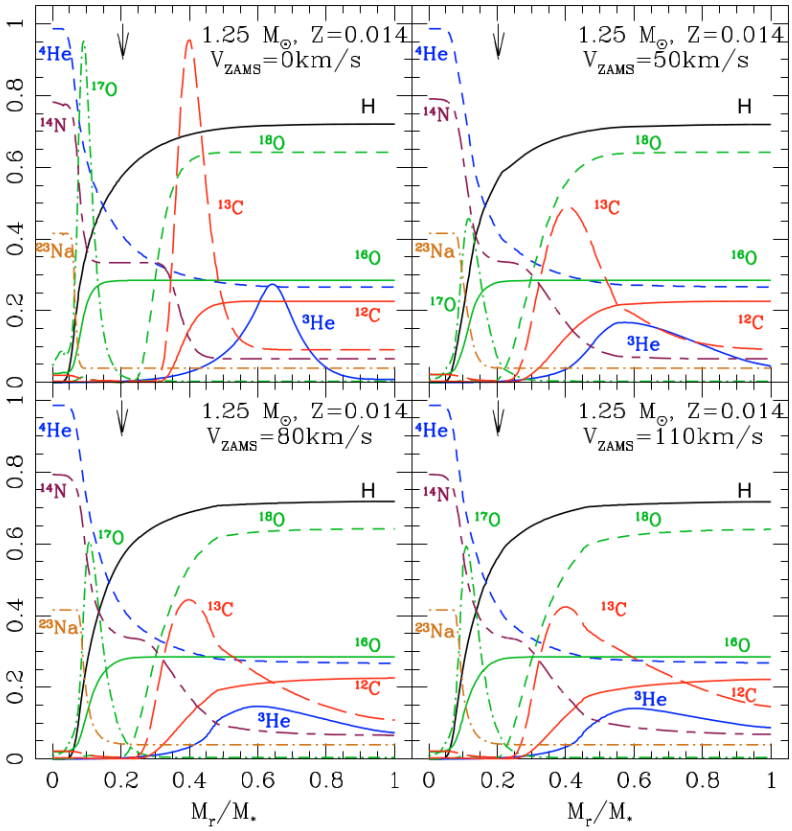

Figure 3.2: Mass fractions of the indicated chemical elements as a function of stellar mass for a 1.25 $M_\odot$ model at the end of core H-burning computed with different initial rotation velocities. All models include thermohaline and rotation-induced chemical mixing (except for the top left non rotating panel). The mass fractions are multiplied by 100 for ^{3}He, ^{12}C and ^{14}N, by 2500, 50, 900, 5×10^4 and 1500 for ^{13}C, ^{16}O, ^{17}O, ^{18}O , and ^{23}Na, respectively. Adapted from Charbonnel and Lagarde (2010).

abundances in red giants have shown evidence of a drop in lithium and carbon abundances, a sudden drop in the carbon isotopic ratio ^{12}C/^{13}C (Gratton et al. 2000), and a slight increase in nitrogen abundance (Frebel et al. 2005). Besides, abnormalities in the ^{3}He abundance in low mass stars (Lagarde et al. 2011) can possibly be explained by missing mixing processes. For example, in figure 3.2 one can see the effect of rotation in the abundances of ^{3}He, ^{12}C, ^{13}C and ^{17}O.

The nature of mixing of chemical elements in stellar interiors is still a heated topic. Recent studies have shown that rotationally induced mixing and meridional circulation alone do not produce enough mixing to explain the abundance anomalies observed around the so-called luminosity bump on the red giant branch (Hekker and Christensen-Dalsgaard 2017). Additional causes for mixing of chemical elements usually have to be considered such as semiconvective and thermohaline mixing. The last one has shown great potential explaining the observed surface abundances of low mass bright giant stars pass the red giant bump (Charbonnel and Lagarde 2010; Lagarde et al. 2011). Magnetism and IGWs are also expected to affect the mixing of chemical elements, however current implementations of the last one have shown a disagreement by orders of magnitude (Aerts 2021).

3.3 Tayler instability and dynamo formation

In this thesis we focus on the transport of angular momentum and rotationally-induced mixing generated by the Tayler-Spruit dynamo mechanism and the revised version by Fuller et al. (2019). In this section we summarize the process of formation and saturation of the Tayler instability, and the derived coefficients for diffusive transfer in stellar interiors for those mechanisms.

Spruit (2002) suggested that to generate a dynamo process there was no need for convection, or other velocity fields such as waves or shear turbulence, as otherwise stated. In fact, the generation of a magnetic field in a star only requires a strong differential rotation. In his description, latitudinal differential rotation shears an original weak fossil field (the radial component B_r) generating a toroidal field (B_ϕ) – the so-called Ω-effect. From the magnetic induction equation (see e.g. Denissenkov and Pinsonneault 2007), one can say that the toroidal field strength grows linearly as

$$\frac{\partial}{\partial t} B_\phi = q \Omega B_r \ , \tag{3.3}$$

where $q = -\partial \ln \Omega / \partial \ln r$ is the dimensionless shear and Ω is the angular rotation frequency. After a few turns, the field is predominantly azimuthal, $B_\phi \gg B_r$.

As B_ϕ grows, it becomes unstable for the first instability to set in, the Tayler instability (Tayler 1973; Pitts and Tayler 1985). A nonaxisymmetric instability, with m = 1 the fastest growing perturbation, that can take place in stably stratified regions (see e.g. Ma and Fuller 2019). This instability sets in only for unstable displacements that avoid doing work against the gas pressure (displacements nearly incompressible) and the buoyancy force (displacements nearly horizontal, along equipotential surfaces).

The B_ϕ critical strength for this instability to set in (Spruit 2002; Zahn et al. 2007) can be written as,

$$\omega_{\rm A} > \omega_{\rm c} \sim \Omega \left(\frac{N}{\Omega} \right)^{1/2} \left(\frac{\eta}{r^2 \Omega} \right)^{1/4} \ , \tag{3.4}$$

where ω_A is the Alfvèn frequency $\omega_A = B_\phi / \sqrt{4\pi\rho r^2}$ associated with B_ϕ, η is the magnetic diffusivity and N is the Brunt-Väisälä frequency.

As illustrated in figure 3.3, B_ϕ field lines can be seen as stacks of loops around the rotation axis. At saturation, the B_ϕ magnetic pressure between the field lines drives this kink-like instability to slip the field lines sideways with respect to each other an horizontal displacement $l_\perp$ coupled by a small radial displacement l_r. Due to a strong effect of the stratification, the radial length scale of the instability is limited to

$$l_r \sim l_\perp \frac{\omega_A}{N} \ , \tag{3.5}$$

where the maximum horizontal length scale is approximately $l_\perp \sim r$ (Ma and Fuller 2019). This radial displacement produces a weak poloidal B_r field (the so-called α-effect), that will be sheared again into a B_ϕ field by the Ω-effect. The alternation of the action of differential rotation and the radial displacements caused by the Tayler instability (Ω- and α-effect) close the dynamo loop.

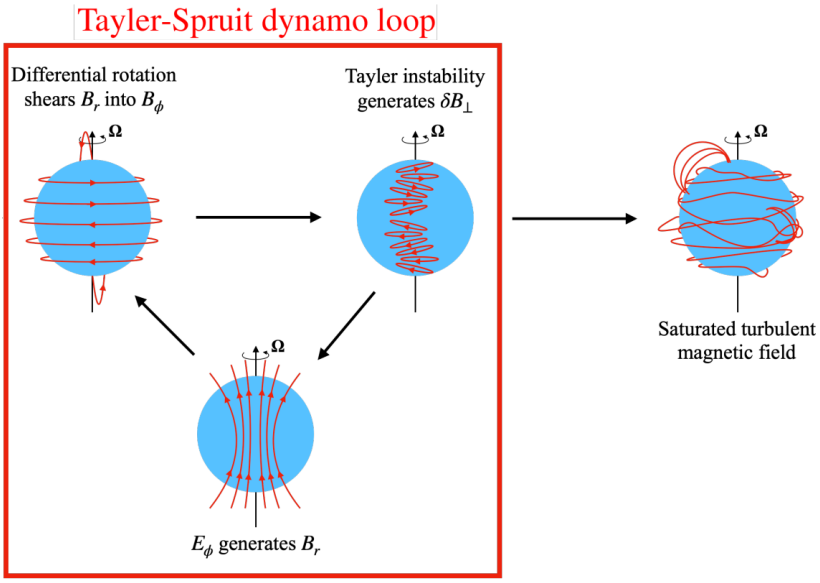

Figure 3.3: Schematic representation of the different stages of the Tayler-Spruit dynamo formation. Red lines represent the magnetic field lines. Adapted from Barrère et al. 2022.

A number of standard assumptions are used in this formulation: the frequencies are ordered such that $\omega_A \ll \Omega \ll N$; shellular rotation (Zahn 1992) is assumed ; the initial magnetic field is considered to be sufficiently weak so that initial magnetic forces can be neglected (Spruit 2002).

3.3.1 Spruit prescription

Spruit (2002) proposes that the energy in the background B_ϕ field is damped to small scales by a turbulent cascade as follows

$$\gamma_{\rm turb} \sim \frac{\omega_{\rm A}^2}{\Omega} \,, \tag{3.6}$$

$$\dot{E}_{\rm damp} \sim \frac{\omega_{\rm A}^2}{\Omega} |B_\phi|^2 \,, \tag{3.7}$$

where $\dot{E}_{\rm damp}$ is the non-linear energy dissipation rate. The growth of the B_ϕ field saturates when the generation of the field due to the instability ($\gamma_{\rm amp} \sim q\Omega\omega_A/N$) is balanced by the diffusion of the field through turbulent cascade ($\gamma_{\rm turb}$). Equating this two expressions one obtains the saturation expression for ω_A. From the definition of the Alfvèn frequency, the B_ϕ strength at saturation can be calculated. The B_r saturation value is obtain using the following relation

$$\frac{B_r}{B_\phi} \sim \frac{\omega_A}{N} \,, \tag{3.8}$$

that derives from the incompressible nature of the instability $B_r/l_r \sim B_\phi/l_\perp$. Combining the magnetic field strengths, the magnetic torque ($B_r B_\phi$) transporting angular momentum is produced via Maxwell stresses due to the dynamo field generated, and can be written in terms of the following diffusivity ($\nu = B_r B_\phi / 4\pi\rho q\Omega$)

$$\nu_{\rm TS} \sim r^2 \Omega q^2 \left(\frac{\Omega}{N}\right)^4 \,. \tag{3.9}$$

This equation applies in the case when thermal diffusion is unimportant, thus the composition gradient dominates the effects of thermal stratification (see Spruit 2002 for details when accounting for thermal diffusion). The minimal shear in order for the instability to operate can be obtained combining the instability criterion (equation 3.4) with the ω_A in the saturated state,

$$q_{\rm min,TS} \sim \left(\frac{\Omega}{N}\right)^{7/4} \left(\frac{\eta}{r^2 N}\right)^{1/4} . \tag{3.10}$$

The small fluid displacement in the radial direction due to the saturation of the Tayler instability is usually orders of magnitude lower than the horizontal displacements, hence a possible generated chemical mixing will be less efficient than the transport of angular momentum. Nonetheless, the diffusivity of mixing of chemical elements can be written as,

$$D_{\rm TS} \sim r^2 \Omega q^4 \left(\frac{\Omega}{N_\mu}\right)^6 . \tag{3.11}$$

There are two particular aspects of this theory that have been criticized. Zahn et al. (2007) outlined that since the instability generates a non-axisymmetric B_r field (as m=1 modes dominate in the Tayler instability), the winding of this field does not necessarily reproduce an axisymmetric B_ϕ field (but mostly a non-axisymmetric component). So the axisymmetric component of the fields B_r and B_ϕ are not necessarily related by (3.8) as initially suggested by Spruit (2002). The second problem (raised by Fuller et al. (2019)) is that equation 3.6 possibly overestimates the damping rate for the large-scale components of B_ϕ, hence, the saturated B_ϕ and B_r fields can reach higher values. Recently, Cantiello et al. (2014) also demonstrated that this mechanism cannot explain the slowing down of the core rotation of red giants as shown in figure 3.1.

3.3.2 Fuller-formalism

To overcome the difficulties of this theory, Fuller et al. (2019) proposed that the Tayler instability transfers energy from the background magnetic field B_ϕ (axisymmetric) to a perturbed field $\delta B_\perp$ (non-axisymmetric). Instead of the background field as in Spruit (2002), it is the energy of $\delta B_\perp$ that is damped to small scales with a turbulent damping rate γ_{cas},

$$\gamma_{\rm cas} \sim \frac{\delta \nu_{\rm A}}{r} , \tag{3.12}$$

where $\delta \boldsymbol{\nu}_{\rm A} = \delta \boldsymbol{B}/\sqrt{4\pi\rho}$ is the perturbed Alfvèn velocity. Hence, the following damping rate is much smaller than equation 3.7,

$$\dot{E}_{\rm damp} \sim \frac{\omega_{\rm A}^4}{\Omega^3} |B_\phi|^2 . \tag{3.13}$$

The magnetic field thus reaches higher values in the saturated regime, and the associated effective angular momentum diffusivity writes as follows

$$\nu_{\rm F} = \alpha^3 r^2 \Omega \left(\frac{\Omega}{N_{\rm eff}}\right)^2 , \tag{3.14}$$

where α is a dimensionless parameter, and $N_{\rm eff}$ is the effective Brunt-Väisälä frequency given by $N^2_{\rm eff} = \frac{\eta}{K} N^2_T + N^2_\mu$, with η and K the magnetic and thermal diffusivities, N_T and N_μ the thermal and chemical composition components. In Fuller et al. (2019) $\alpha \approx 1$ was found to fit the observational data.

The minimal shear for the Tayler instability to set in, analogous of equation 3.10, for the Fuller prescription also highly depends on this free parameter and can be written as

$$q_{\rm min,F} = \alpha^{-3} \left(\frac{N_{\rm eff}}{\Omega} \right)^{5/2} \left(\frac{\eta}{r^2 \Omega} \right)^{3/4} . \tag{3.15}$$

The coefficient for the induced chemical mixing associated with this formalism writes as follows

$$D_{\rm F} = \alpha^3 r^2 \Omega \left(\frac{\Omega}{N_{\rm eff}} \right)^2 \left(\frac{q\Omega}{N_{\rm eff}} \right)^{5/3} . \tag{3.16}$$

The authors highlighted some potential problems with this formalism. The models seem to converge to the same rotation rate independent of the initial rotations. Also, a very weak magnetic fossil field is needed for this mechanism to be the dominant source of transport of angular momentum.

Eggenberger et al. (2019) has tested that the Fuller-formalism is in fact dominant over meridional and shear instabilities. However, further studies on the α parameter to model subgiants and red giants showed a departure from the value in the original article ($\alpha = 1$). Eggenberger et al. (2019) found that $\alpha = 0.5$ was needed to match the measured frequency splittings for subgiants, but did not match the frequency splittings for red giants, that require $\alpha = 1.5$. They also found a lower degree of radial differential rotation in their models in opposition to observed values. den Hartogh et al. (2020) studied the limits for α in red clumps and white dwarfs. For red clump stars, α between 2 and 4 was required to match the observations. For white dwarfs the Fuller-formalism could not match the core rotation rates, unless when it was excluded at the end of the core He-burning phase.

Chapter 4

KIC 8579095: Stellar models with transport of angular momentum

This chapter describes the computational models and methodology used throughout this work. To compute stellar evolutionary models we made use of the open-source 1D stellar evolution package, Modules for Experiments in Stellar Astrophysics (MESA). This code is widely used in the astrophysics community, as it is undergoing active development and contains a wide variety of input stellar parameters to model different physics in stellar interiors. We also made use of the robust open source pulsation code GYRE for the purpose of computing oscillation frequencies and the respective eigenfunctions. GYRE has the advantage to compute solutions for the stellar oscillation equations in both adiabatic and non adiabatic regimes and the possibility to include first and higher approximations in the implementation of rotation, which we took advantage off in this work.

4.1 Process of star selection

For this particular study we considered targets from the APOKASC catalog (Pinsonneault et al. 2018) that combined general spectroscopic quantities with crucial seismic quantities to model the evolution of a star. The targets in the APOKASC catalogue contain high-resolution H-band spectra from the APOGEE project (Majewski et al. 2017), analyzed during the 14th data release (DR14) of the Sloan Digital Sky Survey (Abolfathi et al. 2017). The asteroseismic data was obtained by the *Kepler* mission (Borucki et al. 2010) and analyzed by members of the *Kepler* Asteroseismology Science Consortium. This catalog provides the observational parameters $\{T_{\rm eff},\, \Delta\nu,\, \nu_{\rm max},\, [{\rm Fe/H}]\}$ (effective temperature, large frequency separation, frequency of maximum power, metallicity) as well asteroseismic quantities $\{\log g,\, M,\, R\}$ (log of asteroseismic surface gravity, mass, radius) estimated using the scaling relations (equations (2.38) and (2.39)) that are extremely useful to model the evolution of red giant stars.

In addition we made use of the $\{\Delta\Pi_1,\, \delta\nu_{\rm rot}\}$ (dipole mode period spacing, rotational splitting frequency) in Gehan et al. (2018), that were extracted from the mixed mode frequency spectra of a red giants sample.

We selected KIC 8579095 as our target star since it gathered all the information from both sources,

summarized in table 4.1. KIC 8579095 is also a confirmed rotating red giant branch star (not a fast rotator) with an estimated mass of ~ 1.366 $M_\odot$, which is in the mass range of previous studies of angular momentum transport in evolved stars (e.g., Cantiello et al. 2014; Eggenberger et al. 2019).

Quantities	Values	Sources
$T_{\rm eff}$ (K)	4773.6 $\pm$ 72.9	Abolfathi et al. 2017
[Fe/H]	0.352 $\pm$ 0.025	Abolfathi et al. 2017
$\log g$ (seis)	3.091 $\pm$ 0.005	Pinsonneault et al. 2018
M ($M_\odot$)	1.366 $\pm$ 0.039	Pinsonneault et al. 2018
R ($R_\odot$)	5.512 $\pm$ 0.014	Pinsonneault et al. 2018
$\nu_{\rm max}$ (μHz)	152.046 $\pm$ 0.009 152.46	Pinsonneault et al. 2018 Gehan et al. 2018
$\Delta\nu$ (μHz)	11.942 $\pm$ 0.004 12.0	Pinsonneault et al. 2018 Gehan et al. 2018
$\Delta\Pi_1$ (s)	77.9 $\pm$ 0.92 78.2	Vrard, M. et al. 2016 Gehan et al. 2018
$\delta\nu_{\rm rot}$ (nHz)	285.0 $\pm$ 1.46	Gehan et al. 2018

Table 4.1: Observed and estimated parameters of KIC 8579095. The illustrated columns correspond to: effective temperature, metallicity, log of asteroseismic surface gravity, mass, radius, frequency of maximum power, large frequency separation, dipole mode period spacing, rotational splitting frequency.

4.2 Stellar models and input physics

Stellar evolutionary tracks and structure models for a low mass star from the zero-age main sequence to the red giant branch were computed with the release version 12115 of MESA (Paxton et al. 2011, 2013, 2015, 2018, 2019). We used the same physical inputs as in the publicly available MESA inlist of Fuller et al. (2019) (except for the input parameters described in the calibration process below).

The physical inputs of our stellar evolution models follow the default MESA implementation. With the OPAL equation of state (Rogers and Nayfonov 2002) and OPAL opacities (Iglesias and Rogers 1996). Using the NACRE rate (Angulo et al. 1999) for the nuclear reaction rates and the Eddington grey atmosphere (Eddington 1926). Convection is treated according to the standard mixing-length theory as presented by Cox and Giuli (1968).

Besides the default MESA parameters, these models also include a predictive mixing scheme (Paxton et al. 2018), where the boundaries of a convection region expands until $\nabla_{\rm rad} = \nabla_{\rm ad}$ (equation 2.13) on the convective side, at each time step. Overshooting (controlled by the parameter $f_{\rm ov}$; Paxton et al. 2011, 2013) is implemented via a convective diffusion coefficient exponentially decaying beyond the boundary of convection regions: whether above convective cores or below convective envelopes. Mass loss (Paxton

et al. 2011) is taken into account following the implementations of Reimers (1975) for red giant stars and Blöcker (1995) for asymptotic giant branch stars.

Our MESA models incorporate rotation (Palacios 2013) and the effects of centrifugal force on the stellar structure by adopting the shellular approximation as described in chapter 2. The implementation of transport of angular momentum and mixing of chemical elements in radiative zones in MESA is described in detail in chapter 3. In convective regions the transport of angular momentum and mixing is accounted for using the MLT diffusion coefficient ($\alpha_{\rm MLT}$; Paxton et al. 2011) enforcing almost rigid rotation in those zones.

For all our models, initial solid body rotation with spin rate of ~ 3.6 days is set at zero-age main sequence. We evolve four MESA models until the red giant phase with different implementations of angular momentum transport and chemical mixing in radiative regions:

- the '**AM conservation**' model ensures total conservation of angular momentum (J) up to a 10^{-9} order between each step of evolution ($J_{\rm ini} - J/J < 10^{-9}$). This model does not include stellar wind (or major mass loss) and does not account for any angular momentum transport or mixing of chemical elements induced by rotation;

- the '**Hydrodynamic inst.**' model includes angular momentum transport and rotation-induced mixing ensured by a combination of several hydrodynamic instabilites (dynamical shear (DSI), Solberg-Hoiland (SH), secular shear (SSI), Goldreich-Schubert-Fricke (GSF) instabilities and Eddington-Sweet circulation (ES); described in great detail in Heger et al. 2000);

- the '**TS dynamo**' model includes dynamo-generated magnetic fields that transport angular momentum and mixing of chemical species in radiative zones, as proposed by Spruit (2002) (also known as Tayler-Spruit dynamo);

- the '**Fuller-form.**' model makes use of the revised prescription of the Tayler-Spruit dynamo for transport of angular momentum and mixing of chemical elements by Fuller et al. (2019) (known as Fuller-formalism). We computed a model with the free parameter of this prescription at the value of $\alpha = 1$ as suggested by the author and then with $\alpha = 1.65$ to reach the observed core rotation rate for this particular star.

4.2.1 Calibration process

To model KIC 8579095 we took advantage of the *astero* module (Paxton et al. 2013), and generated calibrated models from the zero age main-sequence to the current day (allowing a direct comparison with current observations) using the physical inputs described above.

The stellar model calibration process takes as inputs parameters $\{{\rm M_{ini}}, {\rm Y_{ini}}, {\rm [Fe/H]_{ini}}, \alpha_{\rm MLT}, f_{\rm ov}\}$ (stellar mass, initial helium abundance, initial metallicity, mixing-length parameter and overshooting parameter, respectively) and, throughout the stellar evolution, at each timestep, performs a comparison to the chosen observational and estimated constraints $\{{\rm T_{eff}}, \log g, \Delta\nu\}$, computing a χ^2_{star} value.

The helium mass fraction Y was computed assuming the linear relation with the metallicity, $Y(Z) = Y_0 + \Delta Y/\Delta Z \cdot Z$, with $Y_0 = 0.248$ and $\Delta Y/\Delta Z = 1.4$. The hydrogen mass fraction was computed using the relation $X = 1 - Y - Z$. [Fe/H] is calculated through $[\mathrm{Fe/H}] = \log[(Z/X)/(Z/X)_\odot]$ where $(Z/X)_\odot = 0.02293$ (computed by Bahcall et al. 2006).

The χ^2_{star} resulting from the calibration process determines whether the computed MESA evolution model can reproduce the outputs parameters within the observational uncertainties. In the case $\chi^2_{\mathrm{star}} \leq 1$ the final model parameters $\{\mathrm{T_{eff}},\ \log g,\ \Delta\nu\}$ are within the observational uncertainties. The χ^2_{star} value is calculated by weighting the contribution of spectroscopic χ^2_{spec} and seismic χ^2_{seis} observable according to $\chi^2_{\mathrm{star}} = 2/3\chi^2_{\mathrm{spec}} + 1/3\chi^2_{\mathrm{seis}}$ with

$$\chi^2_{\mathrm{spec/seis}} = \frac{1}{N}\sum_{i=1}^{N}\left(\frac{X_i^{\mathrm{mod}} - X_i^{\mathrm{obs}}}{\sigma_{X_i}}\right)^2 \tag{4.1}$$

where N is the number of parameters ($N = 2$ and $N = 1$ for χ^2_{spec} and χ^2_{seis}, respectively), X_i^{mod} and X_i^{obs} are the stellar model and observed values of the ith parameter, respectively, with σ_{X_i} being the observational uncertainty.

To determine the optimal set of input parameters (minimum χ^2_{star}) we used a common method (e.g., Capelo and Lopes 2020) where an optimization run is performed using the Nelder-Mead simplex algorithm (Nelder and Mead 1965) implemented in the *astero* module. For each MESA simulation, the *astero* module is called at each timestep to calculate the χ^2_{star} values from the current MESA model output parameters. This process is repeated multiple times with a different set of inputs until several models, with reasonable χ^2_{star} value, have been found. The output of this process is a table with χ^2_{star} and initial input parameters of the several red giant models. We selected the model with the minimal χ^2_{star} and use it as our benchmark model. Table 4.2 shows the benchmark model input parameters.

M_{ini} ($M_\odot$)	Y_{ini}	$[\mathrm{Fe/H}]_{\mathrm{ini}}$	α_{MLT}	f_{ov}
1.405	0.298	0.373	2.04	0.014

Table 4.2: Input parameters of the benchmark model. The illustrated columns correspond to: initial mass, initial helium abundance, initial metallicity, mixing-length parameter and overshooting parameter.

The benchmark model was computed using the Fuller-formalism prescription described above. The rest of the models with different mechanisms of transport of angular momentum and mixing – AM conservation, hydrodynamical instabilities and TS dynamo – were initialized with the same values of input parameters displayed in table 4.2.

Model	age (Gyr)	M ($M_\odot$)	R ($R_\odot$)	T_{eff} (K)	$\log g$	$\Omega_{surf}/2\pi$ (nHz)	$\Omega_{core}/2\pi$ (nHz)	$\Delta\nu$ (μHz)	$\Delta\Pi_1$ (s)	ν_{max} (μHz)	χ^2_{star}
AM conservation	4.57	1.405	5.640	4753.9	3.083	84	410,327	11.940	79.3	150.91	0.586
Hydrodynamic inst.	4.57	1.403	5.635	4753.8	3.083	84	402,812	11.948	79.4	150.98	1.117
TS dynamo	4.57	1.403	5.637	4753.5	3.083	85	21,824	11.942	79.4	150.88	0.482
Fuller-form. (α=1)	4.57	1.403	5.636	4753.6	3.083	85	1,076	11.943	79.4	150.90	0.496
Fuller-form. (α=1.65)	4.57	1.403	5.637	4753.6	3.083	85	674	11.942	79.4	150.89	0.478

Table 4.3: Properties of the KIC 8579095 converged RGB models without mixing of chemical elements. The 5 models were computed using the input parameters of table 4.2. The illustrated columns correspond to: age, mass, radius, effective temperature, logarithm of surface gravity, average surface rotation, average core rotation, large frequency separation for radial modes from scaling relations, dipole mode period spacing, frequency of maximum power from scaling relations.

Model	age (Gyr)	M ($M_\odot$)	R ($R_\odot$)	T_{eff} (K)	$\log g$	$\Omega_{surf}/2\pi$ (nHz)	$\Omega_{core}/2\pi$ (nHz)	$\Delta\nu$ (μHz)	$\Delta\Pi_1$ (s)	ν_{max} (μHz)	χ^2_{star}
Hydrodynamic inst.	4.60	1.403	5.608	4755.98	3.087	85	323,206	12.034	79.5	152.40	176.26
TS dynamo	4.58	1.403	5.633	4754.30	3.083	85	13,112	11.954	79.2	151.08	3.45
Fuller-form. (α=1.65)	4.58	1.403	5.636	4754.03	3.083	85	597	11.943	79.1	150.90	0.50

Table 4.4: Properties of the KIC 8579095 converged RGB models with rotation-induced mixing of chemical elements. The 3 models were computed using the input parameters of table 4.2. The illustrated columns are the same as table 4.3.

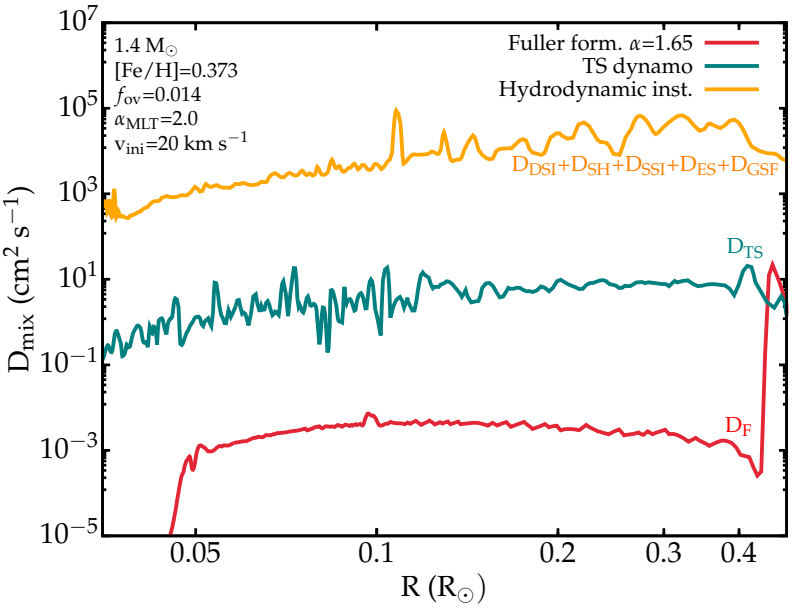

Figure 4.1: Diffusion coefficients for rotation-induced mixing below the convective zone for RGB models. The model in yellow was computed with angular momentum transport and rotation-induced mixing by a sum of hydrodynamical instabilities. In blue is the model computed using the Tayler-Spruit dynamo prescription. In red is the model obtained using the Fuller-formalism.

For the models besides the benchmark model we have not performed an optimization run to obtain their optimal input values. If we had initialized the four models with different input values, the converged final models would inherently differ due to those inputs, since any difference in the initial mass and metallicity would cause crucial changes in the evolution path and final state of the star. The different input parameters would not allow to isolate the visible differences in the stellar structure and evolution solely due to the mechanisms of transport of angular momentum which is one of our goals of study.

Table 4.3 summarizes the properties of the final converged models (without mixing of chemical elements) with the respective $\chi^2_{\rm star}$. We notice that the predictions of all these models are compatible with the stellar observational parameters shown in table 4.1.

4.2.2 Modeling rotation-induced mixing

Including rotation-induced mixing processes in stellar models is far from trivial. As described in chapter 3, MESA uses a diffusion approach where the diffusion coefficient in equation (3.2) is determined as the sum of individual mixing processes. This gives rise to discontinuities along the radius of the models as seen in figure 4.1, particularly in the model accounting for hydrodynamic instabilities since there is a sum of five different coefficients. On one hand, to overcome this problem some degree of spatial smoothing is applied to the models. On the other hand, a new problem arises, namely the effects of the mixing processes on the chemical composition and internal structure are enhanced. This MESA feature is in ongoing development so the results have to be interpreted with caution.

On that note, we accounted for rotation-induced mixing and implemented a minimal smoothing on three of the models described in the previous section: hydrodynamical instabilities model; TS dynamo model; Fuller-formalism model. The rotation-induced mixing coefficient of the Fuller-formalism is being implemented in a computational model for the first time in our work.

The models with mixing converge with χ^2 values much higher than one 1 (see table 4.4). This is a result of initializing this models with the same input parameters as the models without mixing (which we decide to maintain the consistency between models). The results in tables 4.3 and 4.4 clearly show the important impact of diffusion in the asteroseismic background structure.

4.3 Computation of stellar oscillations

To fully understand the repercussions of the different mechanisms of transport of angular momentum and mixing in the stellar interior we need to investigate the oscillation frequencies and respective eigenfunctions in the crucial regions of the previous obtained MESA stellar models. According to the observed frequency of maximum power and large frequency separation for KIC 8579095 (table 4.1), we selected the frequency window $(\nu_{\rm max} \pm 4\Delta\nu) \sim [100; 200]\ \mu Hz$ to compute the oscillation frequencies.

The oscillation modes and corresponding rotational kernels were obtained using GYRE (Townsend and

Teitler 2013; Townsend et al. 2017) given the MESA input stellar models described above (TS dynamo and Fuller-formalism). GYRE was used to compute the oscillation frequencies by solving the fourth-order system of adiabatic equations (e.g., Aerts 2021), given by equations (2.30)-(2.32), rather than relying on the Cowling approximation.

Differential rotation is implemented according to the Ω distribution of the equilibrium stellar model (assuming shellular rotation). We took advantage of the lowest-order rotation effects in the oscillations equations included in GYRE (does not account for the Coriolis effects). The rotational splittings for all the modes in our frequency window were obtained according to equation (2.46).

Table 4.5 shows the estimated core rotational splittings obtained using $\delta\nu_{\rm rot} = \max(\delta\nu_{\rm rot,n,l=1})$ (Mosser et al. 2012). In other words, we selected the mode with higher $E_{\rm norm}$ and retrieve the respective rotational splitting, that should in theory correspond to the core rotation rate.

Model	$\Delta\nu$ (μHz)	$\Delta\Pi_1$ (s)	$\delta\nu_{\rm rot}$ (nHz)	$\sigma_{\delta\nu_{\rm rot}}$
Fuller-form.	78.88	12.62	291.91	5
Fuller-form. with mix	78.60	12.62	252.10	23
TS dynamo	78.88	12.62	8982.48	5957
TS dynamo with mix	78.71	12.63	5090.96	3292

Table 4.5: Large separation in frequency and separation in period for dipole modes obtained using asymptotic expressions (equations (2.40) and (2.42)), and rotational splittings plus the respective relative errors. This values were computed using GYRE for the TS dynamo and Fuller-formalism, with and without rotation-induced mixing.

Chapter 5

KIC 8579095: Impact of rotation in stellar models with transport of angular momentum

In this chapter we discuss how different angular momentum transport mechanisms impact the evolution and structure of a red giant model. We also implement mixing induced by these angular momentum mechanisms to visualize the evolution of the abundance profiles of various chemical elements. At last, we obtain the frequency modes for the Tayler-Spruit dynamo and Fuller-formalism with and without mixing to understand their important on the mode propagation in the various regions inside the star.

5.1 Angular momentum transport

A description of the models and its input parameters used in this section is written in detail in chapter 4. We successfully modeled the stellar evolution of the star KIC8579095, reaching the values for measured and estimated quantities $T_{\rm eff}$, $\log g$, $\Delta\nu$ in table 4.1, and matching the core rotation rate of the red giant model to the asteroseismic derived rotational splitting by adjusting the α parameter of the Fuller-formalism.

The models with different mechanisms of transport of angular momentum (figure 5.1 filled lines) barely show any deviations from the point of view of the surface stellar variables (e.g., luminosity, effective temperature, surface gravity) – less than 0.05% deviation – and also from the asteroseismic diagnostic variables (e.g., large frequency separation, dipole modes period spacing) – less than 0.1% deviation. In fact, the helium core mass and radius are one of the variables more influenced by the different mechanisms, with a relative deviation around 0.1% and 0.04%, respectively. Overall, the major impact of these mechanisms rely on the evolution of the core rotation rates and they solely differ in the efficiency of transport of angular momentum from the inner to outer regions of the star. In the subgiant phase the envelope suffers an expansion while the inert helium core contracts. This is where the mechanisms diverge and predict different core spin rates. On the other hand, the surface rotation behavior is similar for all models, and evolves as rigid rotation throughout all stages of evolution.

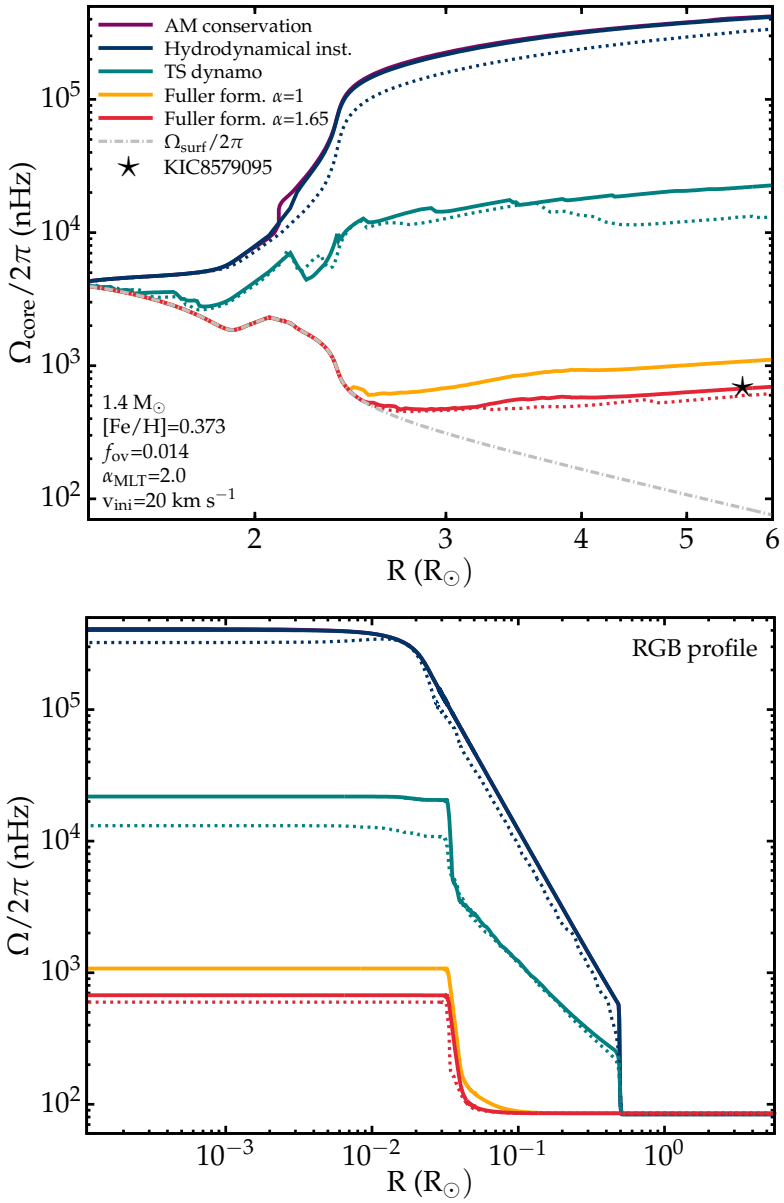

Figure 5.1: Evolution of core rotation rates as a function of radius from the ZAMS to below the RGB bump (left panel). Rotation profile for calibrated RGB models (right panel). The full (dotted) lines indicate the models without (with) mixing of chemical elements induced by rotation. Models accounting for conservation of local angular momentum (purple), including transport of angular momentum due to hydrodynamic instabilities (blue), and to magnetic torques in radiative regions, with the Tayler-Spruit dynamo (green) and with the Fuller-formalism: $\alpha = 1$ (yellow) and $\alpha = 1.65$ (red). The star symbol represents the location of KIC8579095. The grey dashed and dotted line corresponds to the surface rotation rate of all the models.

The top panel of figure 5.1 illustrates the core rotation rate evolution with the stellar radius of an approximately 1.4 $M_\odot$ red giant model with different prescriptions of transport of angular momentum in the inner radiative region.

The model accounting for conservation of angular momentum (purple) predicts the highest core rotation rates at all times, and a core spin up of more than 2 orders of magnitude higher than observed values for this red giant. This model has no substantial mass loss star, thus in the main-sequence phase the model does not lose mass and already spins faster comparing to the other models. In the subgiant phase, due to the local conservation of angular momentum, the core contracts and spins up drastically while the surface expands and consequently spins down to very low values. Along the red giant branch, the core continues to spin up but at a lower rate, and the surface continually spins down.

The inclusion of transport of angular momentum through hydrodynamical instabilities (blue) also leads to higher core rotation rates in the red giant phase than current measurements. In fact this model predicts almost the same rotation rate as the model with conservation of angular momentum, which reveals how non efficient this mechanisms are in this mass range.

The Tayler-Spruit dynamo model (green) provides a lower core spin up at the subgiant phase than the model considering local conservation of angular momentum or even the model with hydrodynamic instabilities (same results in Cantiello et al. 2014). However the core rotation rate is still one order of magnitude higher than asteroseismic values. The low efficiency of transport comes from the suppression of angular momentum mixing in red giant due to the steep composition gradient. Cantiello et al. (2014) increased the coefficient of diffusion by a factor of 100 however that still did not lower the rotation rate to match observed values.

After the initial spin up in the subgiant phase, the efficiency of transport of angular momentum in the Fuller-formalism (Fuller et al. 2019) model (red) matches the observed core rotation in the red giant. Figure 5.1 shows 2 models with a different value for the free parameter α of this mechanism. The original paper suggests $\alpha \approx 1$ as a reasonable saturation parameter that leads to good agreement with asteroseismic core measurements. In our models, a higher value of $\alpha = 1.65$ was needed to meet the core rotation rate of KIC8579095. This parameter enters in the calculation of the viscosity coefficient and in the instability condition and we discuss its implications in the next chapter 6.

The bottom panel of figure 5.1 illustrates the rotation profile of the calibrated red giant models, for the four mechanisms of transport of angular momentum. All models predict almost rigid rotation in the helium core. The decay of rotation in transition zone between radiative and convective layers, with H-burning in the shell surrounding the core, diverges between models. The conservation of angular momentum, hydrodynamical instabilities and the TS dynamo models decay exponentially (as can be seen in figure 5.1). Whereas the Fuller-formalism decays with a $\tanh(r)$ function (as implemented in the code from Fuller et al. 2019). In the convective zones, all the models show almost uniform rotation.

5.2 Rotation-induced chemical mixing

Rotation-driven transport processes have to be taken into account to explain the discrepancies between abundance observations and stellar evolution models predictions. This mechanisms are only dominant in some cases, thorough calculations must be performed incorporating chemical transport via other equally relevant sources such meridional circulation, convective overshoot, thermohaline mixing and others, however, this is out of the scope of this thesis.

In this section we included rotation-induced mixing processes (figure 5.1 dashed lines) in three of the models of the previous section: hydrodynamic instibilities, Tayler-Spruit dynamo and Fuller-formalism; to understand their role on the evolution of chemical abundances in a particular red giant model and test if they can in fact explain some of the current discrepancies between numerical models and observations. The models obtained in this section are described in detail in chapter 4, and are initialized with the same input physics as the models in the previous section with the addition of rotation-induced mixing.

In figure 4.1 of the previous chapter we sought that the mixing diffusion coefficient for the model including hydrodynamical instabilities surpasses by 4 and 6 orders of magnitude the coefficient for mixing induced by the Tayler-Spruit dynamo and Fuller-formalism, respectively. Hence, we expect higher mixing of chemical elements in between radiative and convective regions (the so-called tachocline region) from that first model.

The expression derived by Fuller et al. (2019) for the mixing of chemical elements (equation (3.16)) predicts very lower values ($\nu_{\rm mix}/\nu_{\rm AM} \sim 10^{-6}$). Models with the Fuller-formalism exhibit slower core rotation and smaller shears, which translates into a non efficient mixing of chemical elements in stellar interiors.

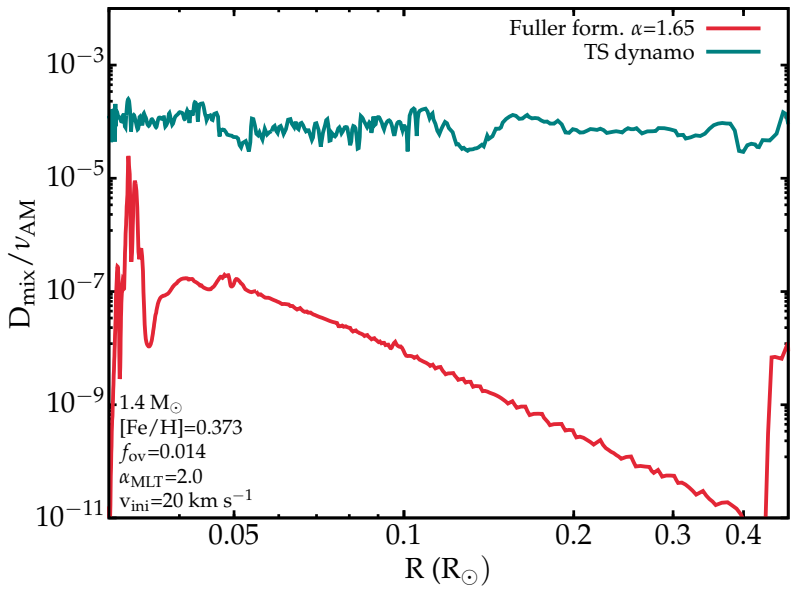

Figure 5.2: Ratio between the diffusion coefficients for rotation-induced mixing ($D_{\rm mix}$) and angular momentum transport ($\nu_{\rm AM}$). In blue is the model computed using the Tayler-Spruit dynamo prescription. In red is the model obtained using the Fuller-formalism.

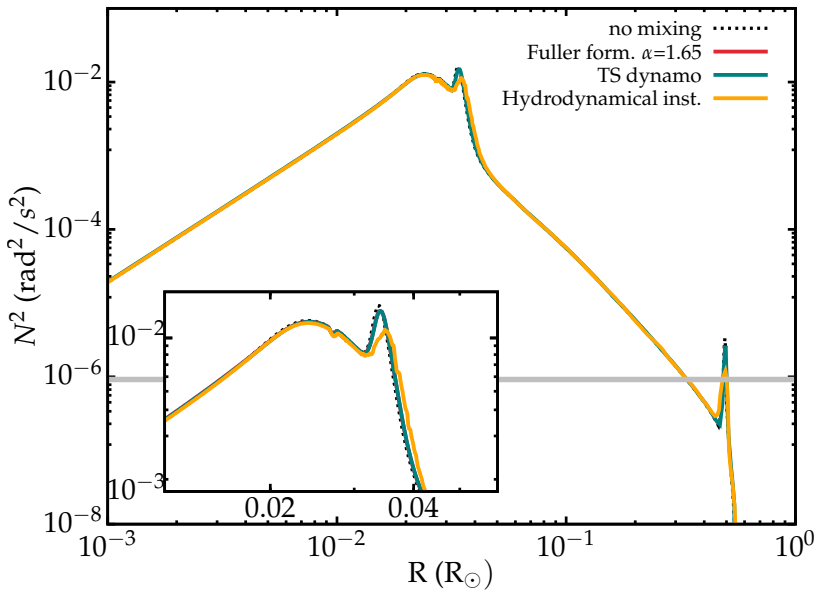

Figure 5.3: Brunt-Väisälä frequency as a function of radius for the RGB models with mixing induced by the hydrodynamic instabilities (yellow), by the Tayler-Spruit dynamo mechanism (green) and by the Fuller-formalism (red). The model without mixing is illustrated with a black dashed line. The horizontal grey line indicates the measured frequency of maximum oscillation power $\nu_{\max}$ of KIC8579095.

Since this hypothesis was not previously tested in computational models, we include this expression in our models to test the statements of the original paper. We observed that $\nu_{\rm mix}/\nu_{\rm AM}$ varies from 10^{-13} to 10^{-5} in the regions where the instability is triggered (see figure 5.2). Hence in our models, the Fuller-formalism manifests slightly higher mixing than what was initially theorized, nonetheless still very low values and non significant. However, the resolution of this processes in numerical evolution codes needs to be improved in order to derive further conclusions.

The repercussions in the internal properties of the star due to rotation-induced mixing are more visible in the asteroseismic variables (e.g., large frequency separation and mixed mode period spacing; see tables 4.3 and 4.4). There are small but visible changes in the density and abundance profile of the red giant models due to the mixing processes (see figure 5.4). In figure 5.1 we can identify that models including rotation-induced mixing predict slightly lower rotation rates. The induced mixing seems to act as an additional angular momentum diffusion coefficient increasing its transport efficiency.

The Brunt-Väisälä frequency (figure 5.3) is also affected due to the change in compositional gradient in the inner layers (below the convective envelope). The highlighted spike around 0.04 R$_\odot$ that results from a variation in the chemical composition at the H-shell burning displays some disparity between different mixing processes. Nonetheless, this spike is far from the observational window centered around the frequency of maximum oscillation power, so it will unlikely contribute to constraint the mixing coefficients. The second spike around 0.5 R$_\odot$ results from chemical discontinuities left behind by the receding convective envelope. This is the signature of the first dredge up that occurs when a low mass star enters the red giant phase,

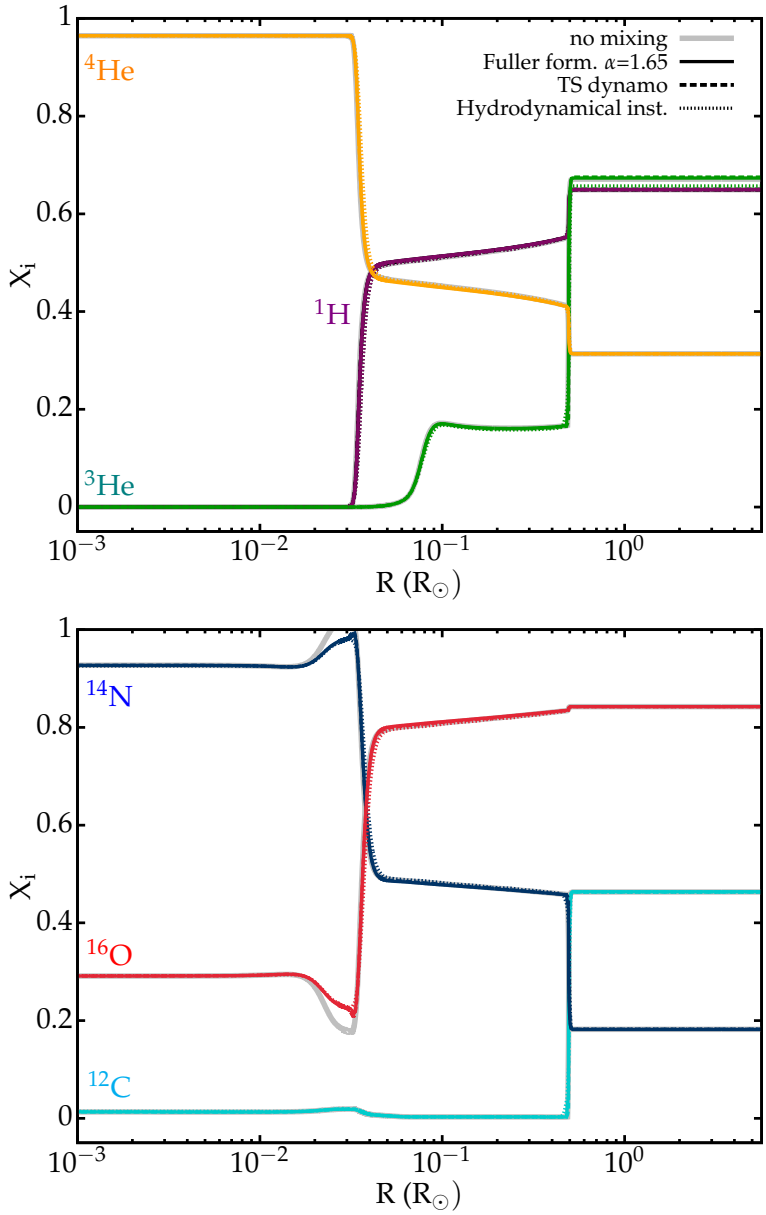

Figure 5.4: Evolution of mass fractions of several chemical species with radius for the red giant KIC8579095. In the top panel the mass fractions are ^{1}H (purple), ^{4}He (yellow) and multiplied by 1000 ^{3}He (green). In the bottom panel the mass fractions are multiplied by 50 for ^{12}C (green), ^{14}N (blue) and multiplied by 100 for ^{16}O (red). The models without mixing induced by rotation are grey and the models with mixing induced by the hydrodynamic instabilities are the dotted dashed lines, by the Tayler-Spruit dynamo mechanism the dashed lines and by the Fuller-formalism the full lines.

where the convective envelope extends up to the nuclear reactions region. There are slight visible differences between mixing mechanisms in that spike, although still not significant. Nonetheless, in more extreme cases (e.g., more efficient mixing mechanisms), this sharp features may affect g-dominated modes (through buoyancy glitches Cunha et al. 2015) and hence become mensurable.

The mass fractions of ^{1}H, ^{3}He, ^{4}He, ^{12}C, ^{14}N and ^{16}O profiles for the calibrated red giant models are illustrated in figure 5.4. The main variation takes place in the tachocline region as expected. Models with mixing induced by hydrodynamic instabilities show a less steeper slope (very small difference) than the other models in this transition region. Hence, rotation-induced mixing seems to smooth the abundance profile in the interior (also observed in Charbonnel and Lagarde 2010). Our models do not predict significant modifications in the surface abundances, which can potentially come from the weak mixing power of this rotation-induced mechanisms as discussed in chapter 3. However this is an important tracer in order to compare this models with current spectroscopic abundance measurements (Somers and Pinsonneault 2016).

Both the mixing of chemical elements by the Tayler-Spruit prescription and by the Fuller-formalism show a small effect in figure 5.3 and 5.4 (as expected by Maeder and Meynet 2004 for the case of TS dynamo). The mixing due to hydrodynamic instabilities has the higher impact as expected.

5.3 Asteroseismic diagnosis

In this section we compute important asteroseismic variables that can be used to extend our knowledge in stellar interiors. Particularly, the observation of dipole modes in red giant stars reveal a mixed mode pattern which is extremely useful to use as a complementary tool to probe the core structure and chemical properties. In this section, stellar oscillations for theoretical models were computed using GYRE (see chapter 4 for details).

Period spacing

The left panels of figure 5.5 illustrate the period spacing for modes with $l = 1$ for the models with transport of angular momentum/mixing mechanism by the Fuller-formalism with $\alpha = 1.65$ (top) and by the Tayler-Spruit dynamo (bottom).

The pattern of period spacing in figure 5.5 shows mixed modes, predominantly of g-mode character. The several local minima and maxima of the period spacing, suggests that the modes in between those regions are being subject to trapping. At high frequency (low period), the period spacing shows a characteristic decrease as more local minima appear in the pattern due to an increase in p-dominated modes. At relatively low frequency (high period), the frequency spacing becomes nearly constant in agreement with the asymptotic period spacing (equation (2.42); horizontal grey dashed line). Therefore, observations of low frequency g-dominated modes provide constraints to the integral of the Brunt-Väisälä frequency in the stellar cores (Hekker and Christensen-Dalsgaard 2017).

The chemical discontinuities previously described in the Brunt-Väisälä frequency, can also be observed through sharp features (also called glitches) in the oscillation spectrum and in the mixed mode period spacing, and cause oscillatory variations in the frequencies that can be modeled (Cunha et al. 2015). We do not observe glitches in the models with mixing which is another possible indication that the impact of this rotation-induced mixing processes is not enough to leave a detectable imprint on oscillation frequencies.

Mode inertia

The right panels of figure 5.5 illustrate the normalized inertia for $l = 1$ modes Fuller formalism (top) and the TS-dynamo (bottom) models. The mixed mode pattern is very defined by the large contrast between the deep local minima and maxima.

The values of $E_{\rm norm}$ are much larger for g-dominated modes – about one order of magnitude – than for p-dominated modes. This reflects the higher contribution to the mixed mode that g-dominates modes have in the core, since they present larger amplitudes in the inner radiative cavity than p-dominated modes. The models with rotation-induced mixing of chemical elements show slight lower $E_{\rm norm}$ in comparison with models without mixing, but this effect is fairly negligible.

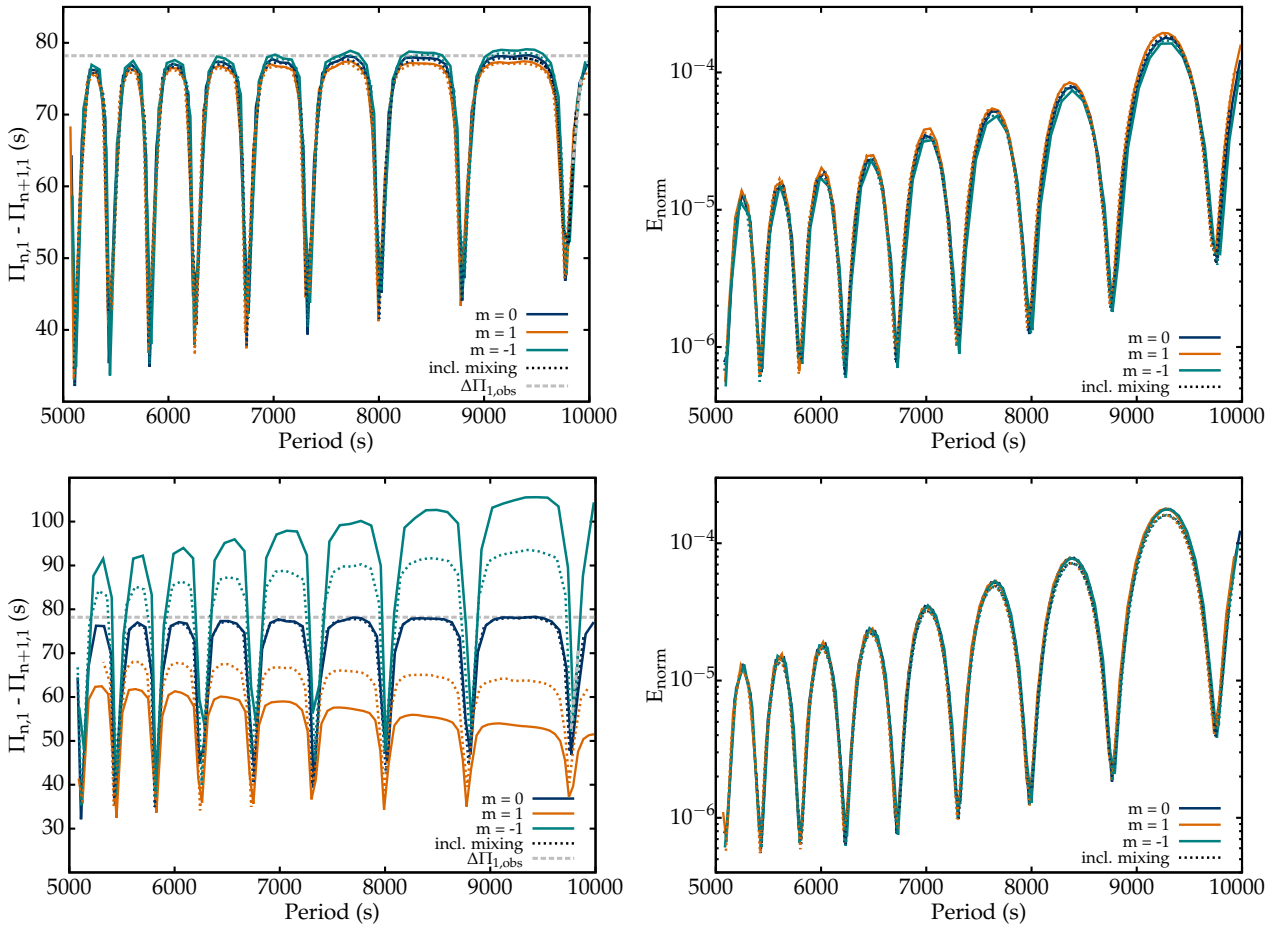

Figure 5.5: Period spacing of dipole modes as a function of the mode period, for models including the Fuller-formalism (top left) and the TS dynamo (bottom left). Normalized inertia for dipole modes as a function of period, for models including the Fuller-formalism (top right) and the TS dynamo (bottom right). The grey dashed line represents the estimated dipole mode period spacing $\Delta\Pi_1 = 78.2$ s from Gehan et al. (Gehan et al. 2018).

Rotational splittings

In figure 5.5 (left bottom) it is evident the drastic impact of rotation in the oscillation frequencies. Rotational splittings of g-dominated modes are a great tool to probe the rotation of the central region. The rotational splittings are computed with GYRE using equation (2.46), hence, the splitting of modes follows the almost same behavior as the value of $E_{\rm norm}$. Rotation causes a slope on the period spacing pattern in the low frequency g-dominated modes, and higher rotations lead to steeper slopes. The splitting of oscillation frequencies increases with the higher rotation rates, hence models with TS dynamo mechanism predict higher splittings. On the other hand, in the previous section we observed that including rotation-induced chemical mixing slightly decreases the core rotation rate, and as we can see in figure 5.5, this reflects on a slightly lower frequency splitting.

Radial and horizontal displacement

Figure 5.6 presents two of the scale eigenfunction displacements calculated in this work. The full compilation of figures can be found in appendix B. We want to find a correlation between the amplitudes of the eigenfunctions in stellar interiors and the differences observed in figures 5.5 when implementing the various models with/without rotation-induced mixing.

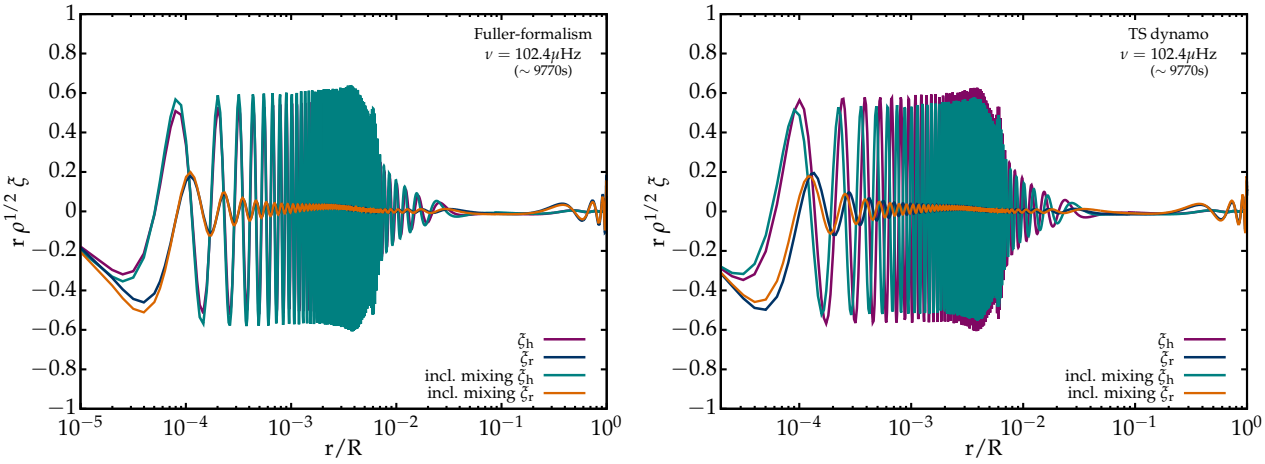

Figure 5.6: Scaled radial and horizontal displacement (on arbitrary scale) for modes with l=1 and m=-1, ν = 102.4 μHz. Models with the Fuller-formalism on the left and with Tayler-Spruit dynamo on the right, both computed with and without rotation-induced mixing for comparison purposes. For reference, the selected mode corresponds to the local minimum around 9770s in figure 5.5.

The general behavior in the figures of appendix B reveals that more visible differences between models with and without rotation-induced mixing arise in modes with lower inertia (correspond to local minimum in figure 5.5). This modes are less g-dominated and more p-dominated, as can be seen by the lower amplitude in the deepest zone ($\sim$ 0.6) and the higher amplitude closer to the surface in figure 5.6 in comparison to modes with higher inertia.

The horizontal eigenfunction amplitudes near the deepest zone $r/R < 10^{-2}$ for models with mixing of chemical elements due to rotational transport are slightly lower than without mixing. Closer to the surface, this differences dissipates. For the models computed using the Tayler-Spruit dynamo the variations are more visible than models with the Fuller-formalism, as expected, in particular in modes with m=1 or m=-1, since one can identify a small shift in the eigenfunctions when including rotation-induced mixing.

Overall the variations are of very lower amplitudes hence they unlikely will be mensurable. Nonetheless, the potential of asteroseismic diagnostic tools to probe the mixing in stellar interiors should not be dismissed and instead explored with other more efficient mixing processes.

Chapter 6

Asteroseismic constraints on angular momentum transport models

This chapter is devoted to the subject of evolution of rotation rates from the main-sequence to the red clump stage (RC; stars that are currently fusing helium in their cores). We start by reviewing the current status of asteroseismic rotation data along stellar evolution. Next, we discuss the impact of the initial parameters: stellar mass, metallicity, convective overshooting and α parameter from the Fuller-formalism when modeling rotation. Lastly, we compute the initial rotation period and the free parameter α using the Fuller-formalism in order to reproduce the observed surface and core rotation rates obtained through asteroseismic inversions.

6.1 Asteroseismic constraints on rotation rates along stellar evolution

The rotation profile evolves as the star moves along the HR-diagram. Asteroseismology is a great tool to constraint the core and surface/envelope rotation rates of stars from the main-sequence to the white dwarf phase.

However, asteroseismic rotation splittings of main-sequence solar-like stars cannot probe core rotation rates $\Omega_{\rm core}$, only envelope rotation rates $\Omega_{\rm env}$ (near surface layers). Nonetheless, asteroseismic rotation rates in combination with surface rotation rates, $\Omega_{\rm surf}$ obtained using high-precision spectroscopic measurements of $v \sin i$, revealed that intermediate mass main-sequence stars envelopes rotate nearly uniformly (Aerts et al. 2019). Observational data shows two distinct rotational regimes on the main-sequence stage (Kraft 1967). Stars with masses greater than 1.2 $M_\odot$ that do not spin down during the main-sequence and remain fast rotators. Stars with masses lower than 1.2 $M_\odot$ that spin down presumably due to magnetic braking during the main-sequence, thus are generally slow rotators. After the main-sequence, there is a general decrease in the surface rotation rate with age for both mass ranges.

On the subgiant branch, as the core contracts, the inner and outer regions evolve with different rotation. The core spins up while the envelope spins down as it expands (Marques et al. 2013). The number of mixed modes at the beginning of the subgiant branch is small, however, it increases as the star evolves towards

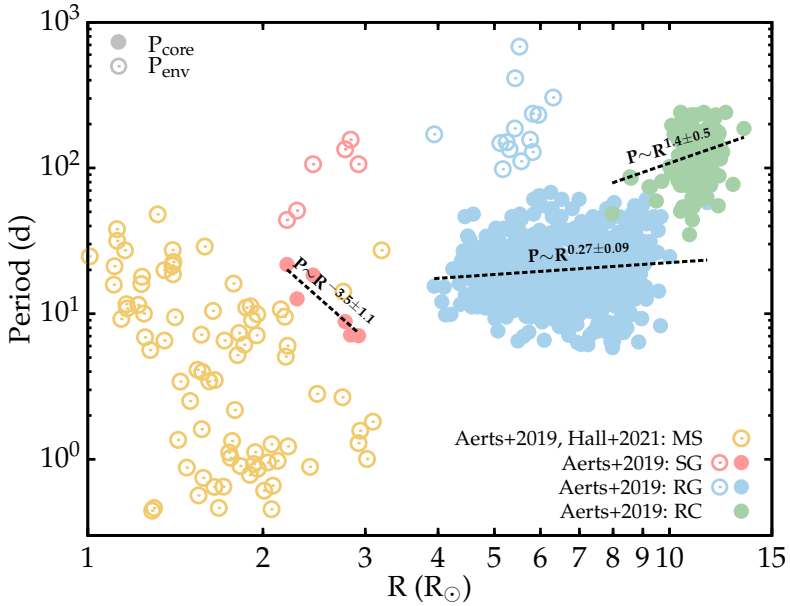

Figure 6.1: Core (filled circles) and envelope/surface (empty circles) rotation period as a function of the stellar radius for 1,093 stars with masses between 1-2 $M_\odot$. The asteroseismic estimates of core and surface rotation and respective radius of 34 main-sequence (yellow), 6 subgiants (red), 843 red giants (blue) and 164 red clump (green) stars were obtained from Aerts et al. (2019). The 46 remaining main-sequence (yellow) stars were taken from Hall et al. (2021) and the respective radius from Aguirre et al. (2017). The dashed black lines indicate the fit performed to subgiant, red giant and red clump core rotation period.

the red giant branch. Nonetheless the core and envelope rotation of subgiant stars are currently precisely determined from asteroseismic measurements (Deheuvels et al. 2014).

As stars evolve up in the red giant branch, the number of g-dominated modes increases in comparison with the existing mixed modes (Dupret et al. 2009) hence measurements of these modes essentially probe the core rotation (Beck et al. 2012) and reveal a strong differential rotation profile (Marques et al. 2013). This implies that there must be an efficient angular momentum transport mechanism in the inner regions of subgiant and red giant stars.

Asteroseismic estimates of red clump stars show they are rotating (Mosser et al. 2012) six times slower than red giant cores. This can be somewhat explained by the change in core radius during He-burning, but not entirely, suggesting a strong transfer of angular momentum from the inner to outer regions.

Figure 6.1 shows the core and envelope or surface rotation period as a function of the stellar radius from a sample of 1,093 stars that were monitored during *Kepler* mission, obtained from combination of the data in Aerts et al. (2019) and in Hall et al. (2021). The sample varies from main-sequence up to red clump stars, with stellar masses between 1-2 $M_\odot$ and stellar radius between 1-15 $R_\odot$. Asteroseismic masses and radii were deduced from scaling relations (defined in equations (2.38) and (2.39)) of damped p-modes or from forward modeling of g-modes obtained by Aguirre et al. (2017), with precisions of $\sim$4% and $\sim$2%, respectively. The rotation rates vary from 0 up to 80% of the critical velocity, with precisons from 0.1-5% (Aerts et al. 2019), hence their errors are smaller than the symbol size in figure 6.1. We also excluded from

the initial sample stars in binaries systems.

To estimate how the core rotation period varies with the stellar radius along the subgiant, red giant and red clump stage we performed a linear fit to logarithm of the data from figure 6.1 to obtain the power laws below and compare them with the values in Mosser et al. (2012). Taking into consideration our broader mass range [1,2 $M_{\odot}$], we obtained the following values:

$$P_{\mathrm{core,SGB}} \propto R^{-3.5\pm1.1} \qquad P_{\mathrm{core,RGB}} \propto R^{0.27\pm0.09} \qquad P_{\mathrm{core,RC}} \propto R^{1.4\pm0.5} \tag{6.1}$$

We found no correlation between the core rotation periods and the stellar mass of the stars in the subgiant, red giant and in the red clump phase.

During core H-burning, the radius of main-sequence stars does not increase significantly, hence the rotation period does not depend strongly on the radius as we can see from the data in figure 6.1. On the subgiant branch, we observe that the period decreases with increasing radius, in opposition to van Saders and Pinsonneault (2013) results. However, the number of subgiant stars in figure 6.1 is not enough to take plausible conclusions. From the red giant power law, we found that red giants period slightly increases with radius. We estimate a less steeper slope than found by Mosser et al. (2012) ($P_{\mathrm{RGB}} \sim R^{0.7\pm0.3}$), that can possibility be justified by our broader mass range [1,2 $M_{\odot}$]. Red clump stars spin down faster as they evolve. The slope found for red clump stars agrees with the Mosser et al. (2012).

6.2 Impact of input parameters in rotation

To investigate the dependence on the input physics of stellar models on the evolution from the main-sequence to above the red giant bump, when including the Fuller-formalism (Fuller et al. 2019), several models were generated with different initial stellar masses, metallicities, convective overshooting and α parameters.

The benchmark model (purple) was computed with an initial stellar mass of 1.5 $M_{\odot}$, Z$= 0.02$, $f_{\rm ov} = 0.015$ and $\alpha_{\rm mlt} = 2$ with an initial period of 2 days and $\alpha = 1$. This mass is commonly used for studying rotation on red giants (see e.g., Cantiello et al. 2014), the rest of the values were chosen based on the calibration performed for a RGB star in chapter 5, and all the non-disclosed remaining parameters are the same as in Fuller et al. (2019), also described in chapter 4.

Mass

To test the sensitivity of rotation rates in models with the Fuller-formalism to the initial mass along evolution, all models were generated with identical starting conditions to the benchmark model but different initial masses. In the top left panel of figure 6.2 we show the evolution of core and surface rotation rates of models with initial masses ranging between 1-2 $M_{\odot}$, starting from the zero age main-sequence and ending right above the red giant bump.

An increase in the mass leads to a decrease in the core rotation rate, and this is particularly notorious at the end of the subgiant phase. The surface rotation rate also decreases with mass, however the difference is less significant than in the core. This behavior is expected according to equation (3.14) as $\nu_{\rm AM} \sim R^2$. Since more massive stars have higher radius models, they have more efficient angular momentum transport. The increase in efficiency of transport of angular momentum leads to a decrease of core rotation. Since there is a visible change due to increase of mass, this means that the increase of radius in the later stages possibly overpowers the other quantities (e.g., local rotation and Brunt-Väissälä) in the coefficient of transport of angular momentum using Fuller-formalism prescription (equation (3.14)). Lastly, we observe that the degree of differential rotation in the models increases slowly with mass from the end of the subgiant phase.

Metallicity

The top right panel of figure 6.2 illustrates the evolution of core and surface rotation rates of models with surface gravity for initial metallicities ranging between $Z = 0.015 - 0.045$.

The major differences in core rotation rates due to initial composition lay in the main-sequence and subgiant phase. The lower metallicity models show shorter total lifetimes. At the end of subgiant phase, the lower metallicity models reach higher helium core radius, which according to equation (3.14) translates roughly into higher viscosity and more efficient transport of angular momentum to the outer layers, thus lower rotation rates.

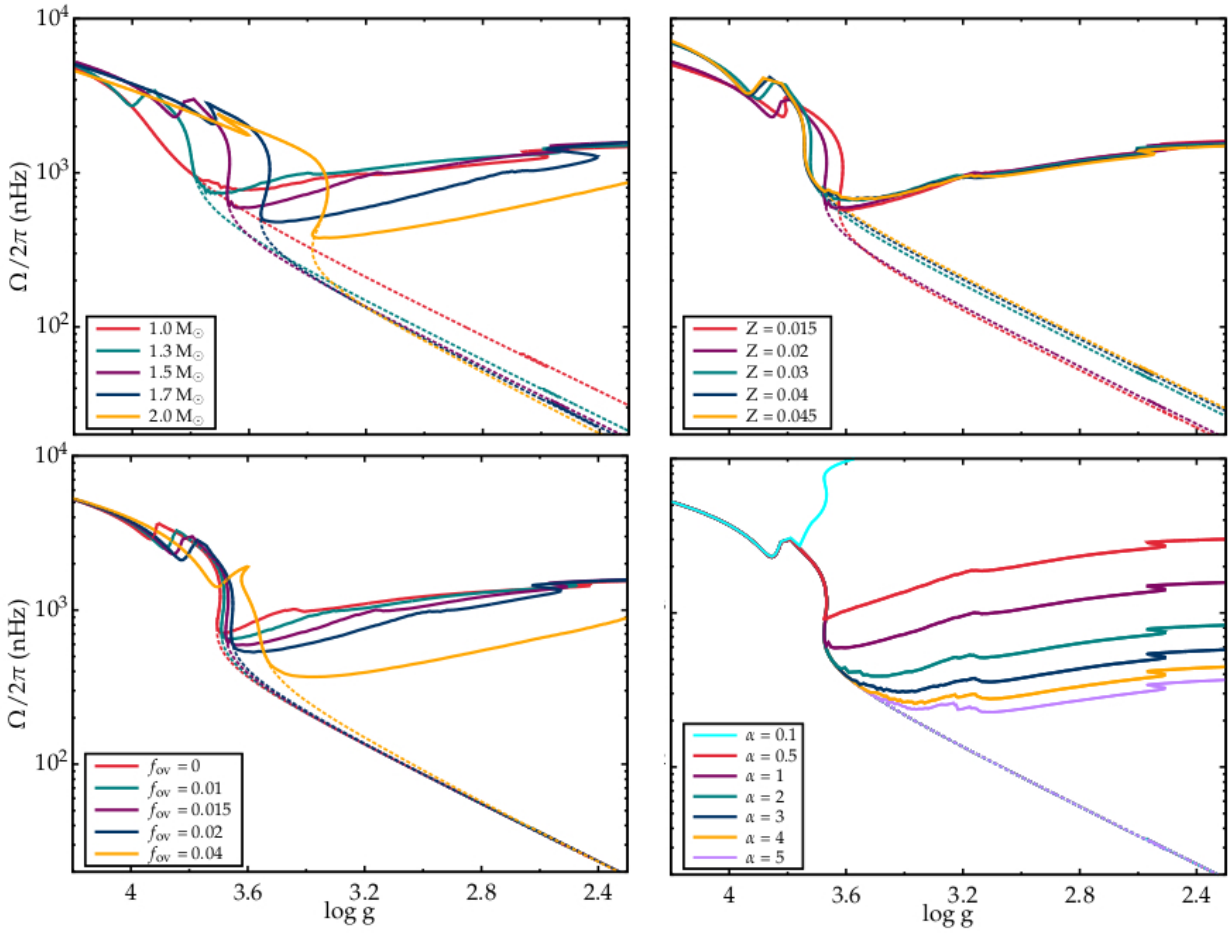

Figure 6.2: Rotation rates as a function of the surface gravity. The full (dashed) line indicates the core (surface) rotation models. The benchmark model is marked in purple. Top left panel illustrates models with different masses ranging between 1-2 $M_\odot$. Top right panel with different metallicities between Z = 0.015-0.045. Bottom left panel with different overshooting parameters between $f_{\rm ov}$ = 0-0.04. Bottom right panel with different α parameter values between α = 0.1-5. The input physics of the stellar models is described in the text.

As the star moves along the red giant branch this situation is inverted. The more metal rich stars expand more than the metal poor ones (as seen in van Saders and Pinsonneault 2013), thus increasing the efficiency of transport of angular momentum in their cores and consequently slowing them down. Despite the metal rich models reaching higher rotations in the initial stages of evolution, in the late stages they have slowed down and met the rotation rates of the metal poor ones. The top right panel of figure 6.2 shows that the core rotation of different metallicity models is almost unaffected in the red giant branch while surface rotation rates are visibly affected, since metal rich models reach higher surface rotation rates. Hence, more metal rich models develop a lower degree of radial differential rotation in later stages of evolution.

Convective overshooting

The overshooting parameter $f_{\rm ov}$ is a scaling parameter and when reduced to zero makes the boundary between the radiative interior and the outer convective zone in stellar models extremely sharp. In literature

the adopted value for $f_{\rm ov}$ is around 0.016 (Herwig 2000), hence we tested a range between $f_{\rm ov} = 0 - 0.04$ (as in Paxton et al. 2013) to understand the impact this parameter has in the rotation rate of our stellar models.

The bottom left panel of figure 6.2 illustrates the evolution of core and surface rotation with the surface gravity for various $f_{\rm ov}$. Increasing overshooting affects the stellar models similarly as increasing initial masses but with more emphasis in the red giant phase, improving the efficiency of internal transport of angular momentum. The impact on the surface rotation rate of these models is negligible. The degree of radial differential rotation slowly decreases with increase overshooting.

α parameter

The efficiency of transport of angular momentum relies in the coefficient of equation (3.14). An increase in α enhances the efficiency of transport and core spin down, since $\nu_{\rm AM} \propto \alpha^3$. According to Fuller et al. (2019), the α parameter has an even more significant impact in the computation of the minimum shear $q_{\rm min} \propto \alpha^{-3}$ for the instability to occur. α leads to a decrease in $q_{\rm min}$, so when $q > q_{\rm min}$, efficient angular momentum transport will tend to decrease the shear until $q \sim q_{\rm min}$ and consequently the reduce the core rotation. The bottom right panel of figure 6.2 illustrates the evolution of core and surface rotation with the surface gravity for α ranging between 0.1-5 (values decided according to recent studies in this variable; Fuller et al. 2019; Eggenberger et al. 2019; den Hartogh et al. 2020).

The minimum shear in equation (3.15) also shows a dependence on the effective Brunt-Väissälä frequency. The shear is strongest where the compositional component N^2_μ is large due to stratification, and that is at the H-burning shell in the subgiant and red giant stages. As such, we expect the mechanism to be more effective in those phases.

As expected, figure 6.2 reveals a significant impact in the core rotation rate in the sungiant and red giant stages with increasing α parameter, and none at the main-sequence where the models experience solid body rotation. The age at which the spin up of the core happens suffers a delay with the increase of α. Higher efficiency of transport of angular momentum prevents the spin up of the core: with a lower α the core spins up during the subgiant phase whereas with a higher α the core only spins up in the early red giant phase. In the red giant phase the core rotation rate decreases up to an order in magnitude ($\Omega_{\rm core} \in$ [200-2000 nHz]) with increase α. The surface rotation rates are unaffected by this parameter.Hence, the models with faster core rotation (e.g., $\alpha = 0.5$) develop a higher degree of radial differential rotation.

6.3 Constraining the α parameter

As observed in the previous section (6.2), the α parameter of the Fuller-formalism has a very significant impact in the evolution of core rotation rate and angular momentum transport efficiency. Figure 4 of Fuller et al. (2019), shows a range of values for this parameter $\alpha \in [0.5 - 2]$ with different initial spin rates P_i, that are able to reproduce the core rotation of a limited sample of red giants, red clumps and white dwarfs.

Using the asteroseismic data from figure 6.1 that contains a broader range of core and surface rotation rates of main-sequence, subgiant, red giant, and red clump stars than Fuller et al. (2019), we aim to establish new limits for the α parameter. To do so, we build two models: one that aims to reproduce the core and surface rotation rate of fast rotators (fast track) and a second for slow rotators (slow track), using the Fuller-formalism. To achieve this, we created two sets of models: in the first set (top panel of figure 6.3), the initial rotation period P_i for the fast and slow track models (green and purple) was fixed to match the maximum and minimum observed rotation rates of main-sequence stars. In the second set (bottom panel of figure 6.3), P_i for the fast and slow track models (blue and orange) was allowed to vary. In both sets, the α parameter was chosen to match the core rotation rates of subgiant, red giant, and red clump stars. All models in figure 6.3 were computed with an initial mass of 1.5 $M_\odot$, Z$= 0.02$, $f_{\rm ov} = 0.015$ and $\alpha_{\rm mlt} = 2$, the rest of parameters are the same as in Fuller et al. (2019), described in chapter 4.

The lower amount of subgiant stars in figure 6.3 does not give a good representation of the core and surface rotation rates, mass and metallicity of those stars. More asteroseismic data from those stars is needed in order to fully determine their range of rotation rates and constrain stellar models. Taking that information into consideration, for the sole purpose of this discussion we will be using those values as our guide for the subgiant rotation rates. The same principle applies to the main-sequence stars in this discussion. Even tough we gathered a significant amount of those stars, they are sparsely distributed in figure 6.3.

For the two sets of models in figure 6.3 we obtained the same α parameter values for the fast and slow tracks $\alpha = 0.5$ and $\alpha = 5$, respectively. $\alpha = 0.5$ is needed to model the subgiant, red giant and red clump fast rotators. At least $\alpha = 5$ is needed to model the slow rotators in the red giant and red clump phase. However, even this α value is not enough to reach the lowest core rotation rates. Increasing the α even more shows small to no improvement in slowing down the core, as can be seen in the bottom panel of figure 6.2. Increasing the mass or the convective overshooting would however reach the desired results, hence we defined the limit to be $\alpha = 5$.

Models with the same α converge to the same core rotation rates in the red giant branch, independently of the imposed initial rotation. This can become a problem in stellar modeling, since there are other factors that we do not take into account (e.g., magnetic braking, anisotropic winds, binary stars) that also have a great impact in the rotation, and that the α could possibly overpower.

The α parameter varying between 0.5 and 5 implies that the viscosity coefficient has to vary between 0.125 to 125 due to the cube dependence on α. Corresponding to a variation of 3 orders of magnitude

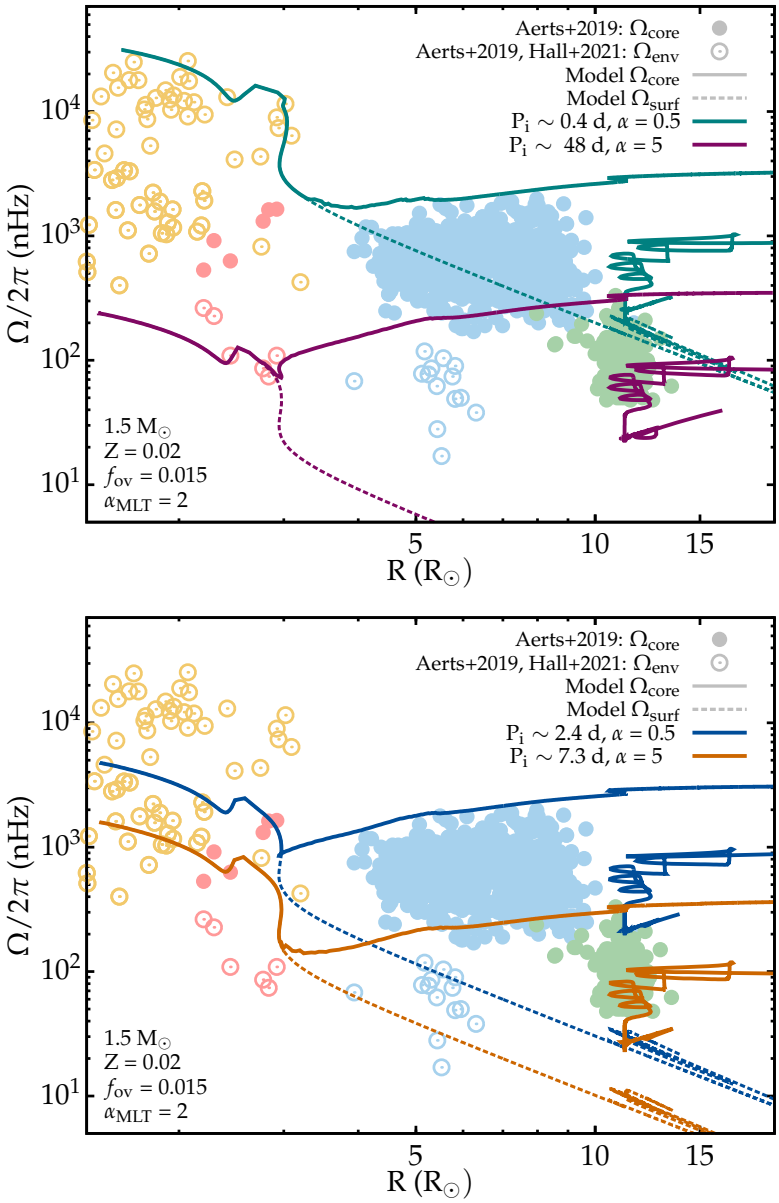

Figure 6.3: Core and surface (solid and dashed lines) rotation rates as a function of stellar radius from the ZAMS until RC phase. Top panel: models constraining the initial periods of the models to match the MS fastest and slowest rotators. Bottom panel: models where the initial period was not constrained. The data points are the same as in figure 6.1.

both in the viscosity coefficient and in the required shear for the Tayler instability to saturate. Hence, the degree of freedom of this parameter is compensating for important missing physics not included in the Fuller-formalism, as discussed in previous reviews.

In early main-sequence stages the core and surface rotation rates strongly depend on the initial rotation rate. The initial rotation period also has an impact in the model's age – lower initial periods seem to generate younger evolutionary tracks. Besides, there is also a strong dependence of the viscosity on the local spin

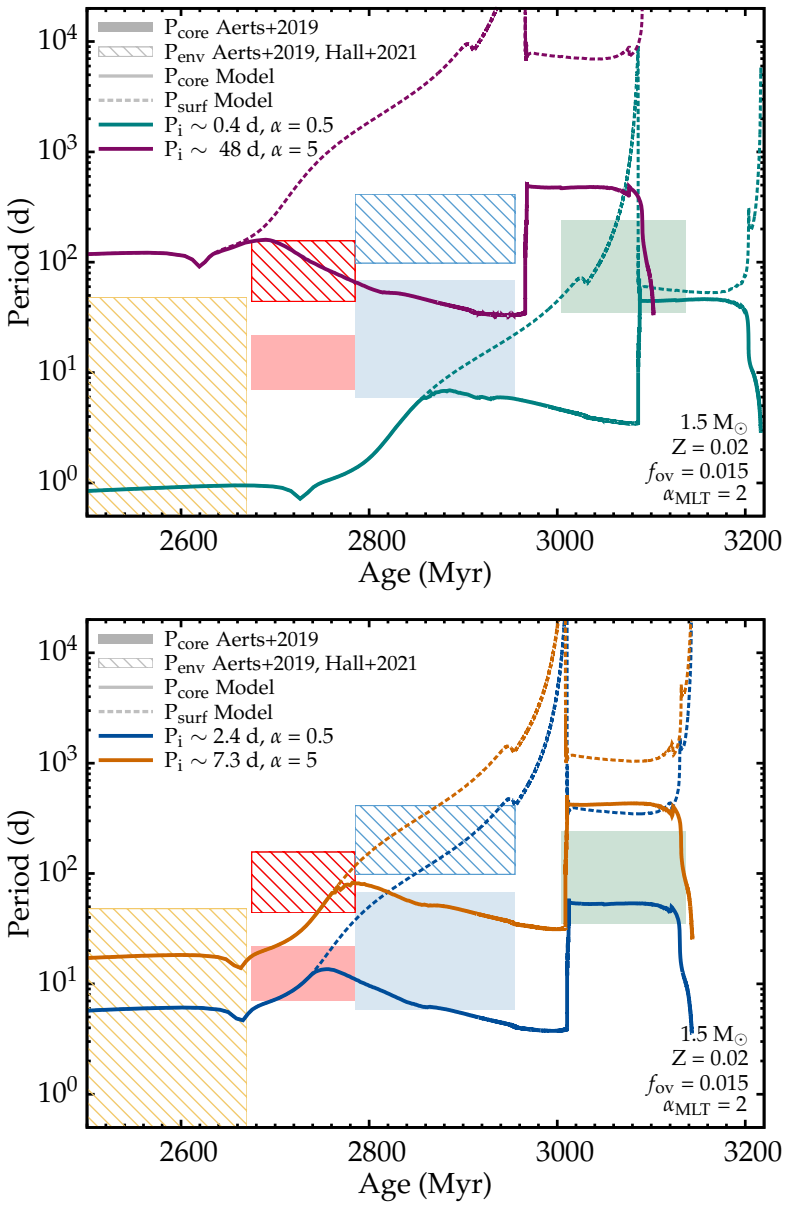

Figure 6.4: Core and surface (solid and dashed lines) rotation period as a function of stellar age from the ZAMS until RC phase. Top panel: models constraining the initial periods of the models to match the MS fastest and slowest rotators. Bottom panel: models where the initial period was not constrained. The boxes refer to data in figure 6.1 with estimates of the ages for the evolution of a 1.5 $M_\odot$ star. Filled (stripped) boxes correspond to core (surface or envelope) periods. Boxes in yellow, red, blue and green correspond to estimated MS, SGB, RGB and RC stars rotation rates, respectively.

rate, $\nu_F \propto \Omega^3$ (Fuller et al. 2019). As such, the fast track (top panel of figure 6.3) in the early stages experiences a stronger decrease in rotation, although not enough to slow down the core to match the subgiant measurements. In later stages, the core rotation evolution is poorly affected by the initial rotation period.

In this section we abstain to discuss the effects of fast rotation in the stellar surface (see appendix A for

a brief study). Nonetheless, the fastest main-sequence stars in our data are in a rotation range were their surface variables will be substantially affected by the centrifugal force.

The surface rotation in not affected by the α parameter variations, on the other hand it highly depends on the rotation imposed at the zero age main-sequence. Therefore, surface rotation rates in the top panel of Figure 6.3 do not match subgiants and red giants measured rates, whereas the bottom panel of figure 6.3 shows a better agreement with observations.

Figures 6.4 illustrate the evolution of core and surface rotation period with the age of Fuller-formalism models, for the two sets of models. The bottom panel of figure 6.4 shows models with a good match for the lower and higher rotation periods of subgiant and red giant stars. The Fuller-formalism predicts slightly higher periods for the red clump fastest and slowest rotators, nonetheless the results are still very close to observations.

Our attempt to create a fast and slow rotation track to constraint the observed rotation rates, revealed that the Fuller-formalism overestimates the spin down of the core between the red giant and red clump phase. We explored changing the α parameter after the red giant bump to compensate this effect, however it did not reproduce the desired results. Since most of the angular momentum extraction in these models happens in the subgiant and red giant phase. And at later stages, due to the large stabilizing composition gradients, the rotation rates are reproduced with conservation of angular momentum (e.g., Cantiello et al. 2014, Fuller et al. 2019).

We can compare (indirectly) the figure 6.4 with 6.1, since the radius of the stars in this range of mass between the main-sequence and red giant increases with age. Figure 6.4 shows a positive slope in the period of subgiant models and a negative slope in the period of red giant models in opposition to values in equation 6.1. Although, the Fuller-formalism models matches the observed core rotation rates, the evolutionary tracks of this models divergences from the fits performed to the measured rotation rates, revealing some inaccuracies in the formalism.

Chapter 7

Conclusions

In this thesis we focused on overall aspects of rotation in red giant stars, more precisely the transport of angular momentum and mixing of chemical elements in radiative zones of 1-2 solar mass stars.

The recent measurements of gravity dominated mixed modes in red giant stars showed slower core rotation rates than predictions, leading to the inevitable conclusion that a more efficient transfer of angular momentum is needed in current stellar models to explain the discrepancies. Transport processes in stellar interiors are extremely complex. Despite several proposed theories, there is still no consensus on the mechanisms responsible for the observed core rotation rates.

7.1 Achievements

In the first part of this work, we concluded that the inner regions of evolved stars are mainly affected by diffusive transport processes. We performed side-by-side comparisons of four mechanisms of transport of angular momentum that corroborated the small impact of different transport mechanisms in variables not related to rotation in red giant stars. We successfully reproduced the observed asteroseismic core rotation rate of a red giant star making use of a recently proposed mechanism based on the Tayler instability. The inherent calibration of the free parameter in this theory revealed a higher value than was initially proposed for red giant stars.

We implemented for the first time the rotational-driven mixing coefficient of the Fuller-formalism in the interior of red giant stars. Comparisons of the efficiency of three transport processes revealed expected, albeit important results. The efficiency of mixing induced by rotation is overestimated in less efficient transport mechanisms due to higher core rotation predictions. Our study shows that the inclusion of mixing increases slightly the efficiency of angular momentum transport.

Using the previous results, we carried out calculations for the oscillation mode frequencies. We verified the mixed mode period spacing pattern present in red giant stars. The period spacing and the frequency splitting of mixed modes showcased clear distinctions between different transport processes and small ones between mixing processes. This notable result confirms that asteroseismic derived rotational mixed mode

splittings are a great tool to probe the values of the diffusion coefficient for angular momentum transfer, and a potential tool to study the mixing of chemical elements in evolved stars.

Lastly, we performed a further study on the Fuller-formalism. Based on our results, the transport efficiency is particularly sensitive to variations on the initial stellar mass and less dependent on the metallicity and convective overshooting. With that information, we performed a calibration on the α parameter. Asteroseismic derived rotational splittings from a considerable amount of main sequence to red clump stars were used to constraint the models. We established new limits for the α parameter of the Fuller-formalism using a wide range of rotators with 1-2 solar masses.

7.2 Future Work

Further advances in this field of study are largely dependent on upcoming discoveries in asteroseismology. In this work, the low number of asteroseismic rotation data for subgiant stars constituted a limitation when obtaining the range of rotation for those stars. More asteroseismic data of those stars is needed to constraint with high precision the rotation profiles of stellar evolutionary models. The space missions COROT and *Kepler* already provided a considerable amount of stellar oscillation data of main-sequence, red giants and white-dwarfs. The on-going TESS mission and the future PLATO mission (expected to launch in 2026) will hopefully survey an increasingly higher amount of stars with unprecedented precision.

In order to perform a more in-depth study on the impact of rotation-induced chemical mixing of the Tayler-Spruit dynamo and the Fuller-formalism, one needs to include a more complex table of nuclear reactions in models than what was considered in this work. This would allow to obtain computational abundances of crucial observational tracers such as lithium, ^{12}C/^{13}C, nitrogen and others. Additionally, different targets with spectroscopic measurements for these species would also have to considered to perform side-by-side comparisons.

Another important aspect to consider in future work is the contribution of both magnetic fields and internal gravity waves to a complete description of angular momentum and rotation-induced chemical mixing in stellar radiative interiors.

Bibliography

Abolfathi, B. et al. (2017). “The Fourteenth Data Release of the Sloan Digital Sky Survey: First Spectroscopic Data from the Extended Baryon Oscillation Spectroscopic Survey and from the Second Phase of the Apache Point Observatory Galactic Evolution Experiment”. In: *Astrophysical Journal Supplement Series* 235, pp. 42–42. DOI: 10.3847/1538-4365/aa9e8a.

Aerts, C. (2021). “Probing the interior physics of stars through asteroseismology”. In: *Reviews of Modern Physics* 93.1. DOI: 10.1103/revmodphys.93.015001.

Aerts, C., Christensen-Dalsgaard, J., and Kurtz, D. W. (2010). *Asteroseismology*. Springer. DOI: 10.1007/978-1-4020-5803-5.

Aerts, C., Mathis, S., and Rogers, T. M. (2019). “Angular Momentum Transport in Stellar Interiors”. In: *Annual Review of Astronomy and Astrophysics* 57.1, pp. 35–78. DOI: 10.1146/annurev-astro-091918-104359.

Aerts, C., T. Van Reeth, and A. Tkachenko (2017). “The Interior Angular Momentum of Core Hydrogen Burning Stars from Gravity-mode Oscillations”. In: *The Astrophysical Journal* 847.1, p. L7. DOI: 10.3847/2041-8213/aa8a62.

Aguirre, V. S. et al. (2017). “Standing on the Shoulders of Dwarfs: theiKepler/iAsteroseismic LEGACY Sample. II. Radii, Masses, and Ages”. In: *The Astrophysical Journal* 835.2, p. 173. DOI: 10.3847/1538-4357/835/2/173.

Angulo, C. et al. (1999). “A compilation of charged-particle induced thermonuclear reaction rates”. In: *Nuclear Physics A* 656.1, pp. 3–183. DOI: 10.1016/S0375-9474(99)00030-5.

Baglin, A., M. Auvergne, P. Barge, E. Michel, C. Catala, M. Deleuil, and W. Weiss (2007). “The CoRoT mission and its scientific objectives”. In: *AIP Conference Proceedings* 895.1, pp. 201–209. DOI: 10.1063/1.2720423.

Bahcall, J. N., A. M. Serenelli, and S. Basu (2006). “10,000 Standard Solar Models: A Monte Carlo Simulation”. In: *The Astrophysical Journal Supplement Series* 165.1, pp. 400–431. DOI: 10.1086/504043.

Barrère, P., J. Guilet, A. Reboul-Salze, R. Raynaud, and H. -T. Janka (2022). “A new scenario for magnetar formation: Tayler-Spruit dynamo in a proto-neutron star spun up by fallback”. In: DOI: 10.48550/ARXIV.2206.01269.

Beck, P. G. et al. (2011). “Kepler Detected Gravity-Mode Period Spacings in a Red Giant Star”. In: *Science* 332.6026, p. 205. DOI: 10.1126/science.1201939.

Beck, P. G. et al. (2012). “Fast core rotation in red-giant stars as revealed by gravity-dominated mixed modes”. In: *Nature* 481.7379, pp. 55–57. DOI: 10.1038/nature10612.

Bedding, T. R. et al. (2011). “Gravity modes as a way to distinguish between hydrogen- and helium-burning red giant stars”. In: *Nature* 471.7340, pp. 608–611. DOI: 10.1038/nature09935.

Blöcker, T. (1995). “Stellar evolution of low and intermediate-mass stars. I. Mass loss on the AGB and its consequences for stellar evolution.” In: 297, p. 727.

Borucki, W. et al. (2010). “Kepler Planet-Detection Mission: Introduction and First Results”. In: *Science (New York, N.Y.)* 327, pp. 977–80. DOI: 10.1126/science.1185402.

Cantiello, M., C. Mankovich, L. Bildsten, J. Christensen-Dalsgaard, and B. Paxton (2014). “Angular momentum transport within evolved low-mass stars”. In: *The Astrophysical Journal* 788.1, p. 93. DOI: 10.1088/0004-637x/788/1/93.

Capelo, D. and I. Lopes (2020). “The impact of composition choices on solar evolution: age, helio- and asteroseismology, and neutrinos”. In: *Monthly Notices of the Royal Astronomical Society* 498.2, pp. 1992–2000. DOI: 10.1093/mnras/staa2402.

Carroll, B.W. and D.A. Ostlie (2007). *An introduction to modern astrophysics; 2nd ed.* San Francisco, CA: Addison-Wesley.
Chaplin, W. J. and A. Miglio (2013). “Asteroseismology of Solar-Type and Red-Giant Stars”. In: 51.1, pp. 353–392. DOI: 10.1146/annurev-astro-082812-140938.
Charbonnel, C. and N. Lagarde (2010). “Thermohaline instability and rotation-induced mixing. I. Low- and intermediate-mass solar metallicity stars up to the end of the AGB”. In: 522, A10, A10. DOI: 10.1051/0004-6361/201014432.
Charbonnel, C. and S. Talon (2005). “Influence of Gravity Waves on the Internal Rotation and Li Abundance of Solar-Type Stars”. In: *Science* 309.5744, pp. 2189–2191. DOI: 10.1126/science.1116849.
Christensen-Dalsgaard, J. (1997). “Lecture Notes on Stellar Oscillations”. In:
— (2002). “Helioseismology”. In: *Rev. Mod. Phys.* 74 (4), pp. 1073–1129. DOI: 10.1103/RevModPhys.74.1073.
— (2021). “Solar structure and evolution”. In: *Living Reviews in Solar Physics* 18.1. DOI: 10.1007/s41116-020-00028-3.
Christensen-Dalsgaard, J. et al. (2020). “The Aarhus red giants challenge - II. Stellar oscillations in the red giant branch phase”. In: *A&A* 635, A165. DOI: 10.1051/0004-6361/201936766.
Claverie, A., G. R. Isaak, C. P. McLeod, H. B. van der Raay, and T. Roca Cortes (1980). “Structure in the 5 minute oscillations of integral sunlight”. In: 91.3, p. L9.
Cowling, T. G. (1941). “The Non-radial Oscillations of Polytropic Stars”. In: *Monthly Notices of the Royal Astronomical Society* 101.8, pp. 367–375. DOI: 10.1093/mnras/101.8.367.
Cox, J. P. (1980). *Theory of Stellar Pulsation. (PSA-2)*. Princeton University Press.
Cox, J. P. and R. T. Giuli (1968). *Principles of stellar structure*.
Cunha, M. S., D. Stello, P. P. Avelino, J. Christensen-Dalsgaard, and R. H. D. Townsend (2015). “Structural glitches near the cores of red giants revealed by oscillations in g-mode period spacings from stellar models”. In: *The Astrophysical Journal* 805.2, p. 127. DOI: 10.1088/0004-637x/805/2/127.
Deheuvels, S. et al. (2014). “Seismic constraints on the radial dependence of the internal rotation profiles of six Kepler subgiants and young red giants”. In: *A&A* 564, A27. DOI: 10.1051/0004-6361/201322779.
den Hartogh, J. W., Eggenberger, P., and Deheuvels, S. (2020). “Asteroseismology of evolved stars to constrain the internal transport of angular momentum - III. Using the rotation rates of intermediate-mass stars to test the Fuller-formalism”. In: *A&A* 634, p. L16. DOI: 10.1051/0004-6361/202037568.
Denissenkov, P. A. and M. Pinsonneault (2007). “A Revised Prescription for the Tayler-Spruit Dynamo: Magnetic Angular Momentum Transport in Stars”. In: *The Astrophysical Journal* 655.2, pp. 1157–1165. DOI: 10.1086/510345.
Dupret, M.-A. et al. (2009). “Theoretical amplitudes and lifetimes of non-radial solar-like oscillations in red giants*”. In: *A&A* 506.1, pp. 57–67. DOI: 10.1051/0004-6361/200911713.
Dziembowski, W. A. (1971). “Nonradial Oscillations of Evolved Stars. I. Quasiadiabatic Approximation”. In: 21, pp. 289–306.
Eddington, A. S. (1926). “The internal constitution of the stars”. In: *Cambridge University Press* 1st edition.
Eggenberger, P., den Hartogh, J. W., Buldgen, G., Meynet, G., Salmon, S. J. A. J., and Deheuvels, S. (2019). “Asteroseismology of evolved stars to constrain the internal transport of angular momentum - II. Test of a revised prescription for transport by the Tayler instability”. In: *A&A* 631, p. L6. DOI: 10.1051/0004-6361/201936348.
Endal, A. S. and S. Sofia (1976). “The evolution of rotating stars. I. Method and exploratory calculations for a 7 M sun star.” In: 210, pp. 184–198. DOI: 10.1086/154817.
— (1978). “The evolution of rotating stars. II. Calculations with time-dependent redistribution of angular momentum for 7 and 10 M sun stars.” In: 220, pp. 279–290. DOI: 10.1086/155904.
Frebel, A. et al. (2005). “Nucleosynthetic signatures of the first stars”. In: *Nature* 434.7035, pp. 871–873. DOI: 10.1038/nature03455.
Fuller, J., Piro, A. L., and Jermyn, A. S. (2019). “Slowing the spins of stellar cores”. In: *Monthly Notices of the Royal Astronomical Society* 485.3, pp. 3661–3680. DOI: 10.1093/mnras/stz514.
García, R. A., S. Turck-Chièze, S. J. Jiménez-Reyes, J. Ballot, P. L. Pallé, A. Eff-Darwich, S. Mathur, and J. Provost (2007). “Tracking Solar Gravity Modes: The Dynamics of the Solar Core”. In: *Science* 316.5831, pp. 1591–1593. DOI: 10.1126/science.1140598.

Gehan, C., Mosser, B., Michel, E., Samadi, R., and Kallinger, T. (2018). “Core rotation braking on the red giant branch for various mass ranges”. In: *A&A* 616, A24. DOI: 10.1051/0004-6361/201832822.
Georgy, C., Meynet, G., and Maeder, A. (2011). “Effects of anisotropic winds on massive star evolution”. In: *A&A* 527, A52. DOI: 10.1051/0004-6361/200913797.
Gratton, R. G., C. Sneden, E. Carretta, and A. Bragaglia (2000). “Mixing along the red giant branch in metal-poor field stars”. In: 354, pp. 169–187.
Hall, O. J. et al. (2021). “Weakened magnetic braking supported by asteroseismic rotation rates of Kepler dwarfs”. In: *Nature Astronomy* 5.7, pp. 707–714. DOI: 10.1038/s41550-021-01335-x.
Handler, Gerald (2013). “Asteroseismology”. In: *Planets, Stars and Stellar Systems*. Springer Netherlands, pp. 207–241. DOI: 10.1007/978-94-007-5615-1_4.
Heger, A., Langer, N., and Woosley, S. E. (2000). “Presupernova Evolution of Rotating Massive Stars. I. Numerical Method and Evolution of the Internal Stellar Structure”. In: *The Astrophysical Journal* 528.1, pp. 368–396. DOI: 10.1086/308158.
Hekker, S. and J. Christensen-Dalsgaard (2017). “Giant star seismology”. In: *The Astronomy and Astrophysics Review* 25.1. DOI: 10.1007/s00159-017-0101-x.
Hekker, S., Kallinger, T., Baudin, F., De Ridder, J., Barban, C., Carrier, F., Hatzes, A. P., Weiss, W. W., and Baglin, A. (2009). “Characteristics of solar-like oscillations in red giants observed in the CoRoT exoplanet field ***”. In: *A&A* 506.1, pp. 465–469. DOI: 10.1051/0004-6361/200911858.
Herwig, F. (2000). “The evolution of AGB stars with convective overshoot”. In: 360, pp. 952–968.
Houdek, G. and M.-A. Dupret (2015). “Interaction Between Convection and Pulsation”. In: *Living Reviews in Solar Physics* 12.1, 8, p. 8. DOI: 10.1007/lrsp-2015-8.
Huber, D. et al. (2011). “Testing scaling relations for solar-like oscillations from the main sequence to red giants using iKEPLER/i data”. In: *The Astrophysical Journal* 743.2, p. 143. DOI: 10.1088/0004-637x/743/2/143.
Iglesias, C. A. and F. J. Rogers (1996). “Updated Opal Opacities”. In: 464, p. 943. DOI: 10.1086/177381.
Karttunen, H., P. Kröger, H. Oja, M. Poutanen, and K.J. Donner (2007). *Fundamental astronomy; 5th ed.* Berlin, Heidelberg: Springer. DOI: 10.1007/978-3-540-34144-4.
Kippenhahn, R. and H.-C. Thomas (1970). “A Simple Method for the Solution of the Stellar Structure Equations Including Rotation and Tidal Forces”. In: *International Astronomical Union Colloquium* 4, pp. 20–29. DOI: 10.1017/S0252921100027007.
Kippenhahn, R., A. Weigert, and A. Weiss (2013). *Stellar Structure and Evolution*. DOI: 10.1007/978-3-642-30304-3.
Kissin, Y. and C. Thompson (2015). “Rotation of Giant Stars”. In: 808.1, 35, p. 35. DOI: 10.1088/0004-637X/808/1/35.
Kjeldsen, H. and T. R. Bedding (1995). “Amplitudes of stellar oscillations: the implications for asteroseismology.” In: 293, pp. 87–106. arXiv: astro-ph/9403015 [astro-ph].
Kjeldsen, H., T. R. Bedding, M. Viskum, and S. Frandsen (1995). “Solarlike Oscillations in eta Boo”. In: 109, p. 1313. DOI: 10.1086/117363.
Koch, D. G. et al. (2010). “KEPLER mission design, realized photometric performance, and early science”. In: *The Astrophysical Journal* 713.2, pp. L79–L86. DOI: 10.1088/2041-8205/713/2/l79.
Kraft, R. P. (1967). “Studies of Stellar Rotation. V. The Dependence of Rotation on Age among Solar-Type Stars”. In: 150, p. 551. DOI: 10.1086/149359.
Lagarde, N., C. Charbonnel, T. Decressin, and J. Hagelberg (2011). “Thermohaline instability and rotation-induced mixing. II. Yields of ^{3}He for low- and intermediate-mass stars”. In: 536, A28, A28. DOI: 10.1051/0004-6361/201117739.
Ledoux, P. (1951). “The Nonradial Oscillations of Gaseous Stars and the Problem of Beta Canis Majoris.” In: 114, p. 373. DOI: 10.1086/145477.
Lee, U. and H. Saio (1987a). “Low-frequency oscillations of uniformly rotating stars”. In: *Monthly Notices of the Royal Astronomical Society* 224.3, pp. 513–526. DOI: 10.1093/mnras/224.3.513.
— (1987b). “Non-adiabatic analysis of low-frequency oscillations of uniformly rotating stars”. In: *Monthly Notices of the Royal Astronomical Society* 225.3, pp. 643–651. DOI: 10.1093/mnras/225.3.643.
Ma, L. and J. Fuller (2019). “Angular momentum transport in massive stars and natal neutron star rotation rates”. In: *Monthly Notices of the Royal Astronomical Society* 488.3, pp. 4338–4355. DOI: 10.1093/mnras/stz2009.

Maeder, A. (2009). *Physics, Formation and Evolution of Rotating Stars*. DOI: 10.1007/978-3-540-76949-1.
Maeder, A. and G. Meynet (2000). "The Evolution of Rotating Stars". In: *Annual Review of Astronomy and Astrophysics* 38.1, pp. 143–190. DOI: 10.1146/annurev.astro.38.1.143.
— (2004). "Stellar evolution with rotation and magnetic fields". In: *Astronomy &amp Astrophysics* 422.1, pp. 225–237. DOI: 10.1051/0004-6361:20034583.
Majewski, S. R. et al. (2017). "The Apache Point Observatory Galactic Evolution Experiment (APOGEE)". In: *The Astronomical Journal* 154.3, p. 94. DOI: 10.3847/1538-3881/aa784d.
Marques, J. P. et al. (2013). "Seismic diagnostics for transport of angular momentum in stars - I. Rotational splittings from the pre-main sequence to the red-giant branch". In: *A&A* 549, A74. DOI: 10.1051/0004-6361/201220211.
Meynet, G. and A. Maeder (1997). "Stellar evolution with rotation. I. The computational method and the inhibiting effect of the μ-gradient." In: 321, pp. 465–476.
Mosser, B. et al. (2011). "Mixed modes in red-giant stars observed with CoRoT". In: *Research Policy - RES POLICY* 532. DOI: 10.1051/0004-6361/201116825.
Mosser, B. et al. (2012). "Spin down of the core rotation in red giants". In: 548, A10, A10. DOI: 10.1051/0004-6361/201220106.
Nelder, J. A. and R. Mead (1965). "A Simplex Method for Function Minimization". In: *The Computer Journal* 7.4, pp. 308–313. ISSN: 0010-4620. DOI: 10.1093/comjnl/7.4.308.
Palacios, A. (2013). "Influence of Rotation on Stellar Evolution". In: *EAS Publications Series* 62, pp. 227–287. DOI: 10.1051/eas/1362007.
Paxton, B., Bildsten, L., Dotter, A., Herwig, F., Lesaffre, P., and Timmes, F. (2011). In: *ApJS* 192, 3, p. 3. DOI: 10.1088/0067-0049/192/1/3.
Paxton, B. et al. (2013). In: *ApJS* 208, 4, p. 4. DOI: 10.1088/0067-0049/208/1/4.
Paxton, B. et al. (2015). In: *ApJS* 220, 15, p. 15. DOI: 10.1088/0067-0049/220/1/15.
Paxton, B. et al. (2018). In: *ApJS* 234, 34, p. 34. DOI: 10.3847/1538-4365/aaa5a8.
Paxton, B. et al. (2019). In: *ApJS* 243.1, 10, p. 10. DOI: 10.3847/1538-4365/ab2241.
Pinsonneault, M. H., Steven D. Kawaler, S. Sofia, and P. Demarque (1989). "Evolutionary Models of the Rotating Sun". In: 338, p. 424. DOI: 10.1086/167210.
Pinsonneault, M. H. et al. (2018). "The Second APOKASC Catalog: The Empirical Approach". In: *The Astrophysical Journal Supplement Series* 239.2, p. 32. DOI: 10.3847/1538-4365/aaebfd.
Pitts, E. and R. J. Tayler (1985). "The adiabatic stability of stars containing magnetic fields. IV - The influence of rotation". In: 216, pp. 139–154. DOI: 10.1093/mnras/216.2.139.
Rauer, H. et al. (2014). "The PLATO 2.0 mission". In: *Experimental Astronomy* 38, p. 249. DOI: 10.1007/s10686-014-9383-4.
Reimers, D. (1975). "Circumstellar absorption lines and mass loss from red giants." In: *Memoires of the Societe Royale des Sciences de Liege* 8, pp. 369–382.
Ricker, G. R. et al. (2014). "Transiting Exoplanet Survey Satellite". In: *Journal of Astronomical Telescopes, Instruments, and Systems* 1.1, p. 014003. DOI: 10.1117/1.jatis.1.1.014003.
Rieutord, M., F. Espinosa Lara, and B. Putigny (2016). "An algorithm for computing the 2D structure of fast rotating stars". In: *Journal of Computational Physics* 318, pp. 277–304. DOI: 10.1016/j.jcp.2016.05.011.
Rogers, F. J. and A. Nayfonov (2002). "Updated and Expanded OPAL Equation-of-State Tables: Implications for Helioseismology". In: *The Astrophysical Journal* 576.2, pp. 1064–1074. DOI: 10.1086/341894.
Rogers, T. M., Lin, D.N.C., McElwaine, J.N., and Lau, H.H.B. (2013). "Internal gravity waves in massive stars: angular momentum transport". In: *The Astrophysical Journal* 772.1, p. 21. DOI: 10.1088/0004-637x/772/1/21.
Shibahashi, H. (1979). "Modal Analysis of Stellar Nonradial Oscillations by an Asymptotic Method". In: 31, pp. 87–104.
Sills, A., M. H. Pinsonneault, and D. M. Terndrup (2000). "The Angular Momentum Evolution of Very Low Mass Stars". In: *The Astrophysical Journal* 534.1, pp. 335–347. DOI: 10.1086/308739.
Somers, G. and M. H. Pinsonneault (2016). "Lithium depletion is a strong test of core-envelope recoupling". In: *The Astrophysical Journal* 829.1, p. 32. DOI: 10.3847/0004-637x/829/1/32.
Spruit, H. C. (2002). "Dynamo action by differential rotation in a stably stratified stellar interior". In: *A&A* 381.3, pp. 923–932. DOI: 10.1051/0004-6361:20011465.

Sweet, P. A. (1950). “The Importance of Rotation in Stellar Evolution”. In: *Monthly Notices of the Royal Astronomical Society* 110.6, pp. 548–558. DOI: 10.1093/mnras/110.6.548.
Tassoul, J.-L. (1978). *Theory of rotating stars*.
Tassoul, M. (1980). “Asymptotic approximations for stellar nonradial pulsations.” In: *ApJS* 43, pp. 469–490. DOI: 10.1086/190678.
Tayler, R. J. (1973). “The adiabatic stability of stars containing magnetic fields-I.Toroidal fields”. In: 161, p. 365. DOI: 10.1093/mnras/161.4.365.
Townsend, R. H. D., Goldstein, J., and Zweibel, E. G. (2017). “Angular momentum transport by heat-driven g-modes in slowly pulsating B stars”. In: *Monthly Notices of the Royal Astronomical Society* 475.1, pp. 879–893. DOI: 10.1093/mnras/stx3142.
Townsend, R. H. D. and S. A. Teitler (2013). “gyre: an open-source stellar oscillation code based on a new Magnus Multiple Shooting scheme”. In: *Monthly Notices of the Royal Astronomical Society* 435.4, pp. 3406–3418. DOI: 10.1093/mnras/stt1533.
Turcotte, S., S. Keller, and R. Cavallo (2004). “Book Review: 3D stellar evolution / Astronomical Society of the Pacific, 2003”. In: *The Observatory* 124, p. 58.
Unno, W., Y. Osaki, H. Ando, H. Saio, and H. Shibahashi (1989). *Nonradial oscillations of stars*.
van Saders, J. L. and M. H. Pinsonneault (2013). “Fast Star, Slow Star; Old Star, Young Star: Subgiant Rotation as a Population and Stellar Physics Diagnostic”. In: 776.2, 67, p. 67. DOI: 10.1088/0004-637X/776/2/67.
von Zeipel, H. (1924). “The radiative equilibrium of a rotating system of gaseous masses”. In: 84, pp. 665–683. DOI: 10.1093/mnras/84.9.665.
Vrard, M., Mosser, B., and Samadi, R. (2016). “Period spacings in red giants - II. Automated measurement”. In: *A&A* 588, A87. DOI: 10.1051/0004-6361/201527259.
Walker, G. et al. (2003). “The MOST Asteroseismology Mission: Ultraprecise Photometry from Space”. In: *Publications of the Astronomical Society of the Pacific* 115.811, pp. 1023–1035.
Zahn, J. P. (1992). “Circulation and turbulence in rotating stars.” In: 265, pp. 115–132.
Zahn, J. P., Brun, A. S., and Mathis, S. (2007). “On magnetic instabilities and dynamo action in stellar radiation zones”. In: *A&A* 474.1, pp. 145–154. DOI: 10.1051/0004-6361:20077653.

Appendix A

Impact of rotation in the stellar structure

In this appendix we briefly touch on the impact of rotation in the stellar surface of KIC8579095 using the Fuller-formalism, for the prescription of angular momentum transport and without any rotation-induced chemical mixing (model details described in chapter 4).

The impact of rotation in the stellar structure, as discussed in chapter 2 and 3, is vastly studied in massive stars since rotation has a substantially stronger effect on their structure. Low and intermediate mass stars demonstrate weaker effects in fast rotation regimes. Sills et al. (2000) explain that this comes from the fact that the centrifugal acceleration balances the gravitational pull, consequently reducing the internal pressure of the star. Since in these stars there is a more a dominant degeneracy pressure in contrast to higher mass stars, the contribution of rotation to the total pressure in less massive stars will be a smaller fraction.However small this effects may be, the implementation of rotation on stellar models should not be neglected has it has secondary implications in other processes (e.g., the amount of lithium depletion).

The top panel of figure A.1 illustrates the HR diagram for a 1.4 $M_{\odot}$ model including the Fuller-formalism for different initial rotation velocities. The gravity darkening phenomena, as explained in chapter 3 becomes visible for higher rotations. The centrifugal acceleration lowers effective gravity, resulting in a reduction in the luminosity and in the effective temperature. Thus rapid rotators are cooler than slow rotators, despite the change in luminosity not being as significant as the change in temperature. The effect is dominant in the main-sequence, but suddenly disappears due to a steep decrease of the rotational velocity of the model as it evolves along the subgiant and red giant branch. In those stages, the H-burning shell promotes a rapid envelope expansion increasing the stellar radius hence decreasing the total rotation.In these stages the effects of high initial rotation rates are not relevant and the models evolve up the red giant branch into later stages almost independently of that parameter, as can be seen in the middle panel of figure A.1 that illustrates the evolution of the core rotation rate with the stellar radius.In models with initial rotation close to critical velocities in the main-sequence (e.g., 0.7 $\Omega_{\rm crit}$) the stellar envelope structure begins to be compromised as there is a drastic decrease in the effective temperature.

The bottom panel of figure A.1 shows the evolution of the equatorial/polar radius with the stellar radius. Rotation deforms the star from spherical symmetry, leading to an increase in the equatorial radius relative

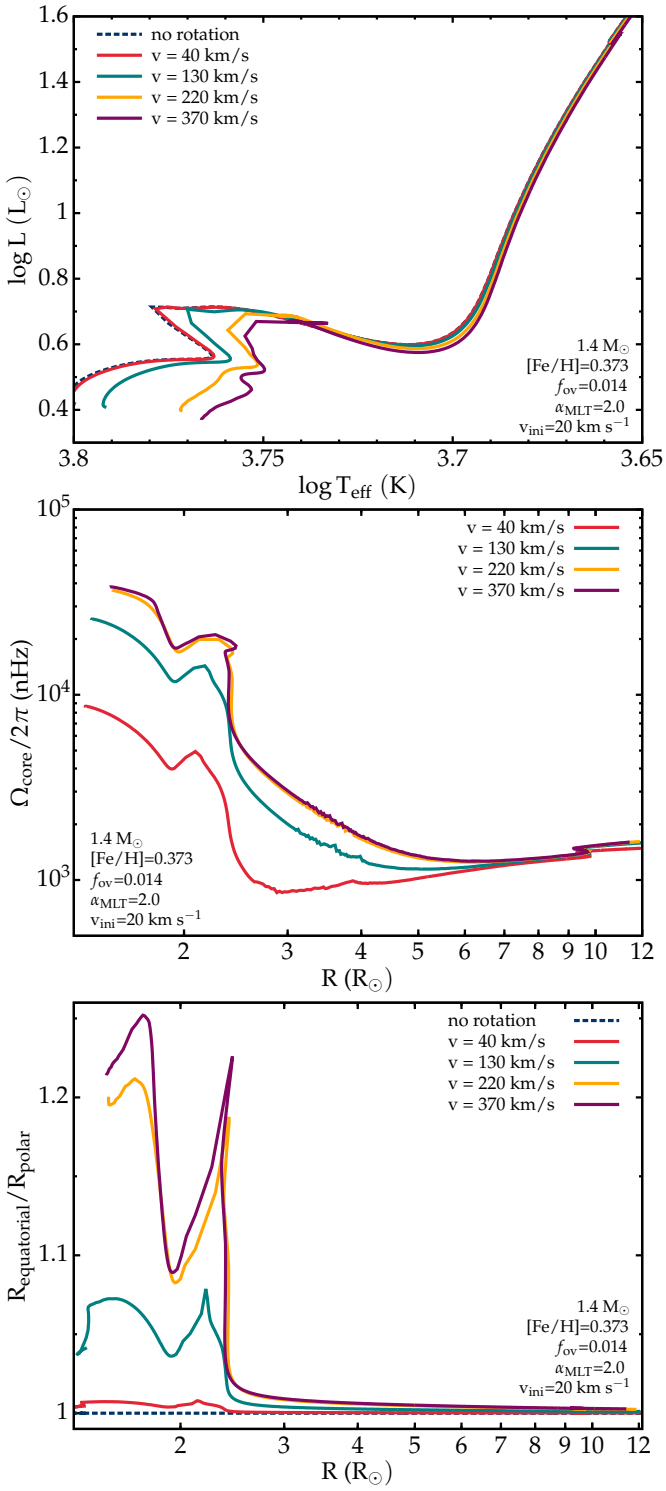

Figure A.1: HR diagram from ZAMS to the RGB of a 1.4 $M_{\odot}$ model using the Fuller-formalism described in detail in chapter 4 (top panel). Evolution of core rotation rate with the stellar radius (middle panel). Effect of increasing rotation rates in the equatorial versus polar radius ratio with the surface gravity (bottom panel). All panels include models with no rotation (dashed line), initial rotation velocity of 40 km/s (red), 130 km/s (green), 220 km/s (yellow) and 370 km/s (purple).

to the polar radius. Only very rapid rotators experience a strong effect – particularly important in the main-sequence, as older stars experience an increase in the stellar radius accompanied of a decrease in the rotation rate, rendering this effect fairly negligible.

Table A.1 shows how the age of the main-sequence models evolves with increasing initial rotation. Fast rotators have slightly longer lifetimes compared to slow ones, because they are fainter, and behave as slightly less massive non-rotating stars due to the decrease in total gravitational potential.

$\Omega_{\rm ini}$ (rad/s)	$v_{\rm ini}$ (km/s)	$\Omega/\Omega_{\rm crit}$	Age (Gyr)
3×10^{-5}	40	0.1	4.11
1×10^{-4}	130	0.3	4.18
2×10^{-4}	220	0.5	4.34
3×10^{-4}	370	0.7	4.48

Table A.1: Initial rotation velocities, ratio of current rotation versus the critical rotation and ages at the end of the main-sequence of the 1.4 $M_\odot$ model computed with Fuller-formalism and initialized with values in table 4.2.

Figure A.2 illustrates the variable f_P, defined in equation (2.11) (left), that modifies the equation of motion in the presence of rotation. The variable f_T (equation (2.11) (right)) is not represented here as its impact is negligible in our models $f_T \approx 1$ throughout all evolutionary stages. f_P only drops below 1 on very fast rotating models, assuring previous results. Since it enters directly in the structure equations implemented in MESA, the impact will be visible in the stellar structure. For slow rotators in the main-sequence and stars above the red giant bump (which is the case for the models of KIC8579095 in chapter 5) the impact of rotation in the stellar surface with the Fuller-formalism can be totally neglected.

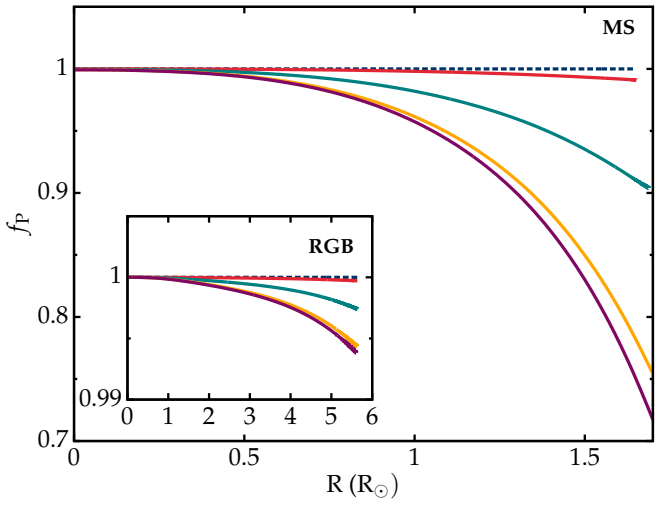

Figure A.2: Evolution of the quantity f_P with the radius with different initial velocities for a main-sequence model and for a red giant model (highlighted). $f_P = 1$ for the non rotating model. Model with no rotation (dashed line), initial rotation velocity of 40 km/s (red), 130 km/s (green), 220 km/s (yellow) and 370 km/s (purple).

Appendix B

Radial and horizontal eigenfunction displacements

In this appendix we show the full scaled radial and horizontal eigenfunction displacements for oscillation modes with local maximum and minimum in the dipole mode period spacing (see figure 5.5), an extension from section 5.3. The stellar oscillations were computed using GYRE and the equilibrium models were computed with MESA to model KIC8579095 (full description of the models in chapter 4). This appendix shows the comparison between eigenfunctions of oscillations modes of models with and without rotation-induced mixing.

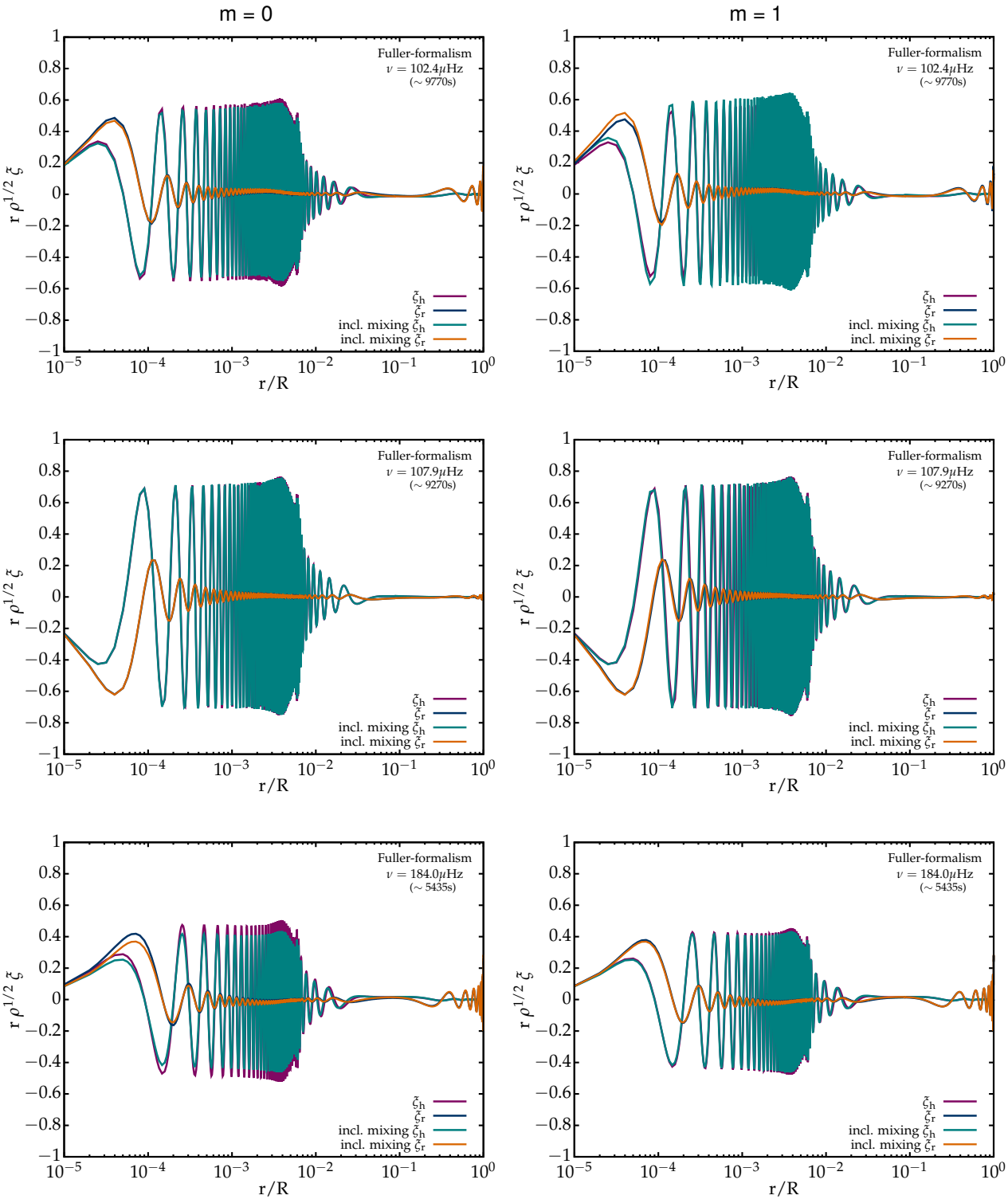

Figure B.1: Scaled radial and horizontal eigenfunction displacements (arbitrary scale) for modes with l=1, m=0 (left panels) and m=1 (right panels) for RGB models with the Fuller-formalism computed with and without rotation-induced mixing for comparison purposes. The modes in the first line correspond to the local minimum around 9770s (ν = 102.4 μHz) in figure 5.5. The second line corresponds to the local maximum around 9270s (ν = 107.9 μHz). The third line corresponds to the local minimum around 5435s (ν = 184.0 μHz).

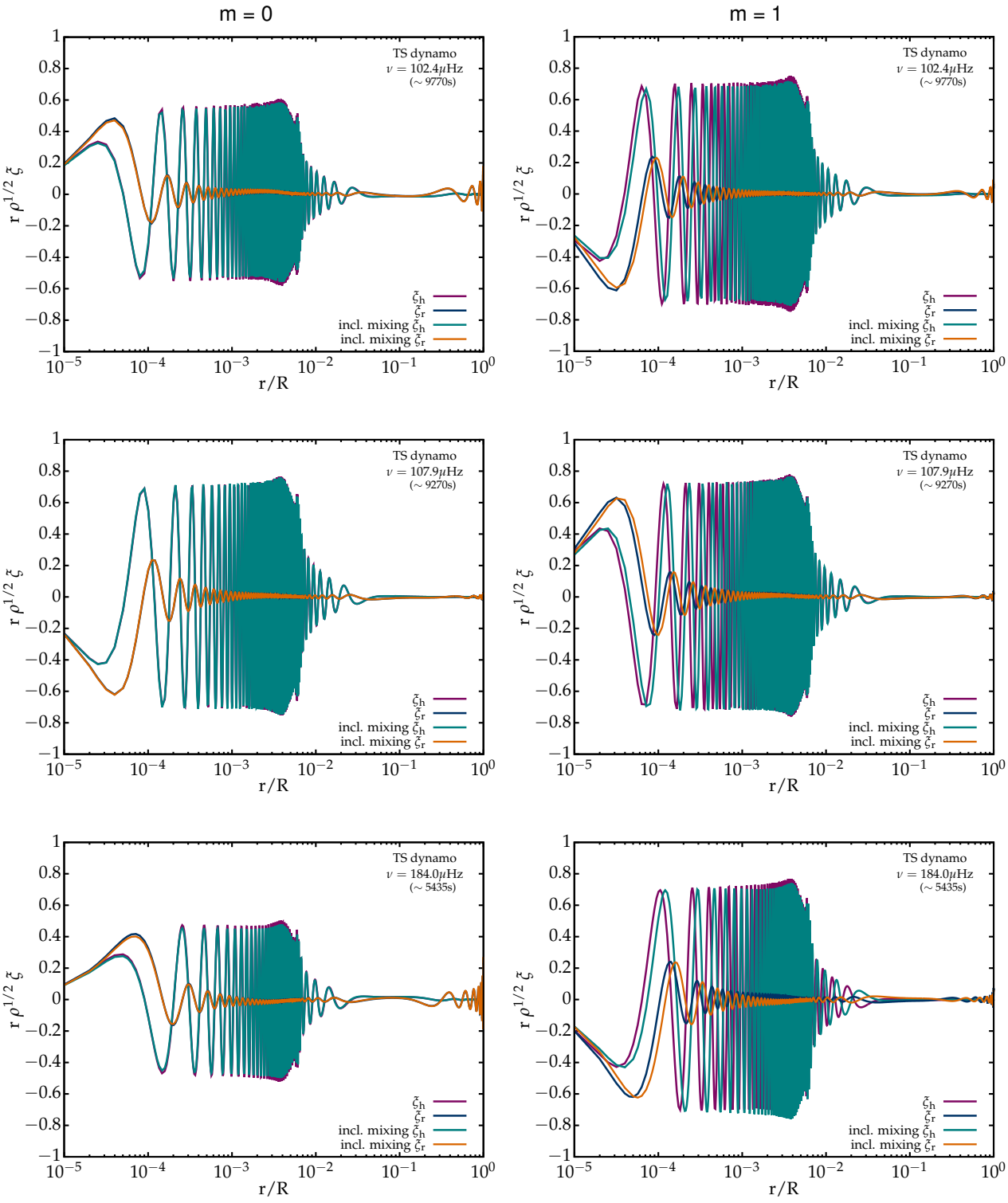

Figure B.2: Scaled radial and horizontal eigenfunction displacements (arbitrary scale) for modes with l=1, and m=0 (left panels) and m=1 (right panels) for RGB models with the Tayler-Spruit dynamo computed with and without rotation-induced mixing for comparison purposes. The modes in the first line correspond to the local minimum around 9770s (ν = 102.4 μHz) in figure 5.5. The second line corresponds to the local maximum around 9270s (ν = 107.9 μHz). The third line corresponds to the local minimum around 5435s (ν = 184.0 μHz).